Technische Universität München
Fakultät für Physik
Max-Planck-Institut für Astrophysik

Transfer of ionizing radiation in dusty, star-forming galaxies

Martin Glatzle

Vollständiger Abdruck der von der Fakultät für Physik der Technischen Universität München zur Erlangung des akademischen Grades eines

Doktors der Naturwissenschaften

genehmigten Dissertation.

Vorsitzende:	Prof. Dr. Elisa Resconi
Prüfende der Dissertation:	1. apl. Prof. Dr. Ewald Müller
	2. Prof. Dr. Sherry Suyu

Die Dissertation wurde am 22.06.2020 bei der Technischen Universität München eingereicht und durch die Fakultät für Physik am 19.10.2020 angenommen.

To my parents.

Contents

Abstract

Recent observations have found evidence of the presence of cosmic dust in and possibly surrounding star-forming galaxies even in the young Universe, suggesting early and efficient chemical enrichment. Dust strongly impacts the evolution and properties of galaxies, while itself constantly evolving, for example under the influence of the radiation emitted by stars or accreting black holes.

In this thesis, the interaction of cosmic dusty plasmas, as found in the interstellar and intergalactic media, with ionizing UV and X-ray radiation is studied. The required fundamentals from cosmology and structure formation, radiative transfer, and the science of cosmic dust are summarized. Furthermore, detailed descriptions of how the relevant properties of dust grains were obtained from a literature model are provided. Two consecutive extensions to a time dependent numerical scheme for the transport of ionizing radiation through primordial gas were implemented, the first being concerned with the absorption of radiation by dust and the second with the charging of dust grains under the associated irradiation. Both are applied to astrophysically motivated configurations and the results are discussed.

Additionally, contributions were made to related projects concerning the numerical transport of X-rays and the production and distribution of dust in the Milky Way and high redshift galaxies. Selected results are presented.

Finally, an outlook is provided on an ongoing project studying the escape of ionizing radiation from galaxies in the context of Cosmic Reionization.

Zusammenfassung

Jüngste Beobachtungen deuten auf eine frühe und effiziente chemische Anreicherung in sternbildenden Galaxien hin, so dass diese schon im jungen Universum kosmischen Staub enthielten. Staub hat großen Einfluss auf die Evolution und Eigenschaften von Galaxien, verändert dabei aber auch stets seine Beschaffenheit, z. B. auf Grund von Wechselwirkung mit von Sternen oder akkretierenden schwarzen Löchern emittierter elektromagnetischer Strahlung.

In dieser Arbeit wird die Wechselwirkung kosmischer, staubiger Plasmen, wie sie in interstellaren und intergalaktischen Medien zu finden sind, mit ionisierender UV- und Röntgenstrahlung untersucht. Die dafür erforderlichen Grundlagen aus Kosmologie, Strukturbildung, Strahlungstransport und der Forschung zu kosmischem Staub werden zusammengefasst. Des Weiteren wird die Bestimmung der zur Beschreibung dieser Wechselwirkung benötigten physikalischen Größen anhand eines Staubmodells aus der Literatur im Detail beschrieben. Im Kernteil der Arbeit wurden zwei aufeinander aufbauende Erweiterungen eines zeitabhängigen numerischen Modells für den Transport ionisierender Strahlung durch primordiales Gas implementiert. Die erste befasst sich mit der Absorption von Strahlung durch Staub und die zweite mit der daraus resultierenden elektrischen Aufladung der Staubkörner. Beide Erweiterungen werden auf astrophysikalisch motivierte Konfigurationen angewendet und die dabei erhaltenen Ergebnisse diskutiert.

Zusätzlich wurden wesentliche Beiträge zu mehreren themennahen Projekten geleistet, welche sich mit dem numerischen Transport von Röntgenstrahlung, bzw. mit der Entstehung und Verteilung von Staub in der Milchstraße sowie in stark rotverschobenen Galaxien auseinandersetzen. Ausgewählte Ergebnisse dieser Projekte werden präsentiert.

Abschließend wird ein laufendes Projekt zur Untersuchung der Emission ionisierender Strahlung aus gesamtheitlichen Galaxien im Kontext der kosmischen Reionisation vorgestellt.

Acknowledgements

To me personally, this monograph is more than my thesis; it is the conclusion of a journey that began nearly twelve years ago when I arrived in Germany with the intention of receiving a professional education. Although I would like to, I cannot here appropriately express my deep gratitude to everyone who, be it on the technical or on the personal side, made this journey possible, interesting, enjoyable and worthwhile. Thus, I will restrict myself in the following to thanking only those most directly involved in the creation of the present work.

I would like to thank Benedetta Ciardi for providing me a position in her research group and the freedom to work in my own way and explore different areas of interest to me.

Furthermore, I am very grateful to Ewald Müller for insightful discussions and for his support in the formal aspects of my thesis.

Last but certainly not least, a heartfelt thank-you to Luca Graziani for all the time, energy and effort spent on providing suggestions, guidance and support in many aspects of the doctoral student's life. Without you, this one would have ended differently. Grazie!

Chapter 1

Introduction

Cosmology is concerned with studying the origin, evolution and structure of the Universe. Numerical cosmology, one of its branches, has the ambitious goal of producing a "universe in a box", i.e. simulating (part of) a universe that statistically reproduces the properties of the observable Universe, while adopting numerical prescriptions based on first principles as closely as possible. Thus, it is a powerful tool in assessing the consistency of a cosmological theory with observations from the local and distant Universe. In the framework of the Standard Model of cosmology, which we assume in the present work, this goal is pursued by numerically evolving in time suitable initial conditions, which are derived from observations of, e. g., the cosmic microwave background (CMB), a relic of our Universe's early history (e.g. Mo et al., 2010). Indeed, one of the successes of standard cosmology is that it closely reproduces the observed large scale structure (LSS) of our Universe when adopted in cosmological simulations.

The evolution of the LSS is dominated by gravity, such that it can successfully be reproduced neglecting other physical interactions (e.g. Springel et al., 2005). On smaller scales, however, many physical phenomena apart from gravitational interaction are crucial in determining the properties of individual galaxies. This has been driving the inclusion of an increasing number of processes such as gas dynamics and star formation in numerical cosmological models (e.g. Katz et al., 1996; Springel & Hernquist, 2003), making them powerful tools also in understanding the origin of the diverse properties of observed galaxies. Unfortunately, the enormous disparity in the temporal and spatial scales on which these processes take place and those on which the Universe evolves, means that they cannot be resolved but have to be treated using effective models. This removes the simulations from first principles and complicates the interpretation of results and their comparison to observations. Nevertheless, this approach has met with success in many aspects (e.g. Nelson et al., 2018) and will undoubtedly be pursued further as even future computational facilities are unlikely to ever be capable of resolving all relevant scales in a fully self consistent manner.

As we will see in the course of this work, two important aspects of galaxy evolution, which before were neglected or could not be investigated with the computational

power available at the time, have in recent years received particular attention in numerical cosmology: ionizing radiation produced by stars and other sources and cosmic dust.

The main goal of the work presented here has been to study the interaction of ionizing radiation with gas and dust in galaxies and to investigate some of the consequences of this interaction with the help of newly developed numerical methods. Related aspects have, however, also been examined. In the remainder of this chapter, we will revisit some fundamental concepts from standard cosmology (§ 1.1) and structure formation (§ 1.2) required for the subsequent text. Our discussions will be necessarily concise and incomplete and we refer the reader to the cited literature for more details. Finally, we will discuss the work performed within the scope of this thesis, state which parts have been previously published and where, and provide an outline of the remaining text (§ 1.3).

1.1 Standard cosmology

Current standard cosmology, also known as ΛCDM model, assumes the theory of general relativity (GR) to be the correct generalization of the classical gravitational force and therefore to provide the framework in which to describe our Universe at large scales (e. g. Dodelson, 2003). GR establishes a relation between the geometry of a space-time (i. e. its metric) and its energy/matter and momentum content via the Einstein Field Equations (EFE). In addition to baryonic matter[1] and electromagnetic radiation, the energy/matter content of the Universe is assumed to consist of dark energy and dark matter (DM). Dark energy is modelled as non-interacting vacuum energy with a constant density (a cosmological constant Λ). Dark matter is assumed to consist of massive particles with low thermal speeds ("cold" dark matter, CDM), which interact almost exclusively gravitationally.

ΛCDM cosmology furthermore relies on the "cosmological principle", the hypothesis that our Universe is spatially homogeneous and isotropic on large scales. It can be shown (e. g. Carroll, 2014) that the cosmological principle alone implies a space-time geometry given by the Friedmann-Lemaître-Robertson-Walker (FLRW) metric, which is completely determined by the curvature k and the scale factor, $a(t)$, describing the change of length scale with time. For later use, note that a freely streaming photon in FLRW geometry undergoes a change in frequency ν described by

$$\frac{\nu_\mathrm{e}}{\nu_\mathrm{o}} = \frac{a(t_\mathrm{o})}{a(t_\mathrm{e})}\,, \tag{1.1}$$

where the subscript "e" refers to the photon's emission and the subscript "o" to its observation.

[1] This includes all ordinary matter, also leptons such as electrons, which, however, contribute only little energy.

Together, the EFE and the FLRW metric result in the Friedmann equation, an ordinary differential equation describing the temporal evolution of a in terms of k and the energy/matter content of the Universe. In combination with thermodynamic considerations and an equation of state, a closed system can be derived (e.g Mo et al., 2010, Ch. 3), which, given values of k and the energy/matter content at a certain time, allows to describe the evolution of a and the Universe's thermal state.

In this framework, our Universe is best described as flat ($k = 0$) and dominated by dark energy ($\sim 70\,\%$ of the energy content) at the present time (t_0), with CDM ($\sim 25\,\%$), baryonic matter ($\sim 5\,\%$) and radiation (negligible) being subdominant. This implies that it is expanding (a grows in time) and was denser and hotter in the past, leading to the hypothesis of its origin in a "Hot Big Bang". The expansion results in a photon from a distant source reaching Earth being redshifted (cf. Eq. (1.1)) with the cosmological redshift z defined by

$$1 + z \equiv \frac{\nu_\mathrm{e}}{\nu_\mathrm{o}} = \frac{a(t_0)}{a(t_\mathrm{e})}\,. \tag{1.2}$$

z is a monotonic function of t_e (and also the distance of the emitting object), such that it is often used to designate a point in the Universe's history. Determining the cosmological redshift of emission/absorption lines from an observed object thus allows to determine its distance and the epoch of the Universe's history in which it is observed.

Since ΛCDM cosmology provides a description of the Universe's thermal history, by applying knowledge from particle, nuclear and atomic physics, one can in principle predict the Universe's matter content. For example, Big Bang Nucleosynthesis[2] describes the formation of atomic nuclei from free protons and neutrons formed earlier as the Universe cooled by expansion to temperatures below nuclear binding energies. It successfully explains the so called primordial composition, in which, by mass, 75 % of baryons reside in ^{1}H nuclei, 25 % reside in ^{4}He nuclei, and traces reside in other light nuclei. As the Universe expanded and cooled further, free electrons could eventually recombine[3] with the primordial nuclei to form atoms. At $z \sim 1100$, this resulted in a dramatic increase of the mean free path, or the "decoupling", of primordial photons, which before scattered frequently, mostly off free electrons, and could afterwards stream virtually freely, forming the cosmic photon background. Today, we observe these photons, redshifted to the microwave band, as the CMB, one of the most important observational constraints for any cosmological model (e.g. Planck Collaboration et al., 2018). After photon decoupling, the Universe entered the so called Dark Ages, a period elusive to observation, and the formation of structure set in.

[2] For reasons of brevity, we will not discuss earlier processes, please consult, e.g., Dodelson (2003) or Carroll (2014) and references therein for further information.

[3] This historical term is slightly inaccurate, since electrons and nuclei combined for the first time.

Before we move on to a brief discussion of structure formation in § 1.2, note that the comparatively simple ΛCDM model is by no means complete in the sense of providing a full description of the Universe and its evolution. While it is remarkably powerful and accurately predicts many observed properties of the Universe given only few observational constraints, several open questions remain, some of which we will briefly mention here. The perhaps most prominent issue is that the nature of dark energy and dark matter remain unknown. No explanation of dark energy in terms of a quantum field theoretical vacuum energy has been found and, despite significant effort, no dark matter particle has been identified. Furthermore, the very early history of the Universe is poorly understood. At the earliest times a general relativistic treatment is expected to break down, with no clearly established generalization available to replace it, resulting in several issues. For example, if the cosmological principle held perfectly on all scales, structure formation would not have been possible and the Universe would remain smooth. Small density perturbations on small scales are presumed to be the seeds of structure formation. However, ΛCDM provides no explanation for the origin of these perturbations, which presumably formed at the earliest times. Therefore, no prediction from first principles for the initial conditions of structure formation is currently possible and they have to be derived, instead, from the imprint of the primordial perturbations observed in the CMB (e.g. Mo et al., 2010).

1.2 Galaxy formation and reionization

In this section we briefly describe hierarchical structure formation from photon decoupling to the present day as it is understood in ΛCDM cosmology, which will provide important context for the central subjects of this thesis. For a more complete discussion, we refer to Mo et al. (2010).

Perturbations in the initially smooth matter distribution are gravitationally unstable in ΛCDM: over-dense regions attracted matter from their surroundings, becoming even denser, with under-dense regions consequently becoming more tenuous. This process was slowed down by the expansion of the Universe, but eventually over-densities collapsed, becoming gravitationally bound. The collision-less CDM, the dominant matter component, relaxed, ultimately reaching quasi-equilibrium and forming so called dark matter halos connected by cosmic sheets and filaments separated by vast cosmic voids, with the ensemble of these structures being referred to as “cosmic web”. Neighbouring halos can undergo mergers, resulting in a picture of hierarchical structure formation, with the most massive halos typically forming where filaments of the cosmic web intersect. This qualitative picture is supported by N-body simulations (e.g. Springel et al., 2005), which discretise the CDM content

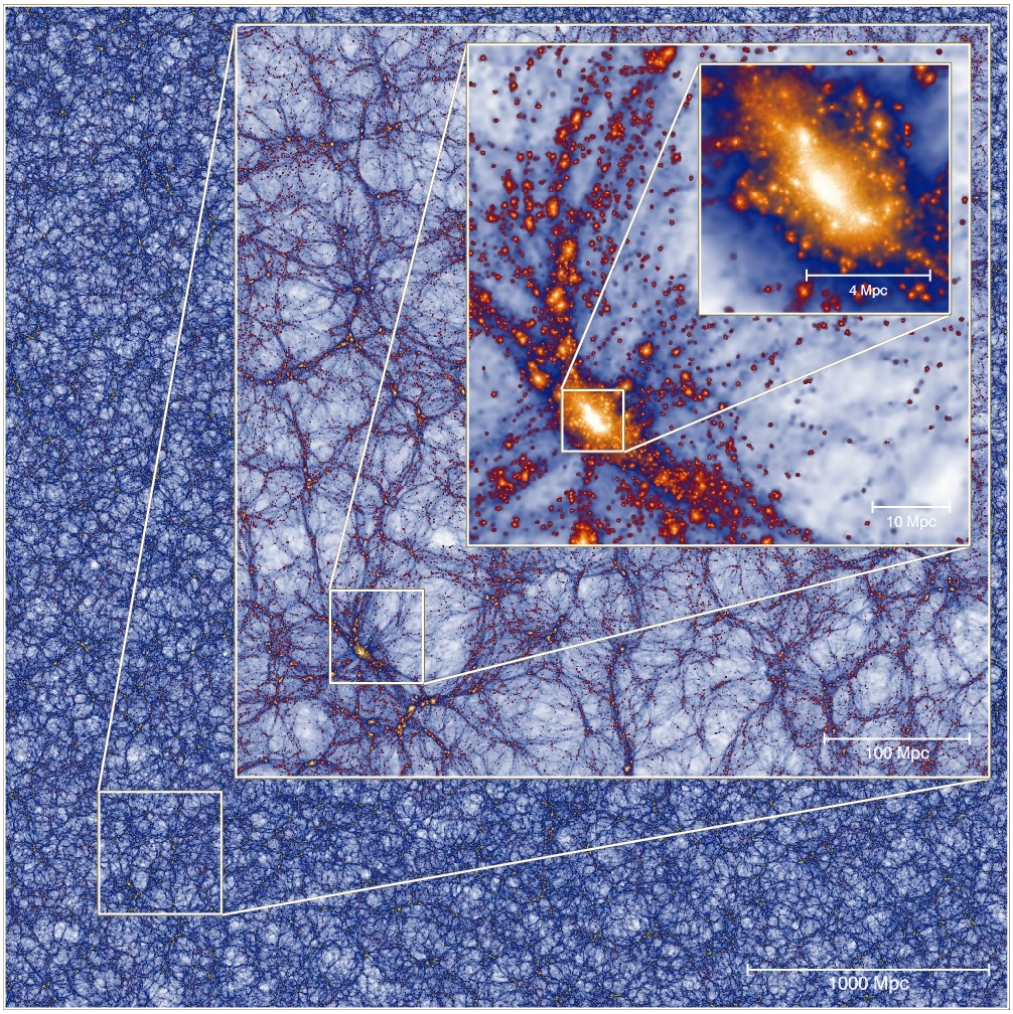

Figure 1.1: The present day ($z = 0$) projected DM mass density of a slice of 8 Mpc thickness and 4.1 Gpc side length from the Millenium-XXL simulation, with insets progressively zooming in on the most massive halo. ©: R. Angulo & S. White, MPA Garching.

of a part of the Universe into billions of massive, collision-less particles[4] and follow their evolution under the influence of gravity from the Dark Ages to the present day, successfully reproducing the observed LSS of the Universe. In Fig. 1.1 we show an example DM distribution at $z = 0$ from the Millenium-XXL simulation (Angulo et al., 2012). Note that the cosmic web is homogeneous on scales of $\sim 10^8$ pc, while in the insets more and more structure in the form of filaments, nodes, and even individual DM halos can be distinguished as one zooms in. In the smallest inset, finally, a massive halo and its substructure can be seen.

The primordial density perturbations are assumed to have contained baryonic and dark matter in proportion to their overall abundances ($\sim 1 : 5$). However, while the collision-less CDM component formed halos in quasi-equilibrium, the baryonic component got shock heated in the gravity-driven collapse. This created thermal pressure gradients counteracting gravity. Radiative cooling processes then allowed some of the baryonic gas to shed energy and to form cool, dense proto-galaxies at the centres of the gravitational potential wells of DM halos. In a yet poorly understood process, pockets of the cooling primordial gas are presumed to have started collapsing under self-gravity and to eventually form the first stars (Pop III stars), marking the end of the Dark Ages and the beginning of the complex evolution of the interstellar medium (ISM) through physical processes involving radiation, chemistry and hydrodynamics, often referred to as "feedback processes" (e.g Barkana & Loeb, 2001; Ciardi & Ferrara, 2005; Bromm & Yoshida, 2011).

Stellar feedback is one the central drivers of ISM evolution. Stars emit large amounts of energy in the form of electromagnetic radiation (radiative feedback), which profoundly impacts the ISM, for example by ionizing atoms. Particularly towards the end of their life, stars will furthermore inject momentum into their surroundings (mechanical feedback), for example in the form of stellar winds or supernova (SN) explosions. Mechanical feedback is associated with the ejection of material by stars and thus also results in the enrichment of the ISM with metals[5] formed by stellar nuclear fusion (chemical feedback). One of the numerous effects of chemical feedback is that it enables the formation of cosmic dust. Stars of later generations (Pop II/I stars), were then born from chemically enriched media and, naturally, themselves fed back into these media, subject to new physical processes. Stellar radiation, for example, will now additionally interact with cosmic dust.

As ISM evolution and structure formation take place, a galaxy might accrete additional primordial baryonic matter from the intergalactic medium (IGM, e.g.

[4] These dark matter particles are not to be confused with dark matter particles in the sense of particle physics. They represent, rather, a discretisation of the dark matter mass distribution and are many times more massive than any candidate CDM particle.

[5] Elements heavier than helium are called metals in astrophysics.

Meiksin 2009)[6]. At the same time, the IGM evolves under the influence of galactic feedback. Powerful galactic winds, for example, could chemically enrich it, at least in the vicinity of galaxies. Moreover, while the IGM was left neutral by recombination, it is observed to be highly ionized in the present Universe (e.g. Fan et al., 2006). The corresponding transition is referred to as Cosmic Reionization and, while it is not yet understood in many details, in the standard paradigm it is assumed to be mainly driven by stellar ionizing radiation escaping galaxies (e.g. Meiksin, 2009). This radiation is assumed to have formed growing ionized and hot bubbles around individual galaxies, which eventually started overlapping and finally pervaded the IGM in its entirety, with the reionization of hydrogen being completed around $z \sim 6$.

While baryonic physics has little influence on the LSS, it is essential in determining the observational properties of the IGM and of individual galaxies. In order to produce realistic galaxy populations, it thus has to be accounted for in cosmological simulations. Since baryonic matter is not collision-less, the inclusion of gas dynamics is a crucial step. The computational method of smoothed-particle-hydrodynamics (SPH), which discretises the baryonic matter into particles, in analogy to the treatment of CDM, is a popular choice to solve the corresponding hydrodynamical equations (e.g. Springel, 2005), with alternative methods being based on volume discretisation (i.e. meshes) (e.g. Teyssier, 2002). Recently, so called hybrid or moving-mesh schemes, which improve on some shortcomings of SPH (e.g. Heß & Springel, 2010), have been frequently adopted (e.g. Weinberger et al., 2019). Many more baryonic processes, chiefly of course star formation (e.g. Springel & Hernquist, 2003), are important and numerical models are being constantly improved to feature more detailed physics. Most of these processes, however, can not be fully resolved due to the large dynamical range involved and are therefore treated in effective or "sub-grid" models. These are informed by specialized theoretical, numerical and observational studies on smaller scales, such that numerical cosmology heavily relies on other branches of astrophysics.

In this thesis, as we will discuss in more detail in § 1.3, specific aspects of the interplay between radiative and chemical feedback are investigated using the theory of radiative transfer and models of dust formation and evolution.

1.3 Project description, previous publications and thesis outline

The main subject of this thesis has been to investigate the transfer of radiation through cosmic gas and dust, the corresponding physical consequences, and possible implications for galaxy formation, feedback and reionization. To accomplish this, extensions to a numerical scheme for the transport of ionizing radiation through

[6]There are no universally accepted definitions of ISM and IGM and, especially in young, poorly developed galaxies, it might be difficult to clearly distinguish between them.

primordial gas have been developed to enable it to additionally account for the interaction of this radiation with cosmic dust. A first extension, concerned with the absorption of radiation by dust, has been completed and results have been published (Glatzle et al. 2019, hereafter GCG19) and presented to the scientific community (contributed talk at *Dusting the Universe*; 2019; Tucson, Arizona). A second extension, concerned with the charging of dust grains, has been implemented and tested, with a publication being in preparation (Glatzle et al., 2020). Finally, a cosmological application studying the escape of radiation from galaxies including the first extension is being worked on, with first preliminary results being available.

To embed the central subject into a broader context, contributions have been made to related projects. Graziani et al. (2018) study the transfer of X-rays and their implementation forms the basis of the extensions developed here. Graziani et al. (2020) study the production and distribution of dust in the early Universe, a crucial ingredient for realistic radiative transfer models. Similarly, Leike et al. (2020a) study the distribution of dust in the solar neighbourhood, where it can be resolved in detail. Further work (Leike et al., 2020b) making use of the code[7] developed here for Leike et al. (2020a) will not be discussed as it is not pertinent to the central subject.

Several auxiliary software packages have been developed and released under open source licenses, the most important being:

- `cosmic_dustbox`[8]: a Python package including various tools to compute properties of cosmic dust grains as predicted by models from the literature.
- `pyBPASS`[9]: a Python package for the efficient computation and binning of spectra as predicted by BPASS (Stanway & Eldridge, 2018) for stellar populations formed in cosmological simulations.

In Table 1.1 a summary of the author's contributions to the different previous publications is provided, including an overview of the parts of the present work where the corresponding results are discussed.

The remainder of the thesis is organised as follows: in Ch. 2 we introduce the theory of radiative transfer, describe how it is used in the context of astrophysics/cosmology and present the numerical implementation CRASH, on which our work is based. Ch. 3 gives on overview of what is known about cosmic dust, discusses how it is produced and distributed, and introduces models which provide the dust properties required for radiative transfer studies. Our implementation and results regarding absorption by dust are presented in Ch. 4, while the corresponding discussion of dust charging can be found in Ch. 5. Finally, we give an outlook on the aforementioned cosmological application in Ch 6 and provide our conclusions in Ch. 7.

[7] `https://gitlab.mpcdf.mpg.de/mglatzle/gda_futils`
[8] `https://gitlab.mpcdf.mpg.de/mglatzle/cosmic_dustbox`
[9] `https://gitlab.mpcdf.mpg.de/mglatzle/pybpass`

Publication	Discussed in	Contributions
X-ray ionization of the intergalactic medium by quasars Graziani L., Ciardi B., Glatzle M.		
Graziani et al. (2018)	§ 2.5	scientific discussion software testing contr. to manuscript
Radiative transfer of ionizing radiation through gas and dust: the stellar source case Glatzle M., Ciardi B., Graziani L.		
GCG19	§ 3.5, Ch. 4, Apps. A, B	numerical modelling software engineering software development software testing execution of simulations simulation analysis principal author of manuscript
The assembly of dusty galaxies at $z \geq 4$: statistical properties Graziani L., Schneider R., Ginolfi M., Hunt L. K., Maio U., Glatzle M., Ciardi B.		
Graziani et al. (2020)	§ 3.6	scientific discussion contr. to result analysis minor contr. to manuscript
Resolving nearby dust clouds Leike R. H., Glatzle M., Enßlin T. A.		
Leike et al. (2020a)	§ 3.2	scientific discussion software development software deployment contr. to manuscript

Table 1.1: Previuos publications, results of which are discussed in the present work in the indicated locations. The author's contributions to each publication are also listed.

Chapter 2

Radiative transfer through ISM/IGM

Radiative transfer (RT), in its full generality, is the physical phenomenon of the propagation of electromagnetic radiation and the associated interactions it takes part in.

Electromagnetic radiation comprises a significant part of the energy content of many astrophysical environments, such as the ISM and IGM (Draine, 2011a), and is often a major source of the "new energy" being injected into an environment, for example in the form of starlight in the case of the ISM. Thus, it frequently contributes importantly to the evolution of such environments (e. g. by ionizing gas). Moreover, despite the recent rise of multi-messenger astronomy (e. g. Abbott et al., 2016a,b; Adrián-Martínez et al., 2016; IceCube Collaboration et al., 2018; IceCube Collaboration, 2018), electromagnetic radiation is still the most important carrier of information that astronomers have access to for objects beyond the reach of in-situ experiments. For the above reasons, RT plays a central role in our understanding of many of the physical processes that govern the evolution of the Universe and in the interpretation of astrophysical observations.

In this chapter, we will first briefly discuss the theory of RT (§ 2.1) and connect it to the physics of ISM/IGM (§ 2.2) before giving an overview of numerical methods applied to RT problems in astrophysics (§ 2.3). We will then describe the numerical method used as a basis for much of the work presented here (§ 2.4) and discuss a recent extension to it as well as some applications (§ 2.5, Graziani et al. 2018). Finally, we will briefly consider the role of RT in the dynamics of ISM/IGM (§ 2.6).

2.1 Radiative transfer equations

Mathematically, an electromagnetic field can be described by the four-component Stokes vector (e. g. Pomraning, 1973, Ch. IV). The problem of radiative transfer can then be modelled by a set of coupled equations for the temporal and spatial evolution of these components, referred to as radiative transfer equations (RTEs).

If radiation polarization can be neglected, as in the cases studied in this work, only one component of the Stokes vector, namely the specific intensity I, is required to describe the radiation field. To develop an intuitive understanding of I, it is useful

to adopt a probabilistic approach in which radiation is modelled as a collection of a large number of photons with phase space density $f(\mathbf{r}, \nu, \mathbf{\Omega}, t)$, where $\mathbf{r}$ is a point in space, ν is a photon frequency, $\mathbf{\Omega}$ is a direction on the unit sphere and t is a point in time. Then:

$$I(\mathbf{r}, \nu, \mathbf{\Omega}, t) = ch\nu f(\mathbf{r}, \nu, \mathbf{\Omega}, t) \tag{2.1}$$

with the speed of light c and Planck's constant h.

Deriving the RTE now amounts to equating changes in I due to photon movement and interactions with matter to its temporal derivative. We refer the reader to Pomraning (1973) for details on this and restrict ourselves to stating the result for matter with a refractive index of unity moving at non-relativistic speeds:

$$\frac{1}{c}\frac{\partial I}{\partial t} + \mathbf{\Omega} \cdot \nabla I = S - \alpha_\mathrm{e} I + \int_0^\infty \mathrm{d}\nu' \int_{4\pi} \mathrm{d}\mathbf{\Omega}' \frac{\nu}{\nu'} \alpha_\mathrm{ds} \left(\nu' \to \nu, \mathbf{\Omega}' \to \mathbf{\Omega}\right) I \,. \tag{2.2}$$

The terms on the left hand side are the temporal derivative of I and the so called photon streaming term, describing the change in I due to movement of photons. On the right hand side, $S(\mathbf{r}, \nu, \mathbf{\Omega}, t)$ is the source term which describes the emission of photons from matter, $\alpha_\mathrm{e}(\mathbf{r}, \nu, \mathbf{\Omega}, t)$ is the extinction coefficient describing absorption of photons by matter and scattering out of direction $\mathbf{\Omega}$, and the last term describes scattering of photons into direction $\mathbf{\Omega}$ and frequency ν from all other directions and frequencies with the differential scattering coefficient $\alpha_\mathrm{ds}(\mathbf{r}, \nu' \to \nu, \mathbf{\Omega}' \to \mathbf{\Omega}, t)$.

It is immediately evident that this seven-dimensional integro-differential equation is exceedingly hard to solve in general and it will, with the exception of highly symmetric or strongly simplified cases, not have an analytic solution. This fact has driven the development of powerful numerical schemes to provide approximate solutions for general configurations, which we will discuss in more detail in § 2.3.

In the present work, we will exclusively be concerned with applications in which scattering of radiation can be neglected (see also § 3.5.2). In such cases, Eq. (2.2) can be greatly simplified:

$$\frac{1}{c}\frac{\partial I}{\partial t} + \mathbf{\Omega} \cdot \nabla I = S - \alpha_\mathrm{a} I \,, \tag{2.3}$$

where α_a is the absorption coefficient. It describes the probability of absorption for a photon travelling a distance $\mathrm{d}s$ in direction $\mathbf{\Omega}$:

$$\mathrm{d}P_\mathrm{a} = \alpha_\mathrm{a}(\mathbf{r}, \nu, t)\, \mathrm{d}s \,. \tag{2.4}$$

In the most general of cases, α_a — as does α_e above — will carry a dependence on $\mathbf{\Omega}$, since the propagation medium may be anisotropic. In the ISM, for example, non-spherical dust grains with a preferential orientation on large scales can cause

such anisotropy (e. g. Draine, 2011a, Ch. 21.3). A detailed discussion of this is beyond the scope of the present work, but see § 3.1 .

Note that generally α_a indirectly depends on I, since the radiation field can change the abundances of species (e. g. by ionization). The source term S generally carries a similar dependence. Radiative heating, for example, can change the temperature of dust grains and consequently their re-emission properties and the ionization state of a medium will determine its recombination emission. Thus, the RTE is non-linear in I and the physical status of a system and the radiation field pervading it need to be solved for simultaneously.

For the sake of completeness, we remark that to study RT on intergalactic scales in the framework of ΛCDM cosmology, an RTE in a comoving frame on a flat, uniformly expanding space-time is required. It can be shown (e. g. Gnedin & Ostriker, 1997, App. A) that this RTE, again under the assumption of a refractive index of unity, non-relativistic matter flows and no scattering, takes the following form:

$$\frac{1}{c}\frac{\partial I}{\partial t} + \boldsymbol{\Omega}\cdot\nabla I + \frac{1}{c}\frac{\dot{a}}{a}\left(3I - \nu\frac{\partial I}{\partial \nu}\right) = S - \alpha_\mathrm{a} I\,, \tag{2.5}$$

where $a(t)$ is the space-time scale factor.

Before moving on to a short discussion of the physics which determine α_a and S and their connection with I, we introduce for later use the optical depth

$$\tau_\nu = \int\limits_{\mathcal{C}} \mathrm{d}s\, \alpha_\mathrm{a} \tag{2.6}$$

along a path $\mathcal{C}$ and observe that the probability that a photon following this path undergoes absorption is given by:

$$P = 1 - \mathrm{e}^{-\tau_\nu}\,. \tag{2.7}$$

2.2 Astrophysical plasmas

In this section we will connect the rather abstract discussion presented above to the physics of the ISM and IGM as it is understood today. For exhaustive discussions of what can only be mentioned briefly here, see Ferland (2003), Dopita & Sutherland (2003), Osterbrock & Ferland (2006) and Draine (2011a), but also Ferland et al. (2017).

Most of the baryonic matter in the ISM/IGM from which stars and galaxies form is in the gaseous state. Hydrogen and helium are by far the most abundant atoms in this gas ($\sim 92\,\%$ and $\sim 8\,\%$ by number respectively), but metals (e. g. C, O, Fe) and molecules (e. g. H_2, CO) are also present, particularly in the ISM, which is generally chemically more enriched. A fraction of the matter, finally, is observed to reside in

the solid state in the form of dust grains (see Ch. 3). As we will see below and in Ch. 5, these particles absorb radiation and collide with each other, which frequently leaves them ionized so that ISM/IGM are what is referred to as dusty plasmas[1].

The electromagnetic radiation that pervades both ISM and IGM covers an enormous range of frequencies from the radio to the gamma-ray regime. The sources of this radiation are diverse, including, for example, stars and quasars but also emission from hot interstellar dust or ionized gas (see § 2.2.1).

Consequently, ISM/IGM astrophysics offers a vast number of applications for radiative transfer, including, for example, spectral synthesis (e. g. Ferland et al., 2017), the transfer of emission line radiation (e. g. Eide et al., 2018b; Behrens et al., 2019) and dust continuum radiative transfer (e. g. Stalevski et al., 2012). For the purposes of this work, however, we focus on hydrogen ionizing radiation, specifically in the photon energy range 13.6 eV to 10 keV. The energy range 13.6 eV to 200 eV is customarily referred to as ionizing UV (ultra-violet) band and the range 200 eV to 3 keV as soft X-ray band, with the hard X-ray band beginning at 3 keV[2]. Young, massive stars are responsible for most emission in the UV, whereas more extreme sources such as X-ray binaries and quasars are accountable for the emission of X-rays.

In the remainder of this section, we will briefly describe the physics of the interaction of hydrogen ionizing radiation with a plasma, establishing the connection between the transport of this radiation and the status of the plasma and its evolution in time. We will restrict ourselves to a plasma composed of hydrogen and helium, keeping track of the five ions[3] (H I, H II, He I, He II, He III) and free electrons. We will not explicitly consider excited states of any of the ions, since they have a short expected lifetime against radiative de-excitation and are typically not significantly populated in the diffuse plasmas of ISM/IGM (e. g. Gould & Thakur, 1970; Black, 1981; Ferland & Williams, 2016). In Ch. 4 and 5 we will extend our discussion to include dust. We will not, however, discuss the physics of atomic metals (for more details see Graziani et al., 2013) or molecules.

2.2.1 Microphysical processes

Microphysical processes govern the transitions between different ionic species and the creation and destruction of photons and thus form the basis of our discussion.

[1] Sometimes a distinction is made between "dust-in-plasma" and "dusty plasma" (Mendis & Rosenberg, 1994), with the former referring to cases where dust grains can be considered to be isolated from each other. We will not make this distinction here.

[2] These designations are not exact and conventions differ from community to community.

[3] Throughout this work we will use Roman numerals to refer to ions in the ground state, e. g. H I refers to the ground state of neutral hydrogen and He II refers to the ground state of singly ionized helium. This notation is ambiguous, since it is generally used to refer to the spectra of ions (e. g., H II is the spectrum produced by singly ionized hydrogen, see `http://www.ferland.org/cloudy/cii_vs_cp.htm`), but it is customary in the reionization community.

We have to consider the following transition processes between the species we track (e. g. Black, 1981), which we discuss individually below:

photoionization:

$$\begin{aligned} \mathrm{H\,I} + \gamma &\rightarrow \mathrm{H\,II} + \mathrm{e}^- \\ \mathrm{He\,I} + \gamma &\rightarrow \mathrm{He\,II} + \mathrm{e}^- \\ \mathrm{He\,II} + \gamma &\rightarrow \mathrm{He\,III} + \mathrm{e}^- \end{aligned}$$

collisional ionization:

$$\begin{aligned} \mathrm{H\,I} + \mathrm{e}^- &\rightarrow \mathrm{H\,II} + 2\mathrm{e}^- \\ \mathrm{He\,I} + \mathrm{e}^- &\rightarrow \mathrm{He\,II} + 2\mathrm{e}^- \\ \mathrm{He\,II} + \mathrm{e}^- &\rightarrow \mathrm{He\,III} + 2\mathrm{e}^- \end{aligned}$$

radiative recombination:

$$\begin{aligned} \mathrm{H\,II} + \mathrm{e}^- &\rightarrow \mathrm{H\,I}^{**} + \gamma \rightarrow \mathrm{H\,I} + \gamma \\ \mathrm{He\,II} + \mathrm{e}^- &\rightarrow \mathrm{He\,I}^{**} + \gamma \rightarrow \mathrm{He\,I} + \gamma \\ \mathrm{He\,III} + \mathrm{e}^- &\rightarrow \mathrm{He\,II}^{**} + \gamma \rightarrow \mathrm{He\,II} + \gamma \end{aligned}$$

dielectronic recombination:

$$\mathrm{He\,II} + \mathrm{e}^- \rightarrow \mathrm{He\,I}^{**} \rightarrow \mathrm{He\,I} + \gamma\,,$$

where γ represents one or more photons and e^- a free electron, while the double asterisk indicates an excited state.

Photoionization is the process of ejection of a bound electron from an atom or ion upon the absorption of a photon. It is a threshold-process since it requires the photon's energy to be higher than the electron's binding energy. Three of the species we track, namely H I, He I and He II, have bound electrons. Their threshold energies for photoionization are 13.6 eV, 24.6 eV and 54.4 eV respectively[4]. In the left panel of Fig. 2.1 we show the three corresponding cross sections as functions of photon energy. The cross sections peak sharply at the ionization thresholds and then fall off approximately linearly in log-log towards higher energies. They reach comparable peak magnitudes, but keep in mind that hydrogen is much more abundant than helium.

Ionization in a plasma can also happen when a free electron collides with a bound electron and ejects the latter in a process referred to as collisional ionization. For this to happen, the incoming free electron, naturally, must carry sufficient kinetic

[4] He I has two electrons but they can be assumed to occupy the same energy level for our purposes.

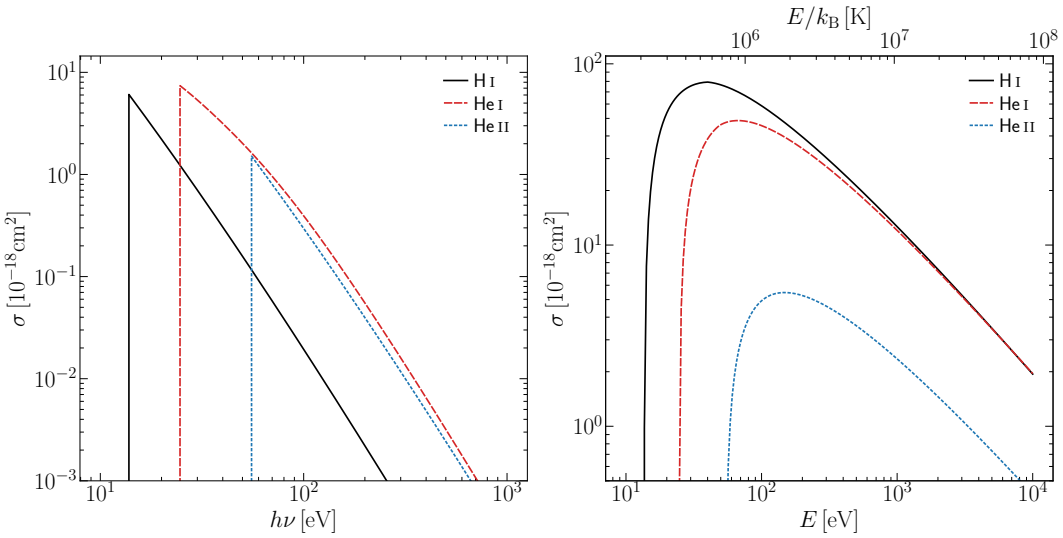

Figure 2.1: **Left:** Photoionization cross sections for H I, He I and He II as functions of photon energy (Verner et al., 1996). **Right:** Collisional ionization cross sections for H I, He I and He II as functions of energy of the incoming free electron (Lotz, 1967). Also shown is energy divided by the Boltzmann constant k_B to indicate at what temperatures (see § 2.2.2 for more details) electrons can be expected to have the corresponding energy.

energy to overcome the binding potential. We show the corresponding cross sections in the right panel of Fig. 2.1. The peaks are shifted towards higher energies from the ionization potentials and smoother compared to those for photoionization, indicating that collisional ionization is more likely to happen if excess kinetic energy is available for both ejecting and ejected electron. A thermal plasma is characterised by the fact that the kinetic energies its electrons carry can be described by a temperature, i. e. a macroscopic parameter. We will go into more detail on this in § 2.2.2, but on the secondary x-axis we show the typical temperatures corresponding to the electron energies on the primary x-axis.

Radiative recombination is the process of free electrons being captured into bound states by ions under emission of a photon. Since we do not explicitly track excited states, we assume that capture to an excited state will result in its decay to the ground state under emission of a cascade of secondary photons. That is to say, we neglect excitations/ionizations from excited states as well as their collisional de-excitation, which is unlikely in a tenuous plasma. In this approximation, the effective cross section for recombination to the ground state corresponds to the sum over the recombination cross sections to all states. For a given state, the cross section

for recombination can be computed from its photoionization cross section via the Milne relation (e. g. Draine, 2011a, § 3.31).

If an ion is not fully stripped of electrons, recombination may be assisted by a collision of the incoming free electron with a bound electron, putting both in excited states. This is referred to as dielectronic recombination, since two electrons are involved. The resulting excited ion is susceptible to auto-ionization but may stabilize under the emission of a photon, completing the recombination. The process thus depends on the cross section for the initial capture into a doubly excited state as well as on the probability for auto-ionization (e. g. Gould & Thakur, 1970). Of the species considered here, only He II can recombine via the dielectronic channel. Note, however, that the required free electron energies are quite high (several ten eV), since He II needs to be excited for this process to happen. As for radiative recombination, we will assume excited states to quickly decay to the ground state under emission of secondary photons.

In addition to recombination, several other processes in a plasma give rise to the emission of photons. Collisions can excite atoms/ions leading to the emission of radiation when the excited states decay[5]. Finally, the acceleration of charged plasma particles results in the emission of Bremsstrahlung. Since all these processes can happen at every point in the plasma, the resulting emission is referred to as diffuse emission.

2.2.2 Plasma temperature

The cross sections for collisional processes discussed in § 2.2.1 depend on the kinetic energy of the participating electron. The frequency with which they happen will therefore depend on the speed distribution of the free electrons. In astrophysical plasmas, an often well justified assumption is that these have a thermal, i. e. Maxwellian, speed distribution characterised by a kinetic temperature[6] T (e. g. Bohm & Aller 1947; Gould & Thakur 1971; see also Mo & Raizen 2019). Recently, it has been suggested that this assumption may not hold for certain photo-ionized nebulae (e. g. Zhang et al., 2016), but this claim has been strongly contested (Ferland et al., 2016; Draine & Kreisch, 2018).

With one exception discussed in the next paragraph, throughout this work, we will assume the electrons to have a thermal speed distribution. We will also assume all other plasma particles to have the same temperature (see Spitzer, 1978, Ch. 2)[7].

[5] If the atom/ion is excited by a photon instead of an electron, often a photon of almost identical energy will be re-emitted, which can be modelled as scattering, e. g. Eide et al. (2018b) and Behrens et al. (2019).

[6] Unless otherwise stated, the word temperature will refer to the kinetic temperature throughout this work.

[7] In shocks (e. g. Raymond et al., 2008) and for extreme temperatures (e. g. Shapiro et al., 1976) this assumption can break down.

There are situations in astrophysical plasmas where thermal speed distributions do not apply (e. g. Raymond et al., 2008; Ferland et al., 2016). The case relevant for this work is that of high energy photoelectrons. A photoelectron is typically thermalized quickly via collisions with other electrons before it collides with atoms/ions, such that it may be assumed to be thermal to begin with. Fast photoelectrons released in a neutral or partially neutral region, however, may cause collisional ionizations[8] before being thermalized. This process is referred to as secondary ionization. Naturally, it becomes more important the higher the energy of the ejecting photon. Instead of modelling it using a high energy tail of the electron speed distribution, we treat it as an additional source of ionizations (cf. Ferland et al., 2016). More detail is given in § 2.5 with regards to Graziani et al. (2018) (but see also Shull & van Steenberg 1985; Dalgarno et al. 1999; Valdes & Ferrara 2008; Furlanetto & Johnson Stoever 2010).

2.2.3 Transition, heating and cooling rates

Suppose we know the radiation field I and the status of a plasma at a certain point and time. In the case discussed here, the status of the plasma is encoded in its temperature T, the number densities n_i of the plasma constituents (n_H and n_He in our case) and the ionization fractions x_i (e. g. $x_{\mathrm{He\,II}} = n_{\mathrm{He\,II}}/n_\mathrm{He}$). We can then compute the transition rates between the different states, as well as the rate of energy transfer between the radiation field and the plasma. In § 2.2.4 we will use these quantities to express the combined time evolution of the plasma status and the radiation field.

The photoionization rate for an ion in a radiation field with spectral energy density u_ν can be computed as follows:

$$\zeta = \int_{\nu_0}^{\infty} \sigma(\nu) c \frac{u_\nu \,\mathrm{d}\nu}{h\nu} \,, \tag{2.8}$$

where ν_0 is the ionization threshold frequency. u_ν, in turn, can be computed from the specific intensity I:

$$u_\nu(\mathbf{r}, t) = \frac{1}{c} \int I(\mathbf{r}, \nu, \mathbf{\Omega}, t) \,\mathrm{d}\mathbf{\Omega} \,. \tag{2.9}$$

Rates for collisional processes can be computed similarly using rate coefficients (e. g. Draine, 2011a, § 2.1). For a reaction between species A and B with cross section σ_{AB}, for instance, the rate coefficient is given by

$$\langle \sigma_{AB} v \rangle = \int_0^{\infty} f_v \sigma_{AB}(v) v \,\mathrm{d}v \,, \tag{2.10}$$

[8] And take part in other interactions; see § 2.5.

where f_v is the relative speed distribution. The rate per unit volume for this reaction is then $n_A n_B \langle \sigma_{AB} v \rangle$. f_v is a function of T and the reduced mass $\mu = m_\mathrm{A} m_\mathrm{B}/(m_\mathrm{A}+m_\mathrm{B})$ of the collisional partners (Draine, 2011a, § 2.1). In all processes we consider here, one of the collision partners is much lighter (i. e. an electron) and thus usually faster than the other (i. e. an atom or ion), such that the motion of the heavy partner can be neglected ($\mu \approx m_\mathrm{e}$).

In Fig. 2.2, we show the corresponding rate coefficients for recombination[9] including dielectronic recombination (left panel) and collisional ionization (right panel) for all ionic species we track as functions of T. The strong increase in $\alpha_{\mathrm{He\,II}}$ setting in at around $4 \times 10^5\,\mathrm{K}$ is caused by dielectronic recombination becoming effective, since at these temperatures free electrons have enough kinetic energy to excite the remaining bound electron of He II. At temperatures of $10^4\,\mathrm{K}$ and below, the collisional ionization rate coefficients are much smaller than the recombination rate coefficients. The converse is true at temperatures higher than $10^6\,\mathrm{K}$ with the transition taking place at roughly $10^5\,\mathrm{K}$. This indicates that, for a plasma at high temperatures, collisional ionization can not be balanced by recombination, leading to high ionization fractions. Under such conditions, typical for example of astrophysical shocks, photoionization will usually be subdominant, with bound electrons being ejected collisionally before they can absorb a photon. At $10^4\,\mathrm{K}$ and below, on the other hand, photoionization will be the dominant source of ionization, if a strong enough radiation field is present.

The processes we have discussed here, transfer kinetic energy to or remove kinetic energy from plasma particles. Specifically, energy being transferred to the plasma from the radiation field is referred to as radiative heating and the converse process is referred to as radiative cooling. Photoionization radiatively heats the plasma, converting photon energy into electron kinetic energy. Collisional ionization, on the other hand, non-radiatively cools the plasma, since the ejecting electron's energy is used to overcome the binding energy of the ejected electron. The diffuse emission processes we have discussed, remove kinetic energy from electrons and transfer it to photons, thus radiatively cooling the plasma[10].

From the rates of all involved processes one can compute the rates of kinetic energy transfer from/to the plasma per unit volume as functions of the radi-

[9] We repeat that these are effective recombination rate coefficients, assuming excited states to decay radiatively after recombination; cf. § 2.2.1.

[10] Note that ionization/recombination processes increase/decrease the number of free particles, such that the relation between heating and cooling and the plasma temperature, which is a measure for the energy *per particle*, is not as simple as one might naively expect (cf. Eq. (2.16)). Photoionization, e. g., can *lower* a plasma's temperature if ejected electrons carry near-zero kinetic energy.

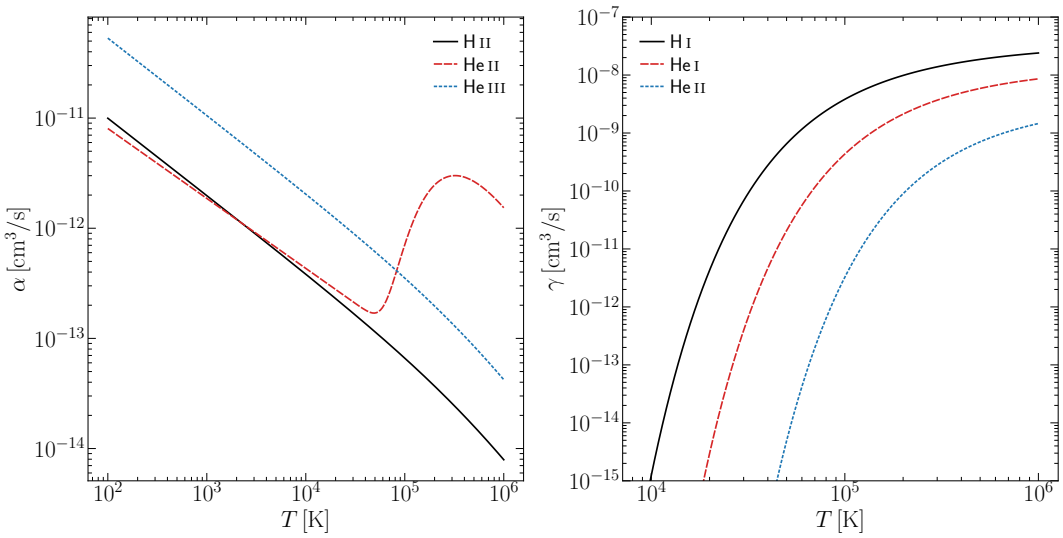

Figure 2.2: **Left:** Full recombination rate coefficients, α, for H II, He II and He III as functions of electron temperature (Cen, 1992). At around 5×10^4 K, dielectronic recombination of He II becomes efficient, resulting in a strong increase of the recombination rate. **Right:** Rate coefficients for collisional ionization by electrons, γ, for H I, He I and He II as functions of electron temperature (Cen, 1992).

ation field and plasma status, which are known as cooling/heating functions $\Lambda(T, n_i, x_i)/\mathcal{H}(I, T, n_i, x_i)$ (e. g. Cen, 1992)[11].

2.2.4 Time evolution of the plasma state and radiation field

We can now connect the RTE (2.3) with the physics discussed above.

For a plasma, it is convenient to express the absorption coefficient for each species i in terms of its number density $n_i(\mathbf{r}, t)$ and photon absorption cross section $\sigma_i(\nu)$:

$$\alpha_{\mathrm{a},i} = n_i(\mathbf{r}, t)\sigma_i(\nu)\,. \tag{2.11}$$

The total absorption coefficient is then given by the sum of the individual absorption coefficients. Note that, at any given redshift, number densities vary significantly from environment to environment going from dense clouds in the ISM ($n \approx 10^6\,/\mathrm{cm}^3$) to voids in the IGM ($n \lesssim 10^{-4}\,/\mathrm{cm}^3$).

To encode emission in the source term S on the right hand side of the RTE, typically, one of two approximations is used: either radiation is assumed to originate in a single point or the emission is modelled as a field, assigning an emissivity to every point in

[11] See Wang et al. (2014) for an example involving a more complicated plasma composition.

space. The spatial scale of the problem being investigated determines which approach is more appropriate for a certain source type. Naturally, different approaches may be used for different source types in the same problem, for example, by modelling a star as a point source and the diffuse emission from the gas surrounding it as an extended source. When considering only ionizing radiation, diffuse emission is often subdominant compared to the primary emission from compact sources.

Naturally, α_a and S depend on the status of the plasma, the time evolution of which we will investigate now. For the ionization state, we find the following equations:

$$\begin{aligned} n_\mathrm{H}\frac{\mathrm{d}x_{\mathrm{H\,II}}}{\mathrm{d}t} &= \gamma_{\mathrm{H\,I}} n_{\mathrm{H\,I}} n_\mathrm{e} - \alpha_{\mathrm{H\,II}} n_{\mathrm{H\,II}} n_\mathrm{e} + \zeta_{\mathrm{H\,I}} n_{\mathrm{H\,I}} \\ n_\mathrm{He}\frac{\mathrm{d}x_{\mathrm{He\,II}}}{\mathrm{d}t} &= \gamma_{\mathrm{He\,I}} n_{\mathrm{He\,I}} n_\mathrm{e} - \alpha_{\mathrm{He\,II}} n_{\mathrm{He\,II}} n_\mathrm{e} + \zeta_{\mathrm{He\,I}} n_{\mathrm{He\,I}} \\ n_\mathrm{He}\frac{\mathrm{d}x_{\mathrm{He\,III}}}{\mathrm{d}t} &= \gamma_{\mathrm{He\,II}} n_{\mathrm{He\,II}} n_\mathrm{e} - \alpha_{\mathrm{He\,III}} n_{\mathrm{He\,III}} n_\mathrm{e} + \zeta_{\mathrm{He\,II}} n_{\mathrm{He\,II}} \end{aligned} \tag{2.12}$$

with the closure relations

$$\begin{aligned} 1 &= x_{\mathrm{H\,I}} + x_{\mathrm{H\,II}} \\ 1 &= x_{\mathrm{He\,I}} + x_{\mathrm{He\,II}} + x_{\mathrm{He\,II}} \\ n_\mathrm{e} &= x_{\mathrm{H\,II}} n_\mathrm{H} + (x_{\mathrm{He\,II}} + 2x_{\mathrm{He\,III}}) n_\mathrm{He}\,. \end{aligned} \tag{2.13}$$

The equation governing the temperature evolution can be derived from energy conservation:

$$\frac{\mathrm{d}u}{\mathrm{d}t} = \mathcal{H} - \Lambda\,, \tag{2.14}$$

with the specific internal energy

$$u = \frac{3}{2} p k_\mathrm{B} T \tag{2.15}$$

and $p = n_\mathrm{H} + n_\mathrm{He} + n_\mathrm{e}$ the number density of free particles. Combining this, one finds

$$\frac{\mathrm{d}T}{\mathrm{d}t} = \frac{2}{3k_\mathrm{B}p}\left[-\frac{3}{2}k_\mathrm{B}\frac{\mathrm{d}p}{\mathrm{d}t}T + \mathcal{H} - \Lambda\right]\,. \tag{2.16}$$

The above emphasizes again the complexity of general RT applications, which can not take advantage of symmetries or assume solutions to be time steady and instead have to evolve the physical status of the propagation medium and the radiation field simultaneously. In § 2.3 we will discuss how such complexity can be tackled with the help of numerical schemes.

2.3 Numerical methods

The numerical techniques used to solve 3D RTEs in astrophysics can roughly be grouped into three categories. The first category is comprised of so called moment methods. These rely on a series expansion of the RTE in question in terms of the (usually first and second) solid angle moments of the specific intensity. This reduces the problem to be solved to a set of coupled partial differential equations and a so called closure relation derived from assumptions. We refrain from discussing this in more detail and refer the interested reader to Gnedin & Abel (2001) for a detailed discussion of one such method.

Ray tracing schemes, which solve a 1D-RTE along many rays cast through a 3D computational domain to obtain the 3D solution form the second category. As for moment methods, we will not go into more detail here and refer the reader to Rijkhorst et al. (2006) and Mellema et al. (2006) for further information.

The third category, finally, is comprised of so called Monte Carlo (MC) methods, which take a stochastic approach to RT. Since this technique underlies the present work, we will discuss it in some detail in § 2.3.1.

2.3.1 Monte Carlo Radiative Transfer

Monte Carlo Radiative Transfer (MCRT) takes a different approach to studying RT problems than the two other methods mentioned above. It does not try to solve RTEs either directly or in a simplified form but rather aims at simulating the underlying RT process itself. To this end, radiation is represented using discrete sampling units or quanta. These quanta are interpreted either as units of radiant energy (energy packets, e. g. Lucy 1999) or as collections of a large number of photons (photon packets, e. g. Maselli et al. 2009). Packets are injected into the simulation where radiant energy is created (e. g. by stars) and then propagated through the computational domain undergoing physical interactions with the matter present (e. g. absorption). Some of the initial properties of a packet (e. g. propagation direction) and certain aspects of its fate (e. g. interaction locations) are determined randomly by sampling appropriate probability density functions, although different schemes vary as to where randomized choices are taken. Even though the propagation of every single packet is essentially random, the entire ensemble of packets, provided it is chosen to be large enough, thus gives an accurate representation of the transport process and allows to determine physical quantities of interest.

Unlike the more rigorous mathematical strategies adopted by other methods, the intuitive approach of the MC method to RT allows for comparatively straightforward implementations that require moderate modelling and coding efforts and tend to lend themselves relatively easily to extensions and generalizations, such as the inclusion of additional physical processes. Moreover, intrinsically, i. e. without requiring

modifications of the implementation, MCRT methods offer principally arbitrary precision in exchange for an increased sampling rate. On the other hand, any physical quantity extracted from an MCRT simulation will have an unknown stochastic uncertainty, which can often only be quantified by comparing to a simulation run with a higher sampling rate. This, naturally, comes at an increased computational cost. Reaching an acceptable or required level of precision in MCRT can thus be challenging and computationally very expensive. Particularly in applications to media with high optical depths, the computational cost can become prohibitive (e. g. Camps & Baes, 2018; Krieger & Wolf, 2020).

For reasons of brevity, we will now go over to a discussion of the MCRT code used in this work, CRASH, and refrain for the most part from providing a more general context. However, we encourage the interested reader to become acquainted with the excellent reviews of the MCRT method as used for a variety of applications in astrophysics by Whitney (2011), Steinacker et al. (2013) and Noebauer & Sim (2019). Descriptions of specific implementations apart from CRASH can, for example, be found in Jonsson (2006), Bisbas et al. (2015b), Verstocken et al. (2017) and Vandenbroucke & Wood (2018).

2.4 The cosmological radiative transfer code CRASH

CRASH (Cosmological RAdiative transfer Scheme for Hydrodynamics) is a 3D MCRT code that was developed specifically to study time dependent RT problems in the context of reionization and cosmology (Ciardi et al. 2001; Maselli et al. 2003, 2009; Pierleoni et al. 2009; Graziani et al. 2013; Hariharan et al. 2017; Graziani et al. 2018 and GCG19). A CRASH simulation predicts the temporal evolution of the ionization status and temperature of astrophysical gas as a function of space in a volume of interest under the influence of radiation in the ionizing band (13.6 eV to 10 keV) emitted by the sources (e. g. stars, quasars) in this volume and/or impinging on the volume from outside. It does this by simulating the transfer of the radiation through the volume and its interaction with the absorbers present. The absorbers considered are hydrogen and helium and, as one of the results of the work presented here, cosmic dust. The first version of CRASH was developed almost two decades ago (Ciardi et al., 2001), followed by various updates (Maselli et al., 2003, 2009) and a complete rewrite (Graziani, 2012; Graziani et al., 2013). The latest updates were published in Graziani et al. (2018) (X-ray physics) and GCG19 (dust absorption). Here we will now outline the basic CRASH algorithm, referring the reader to the literature cited above for details. As they will be discussed separately in § 2.5 and Ch. 4, respectively, the updates from Graziani et al. (2018) and GCG19 are not included in this description.

The initial conditions required for a CRASH simulation encompass a gas density

distribution, a field describing the temperature and ionization status and the positions and spectral energy distributions of all point sources in the simulation volume. The gas distribution and status are mapped onto a three-dimensional Cartesian grid and assumed to be constant within single cells. The gas density distribution, moreover, is assumed to be constant during the simulation, i. e. gas dynamics are not followed (cf. § 2.6). The evolution of the gas density due to cosmological expansion can, however, be taken into account. This is also true of the cosmological redshift of the propagated photons, i. e. CRASH can simulate transport according to both Eq. (2.3) and Eq. (2.5). Time dependent RT simulations that span long timescales during which gas and source configurations can not be assumed to be constant (e. g. simulations of reionization), can be performed by running CRASH on a time sequence of configurations and combining the outputs appropriately (e. g. Ciardi et al. 2003, 2012; Eide et al. 2018a).

During the simulation, CRASH will loop over all point sources in arbitrary but fixed order, emitting and propagating a photon packet from each. This process is repeated until each source has emitted the user-specified maximum number of packets N_p. The simulation time is advanced by a constant time step Δt after each loop over the sources, which is given by N_p and the simulation duration.

A packet emitted by a source j contains

$$N = Q_{0,j}\Delta t \tag{2.17}$$

photons, where $Q_{0,j}$ is the source's emissivity in the ionizing band. These photons are distributed over a number of frequency bins specified by the user, i.e. CRASH propagates what is referred to as coloured or polychromatic photon packets (Jonsson, 2006; Maselli et al., 2009). The direction of the packet is determined by randomly sampling the source's angular probability distribution function. After emission, it will be moved along the ray defined by this direction and the source's position. For each cell it crosses in this process, the number of photons N_ν in each frequency bin is reduced by

$$\Delta N_\nu = N_\nu(1 - \mathrm{e}^{-\tau_\nu}), \tag{2.18}$$

with the optical depth $\tau_\nu = l\sum_i n_i\sigma_i(\nu)$, $i \in \{\mathrm{H\,I}, \mathrm{He\,I}, \mathrm{He\,II}\}$ and the path cast through the cell l. The total number of absorbed photons is limited by the number of available absorbers and any photons to-be-absorbed in excess of the available absorbers will be kept in the packet to ensure energy conservation. Each packet is propagated until this process results in its depletion or it escapes the simulation volume, i.e. CRASH uses the infinite speed of light approximation. A discussion of the implications of this can be found in Graziani et al. (2018, App. D).

Each time a cell is crossed by a packet, its ionization state and temperature are updated by evolving the coupled system of Eqs. (2.12) and (2.16) in time using a first order explicit Euler scheme. The rate coefficient for collisional ionization and

the recombination rate coefficient, as well as the cooling function are computed using literature prescriptions; see Maselli et al. (2003) for more details. The photoionization rate ζ_i and the heating function $\mathcal{H}$, on the other hand, are computed using the number of photons absorbed from the packet:

$$\zeta_i = \frac{\sum_\nu \Delta N_{i,\nu}}{\delta t} \tag{2.19}$$

and

$$\mathcal{H} = \frac{\sum_i \sum_\nu \Delta N_{i,\nu}(h\nu - h\nu_{0,i})}{\delta t \Delta V}\,, \tag{2.20}$$

where

$$\Delta N_{i,\nu} = \frac{\tau_{i,\nu}}{\tau_\nu} \Delta N_\nu \tag{2.21}$$

is the number of photons of each frequency ν absorbed by species i (Friedrich et al., 2012, App. D), δt is the time that has passed since the last packet crossing and ΔV is the cell volume.

Diffuse, ionizing emission (cf. § 2.2.1) can, in principle, be accounted for (Maselli et al., 2003), however, this feature will not be used for the present work.

2.5 The transfer of X-rays

X-rays have a long mean free path due to the low cross sections hydrogen and helium (as well as other absorbers) offer at high energies (cf. Fig. 2.1), allowing them to drive photochemistry and deposit energy in regions well shielded from UV radiation. Thus, they could be important agents in regulating the chemistry in many, often dusty galactic environments, such as for example protoplanetary disks (e. g. Rab et al., 2018) or molecular clouds (e. g. Mackey et al., 2019).

Dust grains can acquire high charges when exposed to X-rays (e. g. Weingartner et al. 2006 and Ch. 5). The charge values could become high enough for Coulomb repulsion to exceed the tensile strength of grains, resulting in what is referred to as Coulomb explosions. This mechanism has been suggested as a possible explanation for the dearth of small grains in the neighbourhoods of quasars (Tazaki et al., 2020). X-rays have further been shown to be able to efficiently destroy polycyclic aromatic hydrocarbons (PAHs, large organic molecules assumed to be abundant in the ISM; e. g. Li 2020 and Ch. 3) by dissociating molecular bonds (Monfredini et al., 2019).

As discussed in § 2.2.1, high energy photoelectrons ejected into a plasma may take part in collisional processes with plasma constituents other than free electrons before being thermalized by these. Typical single-star spectra, even of massive stars that have a high UV output, provide very few of the hard photons required for the production of these energetic electrons (e. g. Draine & Kreisch, 2018). When considering radiation sources such as quasars or X-ray binaries that emit considerable

power in the X-ray regime (e. g. Richards et al., 2006), however, the fate of hot photoelectrons has to be carefully investigated to understand their impact. It is hypothesized, for example, that the X-ray emission from sources formed early in the history of the Universe could have left a peculiar imprint, distinct from that of UV radiation, on the ionization and temperature state of the IGM before reionization was complete (e. g. Fialkov et al., 2014; Eide et al., 2018a). This has implications for the detectability of the 21 cm signal emitted by neutral intergalactic hydrogen at these early times (e. g. Semelin et al., 2017), which is expected to be detectable by current (e. g. LOFAR[12], MWA[13]) or future (e. g. SKA[14]) radio telescopes.

Interpreting observations of these phenomena and understanding their importance and effects in different environments requires precise theoretical modelling of the interaction of X-rays with astrophysical plasmas. A first step towards this goal has been taken in Graziani et al. (2018) by implementing a module for the treatment of X-rays being absorbed by a hydrogen and helium plasma and thus producing high energy photoelectrons in CRASH. This section is based on Graziani et al. (2018) and we will now discuss the underlying physical models and the implementation itself, show an illustrative, idealised example application and study a more realistic scenario based on the emission of a powerful quasar impinging on the IGM at high redshift. For details omitted here see Graziani et al. (2018) and for further applications of this module, see Kakiichi et al. (2017), Eide et al. (2018a) and Eide et al. (2020, in prep.).

2.5.1 Modelling secondary ionization

The initial kinetic energy $E_\mathrm{k} = h\nu - h\nu_0$ of an electron with initial binding energy $h\nu_0$ released in an ionization event induced by a photon $h\nu$, will be distributed in the plasma across different processes (collisional ionization/excitation, heating, etc.). Of course, the distribution depends on the individual electron's history as well as on the composition and status of the plasma at the injection point. In a weakly ionized plasma, generally, a larger fraction of the energy will be deposited in collisional ionizations than in a strongly ionized plasma. Computing the fate of individual electrons self consistently, however, is intractable in simulations of astrophysical plasmas, requiring the use of what can be referred to as "effective models". These models provide average photoelectron histories as functions of the initial kinetic energy and the plasma status, usually obtained by averaging the results of large numbers of detailed Monte Carlo simulations. Each simulation run follows a single photoelectron injected at a fixed kinetic energy into a plasma with a fixed status and the secondaries it produces. Such computations have, for example, been performed

[12] `http://www.lofar.org`
[13] `http://www.mwatelescope.org`
[14] `http://www.skatelescope.org`

by Shull & van Steenberg (1985); Dalgarno et al. (1999) and Valdes & Ferrara (2008), who provide prescriptions for the number of secondary ionizations of species i, $N_{\mathrm{s},i}$, induced by a photoelectron and the fraction of its kinetic energy, f_Q, that contributes to heating the plasma. Here, $N_{\mathrm{s},i}$ and f_Q are assumed to be functions of E_k and the ionization state as described in more detail below[15].

Shull & van Steenberg (1985) compute $N_{\mathrm{s},i}$ and f_Q for a plasma composed of hydrogen and helium at cosmological abundances. They consider $10^{-4} \leq x_{\mathrm{H\,II}} \leq 0.95$ and kinetic energies from 0 eV to 3 keV. However, they only provide analytic fits valid for $100\,\mathrm{eV} \leq E_\mathrm{k} \leq 3\,\mathrm{keV}$. $x_{\mathrm{He\,II}} = x_{\mathrm{H\,II}}$ and $x_{\mathrm{He\,III}} = 0$ is assumed and collisional ionization/excitation of H I and He I as well as Coulomb collisions with electrons are considered. Interactions with He II turned out to be unimportant in their model.

Dalgarno et al. (1999) extend previous work by including a wealth of microphysical processes: collisional ionization/excitation of and momentum transfer to H I and He I, ionization/excitation of He II, ionization/excitation/dissociation of and momentum transfer to molecular hydrogen (H_2) and finally Coulomb collisions with other electrons. They study different plasma compositions, including a hydrogen/helium mixture at cosmological abundances which we will use here. Fits are provided for $N_{\mathrm{s},i}$ and f_Q where $30\,\mathrm{eV} \leq E_\mathrm{k} \leq 1\,\mathrm{keV}$ and $10^{-6} \leq x_\mathrm{e} \leq 0.1$, with $x_\mathrm{e} = n_\mathrm{e}/(n_\mathrm{H} + n_\mathrm{He})$[16].

Valdes & Ferrara (2008) take an approach similar to that of Shull & van Steenberg (1985), in that they consider a cosmological H/He mixture and assume $x_{\mathrm{He\,II}} = x_{\mathrm{H\,II}}$ and $x_{\mathrm{He\,III}} = 0$. However, they make use of newer atomic data and consider collisional ionization of H I, He I and He II, collisional excitation of H I and He I, Coulomb collisions with electrons and protons and, finally, hydrogen recombination when following the fate of an electron. They provide results for $E_\mathrm{k} = 3\,\mathrm{keV}$ and $E_\mathrm{k} = 10\,\mathrm{keV}$ and $10^{-4} \leq x_{\mathrm{H\,II}} \leq 0.99$.

The models described in this section allow the extension of ionization schemes used in RT codes, enabling their use to study the transfer of X-rays. The corresponding implementation in CRASH will be discussed in the next section.

2.5.2 Numerical implementation

A pre-requisite for the extension of an RT code for the ionizing UV band to the X-ray band is the use of photoionization cross sections that remain accurate at the correspondingly higher photon energies. CRASH uses the cross sections provided by Verner et al. (1996) (cf. Fig. 2.1). These are analytic fits to experimental data, which

[15] Note that in each study specific assumptions are made on the plasma composition and the relations between the ionization states of different species. Furthermore, any temperature dependence, e. g. in the modelling of Coulomb collisions with free electrons, is neglected. Finally, the diffuse medium assumption (cf. § 2.2) is used and density dependencies are neglected.

[16] No information on the assumed relationships between the ionization states of different species are provided by Dalgarno et al. (1999).

extend up to 50 keV, remaining accurate to at least the 10 % level for hydrogen and helium.

The X-ray module of CRASH was designed to enable an accurate treatment of the effects of fast photoelectrons. It implements several changes to the algorithm described in § 2.4, which we will discuss now.

When a photon packet crosses a cell, the number of secondary ionizations each species i experiences has to be computed. This can simply be modelled as a correction term to the photoionization rate from Eq. (2.19):

$$\zeta_i' = \zeta_i + \frac{\sum_j \sum_\nu N_{\mathrm{s},i,j,\nu} \Delta N_{j,\nu}}{\delta t}\,, \tag{2.22}$$

where $N_{\mathrm{s},i,j,\nu}$ is the number of secondary ionizations of species i caused by a photoelectron with energy $E_\mathrm{k} = h\nu - h\nu_{0,j}$ released by a photon from frequency bin ν ionizing species j with threshold frequency $\nu_{0,j}$. $N_{\mathrm{s},i,j,\nu}$ is computed by interpolating a two dimensional table using E_k and the ionization state of the cell.

The heating function from Eq. (2.20) has to be corrected for the fact that only a fraction $f_{Q,i,\nu}$ of a photoelectron's energy $E_\mathrm{k} = h\nu - h\nu_{0,i}$ will go into heating:

$$\mathcal{H} = \frac{\sum_i \sum_\nu \Delta N_{i,\nu} f_{Q,i,\nu} (h\nu - h\nu_{0,i})}{\delta t \Delta V}\,, \tag{2.23}$$

Like $N_{\mathrm{s},i,j,\nu}$, $f_{Q,i,\nu}$ is computed by interpolation on a two dimensional table.

Note that this implementation assumes fast photoelectrons to deposit their energy in a single cell. For this assumption to hold at keV energies, the cell must have a column density of more than $10^{17}\,\mathrm{cm}^{-2}$ (Dalgarno et al., 1999), i. e.:

$$(n_\mathrm{H} + n_\mathrm{He}) l_\mathrm{c} \overset{!}{>} 10^{17}\,\mathrm{cm}^{-2}\,, \tag{2.24}$$

with the cell size l_c. For typical CRASH simulations, it is well justified.

The X-ray module of CRASH can use any of the models presented in § 2.5.1 to construct the tables used for the interpolation of $N_{\mathrm{s},i,j,\nu}$ and $f_{Q,i,\nu}$. For Shull & van Steenberg (1985) and Valdes & Ferrara (2008) the $x_{\mathrm{H\,II}}$ of the cell is used to represent its ionization state, while x_e is used for Dalgarno et al. (1999). See Graziani et al. (2018, App. A) for details on how the tables are obtained from the available data for each model, we will only provide a short summary here. Below 30 eV, CRASH will deposit all electron energy as heat for all models. Between 30 eV and 100 eV, Dalgarno et al. (1999) is the most reliable model, while above 100 eV there is reasonable agreement (considering the differences in atomic data used) between models. Shull & van Steenberg (1985) has been widely adopted in the literature and thus allows for comparison of CRASH to other codes. Valdes & Ferrara (2008), finally, is useful for cases where very hard photons need to be considered, as it can even be extended beyond 10 keV (Valdés et al., 2010).

2.5.3 The impact of X-rays in an idealized case

In this section we present the idealized case of a powerful, isotropic and quasar-like point source ionizing a homogeneous cosmological hydrogen/helium mixture to illustrate some of the effects of energetic photoelectrons produced by X-rays.

The point source is placed at a corner of a cube with side length $110\,h^{-1}$cMpc (comoving Mpc) at redshift $z = 7.08$ (i. e. $\sim 19\,$Mpc for $h = 0.72$). It is assigned an emissivity $Q_0 = 1.36 \times 10^{56}\,\mathrm{s}^{-1}$ and a spectral shape $S(\nu) \propto \nu^{-1.5}$, with the full spectrum extending to 3 keV and being sampled by 41 bins in frequency. We will apply cuts in frequency below, which are associated with a corresponding reduction in the number of bins. The source's emission is sampled using 2×10^8 photon packets, with a convergence run at 2×10^9 showing essentially no output changes. The cube is mapped onto a Cartesian grid of 512^3 cells and is assigned a number density of $n = 9.59 \times 10^{-5}\,\mathrm{cm}^{-3}$, with the gas initially being neutral and at a temperature of 100 K before the source is turned on and allowed to shine for $10^8\,$yr. Cosmological redshift and density evolution are accounted for. The Dalgarno et al. (1999) model is used here; a comparison to the other models can be found in Graziani et al. (2018, App. B). All parameters are chosen to be comparable to the realistic case discussed in § 2.5.4.

In Fig. 2.3 we show radial profiles from the source to the edge of the box at $6 \times 10^7\,$yr for $x_{\mathrm{H\,II}}$, $x_{\mathrm{He\,II}}$, $x_{\mathrm{He\,III}}$ and the gas temperature T from top to bottom. We show four cases including secondary ionization, with the spectrum extending to 3 keV (solid blue line), 0.1 keV (dash-double-dotted red), 0.2 keV (dash-dotted red) and 0.5 keV (triple-dotted red) respectively. Additionally, we show a case with the full spectrum but no secondary ionization (dashed black).

The location of the ionization front[17] remains roughly the same 2 Mpc for all cases, indicating that UV photons below 0.1 keV are mainly responsible for the creation of the fully ionized H II region. Extending the spectrum to 0.2 keV, results in the creation of a short ionization tail that extends to 2.5 Mpc. When going to 0.5 keV and the full 3 keV, finally, a long tail of low ionization is created beyond the ionization front. Comparison with the dashed black line shows that this is maintained primarily by secondary ionizations, whereas direct photoionization of hydrogen at these high energies is much less efficient.

Inside the ionization front, helium is mostly doubly ionized (third panel); a result of the hard shape chosen for the source's spectrum, which provides enough photons above the ionization threshold of He II. Beyond the ionization front, $x_{\mathrm{He\,II}}$ (second panel) behaves similarly to $x_{\mathrm{H\,II}}$, with the difference that its low ionization tail is maintained in large part by direct photoionization and does not as strongly depend on secondary ionization (see dashed black line).

The bottom panel, finally, shows the plasma temperature, which is more or less

[17] Somewhat arbitrarily defined as the point at which $x_{\mathrm{H\,II}}$ drops below 0.9.

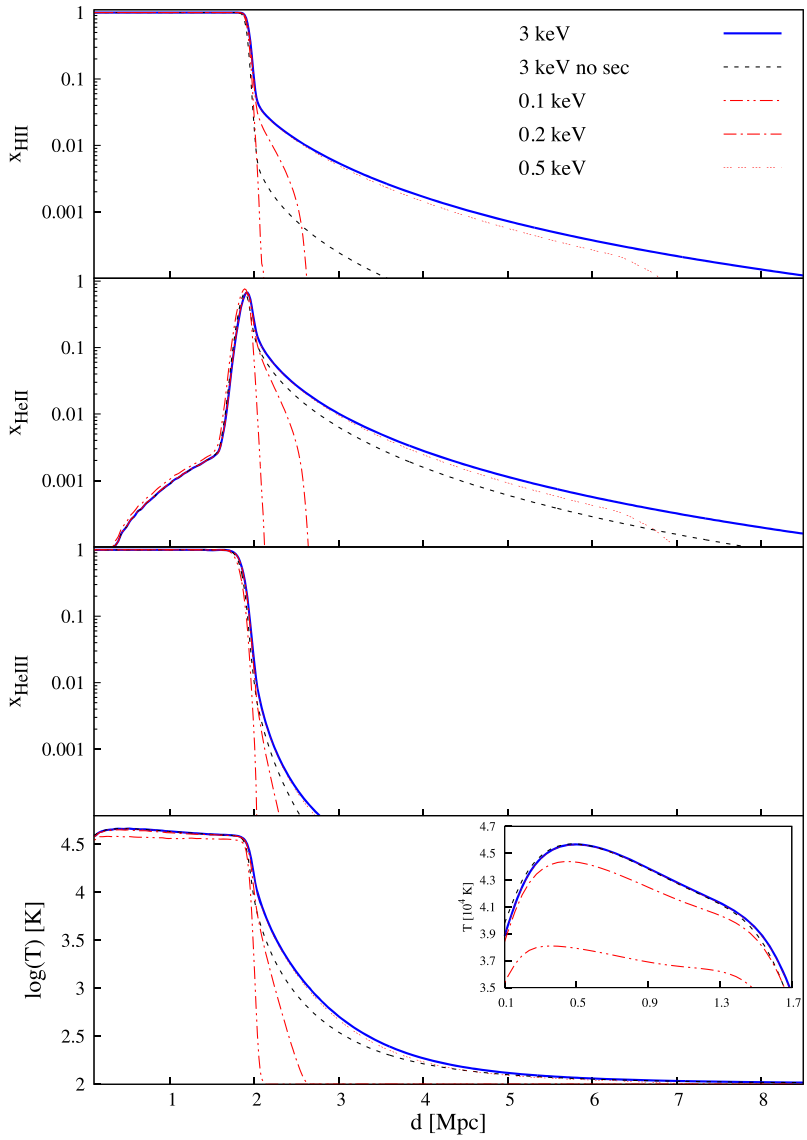

Figure 2.3: Fig. 2 of Graziani et al. (2018). Radial profiles of the ionization fractions ($x_{\mathrm{H\,II}}$, $x_{\mathrm{He\,II}}$, $x_{\mathrm{He\,III}}$) and temperature (from top to bottom) created by a quasar-like source in a homogeneous cosmological mixture of H and He at simulation time $t = 6 \times 10^7\,\mathrm{yr}$. The distance d from the source is shown in physical Mpc. The profiles are created by a spectrum extending up to 3 keV, with/without the effects of secondary electrons (blue solid/black dashed line). The dash–double-dotted red line indicates profiles created by cutting the spectrum at 0.1 keV, the dash–dotted red at 0.2 keV and the triple-dotted red line refers to a cut at 0.5 keV. The inset in the bottom panel shows a zoom of the temperature in the fully ionized region $0.1\,\mathrm{Mpc} < d < 1.7\,\mathrm{Mpc}$. See text for more details.

constant inside the ionization front. The spectral cut off has little impact on the shape of the profile, although the average value goes down to $\sim 3.7 \times 10^4$ K from $\sim 4.2 \times 10^4$ K when the cut off is set at 0.1 keV (dash-double-dotted red). Photons above 0.5 keV do not contribute to the heating in this region (triple-dotted red and solid blue lines overlap). Beyond the ionization front, the temperature profile falls off smoothly to the initial value of 100 K for the full spectrum (solid blue). Its reaction to cuts in the spectrum is similar to that of the $x_{\mathrm{H\,II}}$ profile. Turning off secondary ionization results in a lower temperature in the low ionization region, indicating that photoionizations deposit less energy in the plasma. This is caused by fewer He II ions being produced in secondary reactions and thus fewer photionizations of He II to He III taking place.

2.5.4 Ionization of the IGM by a quasar

Quasars are extremely powerful point sources of a broad spectrum of electromagnetic radiation and thus are among the most distant objects ever observed by astronomers. This radiation probes the IGM from the moment of its emission to its detection, making observed quasar spectra rich sources of information on the status (in particular the ionization status) of the IGM as a function of time (Gunn & Peterson, 1965), sometimes reaching back into the epoch of reionization (e. g. Mortlock et al., 2011; Bañados et al., 2018). The spectra of these distant quasars indicate that the IGM in their vicinity is substantially neutral. Interpreting such observations requires profound understanding of the time evolution and structure of the H II regions they form in an inhomogeneous IGM. To investigate this, we apply CRASH to the case of a powerful quasar at $z \sim 7.1$ ionizing the cosmic structure surrounding it. Parameters are chosen to be similar to the case of ULAS J112001.48+064124.3 (Mortlock et al., 2011) and this work extends Bolton et al. (2011). A similar investigation using CRASH but focusing on higher redshift and particularly considering the combined effect of a quasar and the radiation from young galaxies in its vicinity has been conducted by Kakiichi et al. (2017). The global effect of quasars and other sources on reionization, on the other hand, has been investigated by Eide et al. (2018a).

We place a source similar to ULAS J112001.48+064124.3 in a massive halo (total mass of $\sim 5 \times 10^{11}\, h^{-1}\mathrm{M}_\odot$, $R_{\mathrm{vir}} \sim 292.2\,\mathrm{ckpc} \sim 36.2\,\mathrm{kpc}$) located in a box of size $25\, h^{-1}\mathrm{cMpc}$ chosen such that the halo lies in a corner of the box at $z = 7.08$. The formation of structure in this box was simulated using `Gadget` (Springel, 2005) and the following cosmology: $\Omega_{\mathrm{m}} = 0.26$, $\Omega_\Lambda = 0.74$, $\Omega_{\mathrm{b}} = 0.0463$, $h = 0.72$, $\sigma_8 = 0.85$ and $n = 0.95$; see Bolton et al. (2011) for details. For the CRASH post processing, we map the simulation outputs onto a Cartesian grid with 512^3 cells, which results in a spatial resolution of $d \sim 48.8\, h^{-1}\mathrm{ckpc} \sim 8.4\,\mathrm{kpc}$. The source's properties are identical to those provided in § 2.5.3. We use the full spectrum up to 3 keV and the Valdes & Ferrara (2008) model. Initially, the gas is assumed to be neutral and its temperature is

set to 100 K, consistent with the value predicted by the hydrodynamical computation. For the effects of pre-ionized gas, see Kakiichi et al. (2017). We run the simulation for 10^8 yr, which corresponds to a typical quasar lifetime. See Graziani et al. (2018) for explorations of the impact of some of the parameter choices taken here.

To provide an understanding of the impact of the quasar on this volume, we first discuss some average values at simulation times 6×10^7 yr and 10^8 yr. The volume averages for the hydrogen ionization fraction are $\bar{x}_{\mathrm{H\,II}} \sim 0.162$ and ~ 0.274, with a minimum ionization fraction of 3×10^{-4} in both cases. This indicates that, while the quasar is only able to fully ionize 15 %/30 % of the box, its X-ray flux pervades the entire volume, resulting in some level of ionization everywhere. Similar considerations also apply to helium. The temperature reaches average values of 5.5×10^3 K/8.5×10^3 K. The spherically averaged profiles, are similar to those found in § 2.5.3 and feature an ionization front at ∼2.61 Mpc/∼3.2 Mpc.

Due to inhomogeneity of the IGM, the ionization structure along every line of sight (LOS) from the quasar will, in general, be different. Understanding the variability is important for the interpretation of observations, which is why we will investigate it now. In Fig. 2.4, we show a slice cut through the simulation volume in the source plane at $t = 10^8$ yr. The gas density is shown in grey, while contours corresponding to different levels of hydrogen ionization are shown in colour and reveal strong variation from LOS to LOS. In particular, we call to attention the region marked by the dashed square in the main panel, which is also shown in the zoom panels on the right, each of which displays contours of the ionization fractions and temperature as indicated. This region features the smallest extension of the ionization front because it contains one system with a surface density of $4 \times 10^{20}\,\mathrm{cm}^{-2}$ and several ten systems with surface densities $\gtrsim 8 \times 10^{19}\,\mathrm{cm}^{-2}$, which are intersected by LOS from the quasar. Note also that the helium ionization front is even less extended than that of hydrogen, since it recombines more efficiently (cf. Fig. 2.2). These observations are consistent with the observed size of the H II region (Mortlock et al., 2011) and the DLA scenario proposed by Bolton et al. (2011) for its explanation. However, only ∼0.02 % of LOS into the simulated octant fall into this regime. For $Q_0 = 1 \times 10^{57}\,\mathrm{s}^{-1}$, which might be more appropriate for ULAS J112001.48+064124.3 (Mortlock et al., 2011), the situation is very similar at $t = 10^7$ yr, but already at $t = 3 \times 10^7$ yr the overdense systems become fully ionized, resulting in too large an ionized region to be consistent with observations.

We now turn to a short statistical analysis of the 10^6 LOS that we randomly traced from the source into the simulated octant. In Fig. 2.5 we show histograms of d_{max} for different threshold values ($x_{\mathrm{th,H\,II}} = 0.001$, 0.01, 0.1, 0.9) indicated by the different line colours/styles at $t = 6 \times 10^7$ yr. d_{max} is the maximum distance from the source after which $x_{\mathrm{H\,II}}$ always lies below the corresponding threshold. First, note that the histograms for 0.1 (dashed blue) and 0.9 (solid green) are very similar, indicating an abrupt transition from fully ionized to mostly neutral taking place along the

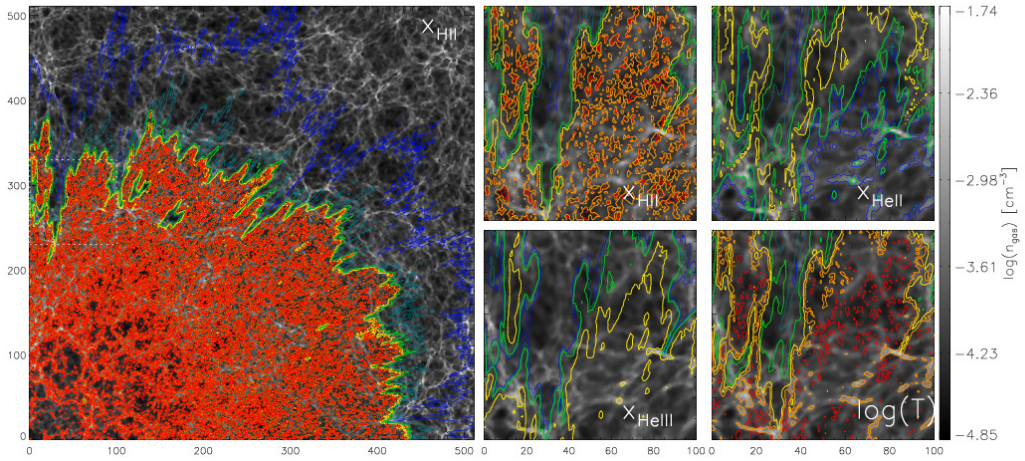

Figure 2.4: Fig. 5 of Graziani et al. (2018). Slice cut of the box intercepting the quasar source plane in a realistic IGM gas distribution at $t = 10^8$ yr. $n_{\rm gas}$ is shown as grey colour palette, while the iso-contour lines represent fronts at progressively lower ionization fractions ($x_{\rm H\,II} = 0.99996, 0.99995, 0.9, 0.1, 0.05, 0.015$ from red to blue). The box dimensions are shown in cell units ($1\,{\rm cell} \sim 0.05\,h^{-1}{\rm cMpc} \sim 8.4\,{\rm kpc}$); as a reference the virial radius of the halo is contained in the first four cells. The region indicated by the dashed square and zoomed in the four panels on the right, shows the smallest extension of the ionization front in the simulated volume. In the zoom panels, iso-contour lines of $x_{\rm H\,II}$ (top left), $x_{\rm He\,II}$ (top right) and $x_{\rm He\,III}$ (bottom left) are shown with the same colour scheme. The bottom right panel adopts the colour scheme to map iso-contour regions corresponding to $\log(T/{\rm K}) = [4.55, 4.4, 4.0, 3.5, 3.0, 2.69]$.

majority of LOS. Following the discussion in § 2.5.3, the quasar's UV flux can be associated with the shapes of these histograms. For 0.01 and 0.001 the average values of the histograms lie far beyond the ionization front. Moreover, the distributions are broader, in particular for $x_{\rm th,H\,II} = 0.001$. This indicates that also in a realistic gas distribution, a quasar's X-ray flux creates an extended low ionization layer beyond the ionization front. The extent of both the ionization front and this layer exhibit correlated and strong spatial variation, indicating significant spatial fluctuations in the UV and X-ray fields pervading the surrounding IGM.

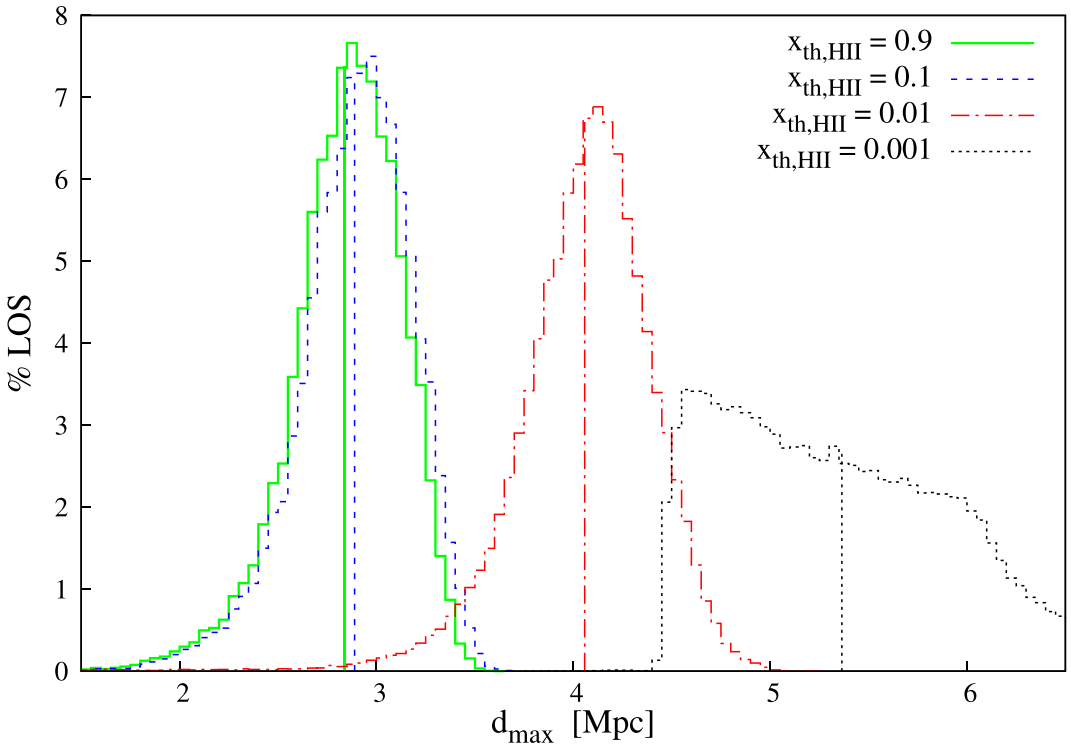

Figure 2.5: Fig. 6 of Graziani et al. (2018). Distributions of LOS over $d_{\max}$, the maximum distance (physical Mpc) at which $x_{\mathrm{th,H\,II}} = 0.9$ (solid green line), 0.1 (dashed blue line), 0.01 (dash–dotted red line), and 0.001 (dotted black line). Vertical lines show the average values of each distribution. The figure refers to simulation time $t = 6 \times 10^7$ yr. See text for details.

2.6 Radiation hydrodynamics

In this chapter, we have been concerned with describing the temporal and spatial evolution of a radiation field and a static matter distribution[18] it propagates through. This is a common and often well justified assumption in astrophysics, since changes in the radiation field propagate at the speed of light, which is much higher than the typical flow speed of matter (e. g. Ercolano et al., 2005; Verstocken et al., 2017; Eide et al., 2018a; Vandenbroucke et al., 2018) and it allows to simulate the dynamics of matter first and perform RT in post-processing. An approach which results in a significant reduction of the complexity of numerical models and the cost of individual simulation runs.

[18] Of course, the unresolved thermal motion of individual particles is considered, but no large scale motion.

However, in physical reality the radiation field carries energy and momentum, which, as discussed in § 2.2, it can transfer to the matter and thus affect its dynamics. Photo-electric heating by ionizing radiation, for example can result in increasing thermal pressure and consequently the expansion of heated material. Cosmic dust, as we will discuss in Ch. 3, efficiently absorbs and scatters electromagnetic radiation over broad frequency ranges, and can therefore be driven by radiation pressure. It can communicate this pressure to the ISM gas via collisions and thus launch so called momentum-driven winds (e. g. Murray et al., 2005). On the other hand of course, matter dynamics, affect RT. For example if a shock heats up and collisionally ionizes a plasma, reducing its opacity to ionizing radiation.

This is to say, naturally, that RT and matter dynamics are coupled. While a comprehensive discussion is far beyond the scope of the present work, below we will very briefly outline how a combined treatment of matter dynamics and radiation can be achieved in the context of simulations of star/galaxy formation and we will mention some efforts undertaken in this direction.

As we saw in § 2.2, the baryonic matter in the ISM/IGM forms dusty plasmas. Although not pertinent to our discussion so far, magnetic fields seem to pervade these plasmas on virtually all scales (e. g. Han, 2017). The dynamics of such magnetized plasmas can be described by the equations of magneto hydrodynamics (MHD). The theory of coupling dynamics and RT in ISM/IGM, then, is radiation hydrodynamics. An excellent introduction to this complex field can be found in Pomraning (1973, Ch. IX).

Modern cosmological codes (e. g. Springel, 2005; Weinberger et al., 2019) are based on MHD theory but do generally not follow radiation explicitly, treating it in an approximate way in the form of a uniform background field (e. g. Haardt & Madau, 2012) instead. This is often necessary to keep computational cost at an acceptable level but it is a strong assumption since, for example, the emission of ionizing radiation by young stars, one of their main feedback channels, is strongly affected by shielding and thus not uniform. Consequently, in recent years much effort has been put into the development of radiation hydrodynamics codes and successful coupled simulations of galaxy evolution have been run (e. g. Petkova & Maio, 2012; Gnedin, 2014; Maio et al., 2016; Rosdahl et al., 2018; Kannan et al., 2019). However, due to the high computational cost associated with exact transfer methods such as MCRT, in all these works approximations, usually based on the moment methods mentioned above were used. MCRT hydrodynamics simulations have, to the best of our knowledge, only been conducted on smaller scales so far (e. g. Ali et al., 2018; Lund et al., 2019; Sartorio et al., 2019).

Chapter 3

Cosmic dust

Already in 1683, Giovanni Domenico Cassini postulated that the phenomenon of zodiacal light is caused by dust in interplanetary space scattering sunlight (Hockey et al., 2014; Grün et al., 2019). The existence of dust grains in interstellar space, on the other hand, was first hypothesized in the 1920s and 30s to explain the extinction of light from distant Galactic stars[1]. Since that time, an enormous body of observational evidence in support of the existence of cosmic dust has been constructed and is continuously being extended, investigating absorption, scattering and emission of electromagnetic radiation by grains in bands ranging from X-rays to microwaves. The evidence includes, for example, observations of star-forming regions (e. g. Churchwell et al., 2009), the diffuse Galactic ISM (e. g. Schlafly et al., 2016) or our Solar System (e. g. Leinert et al., 1981). It has thus become increasingly apparent that, at least in star-forming galaxies, dust is nearly ubiquitous in the local Universe. Improved instrumentation has led to the detection of dust in galaxies at increasingly earlier times in the history of the Universe, culminating in recent detections of dusty galaxies in the epoch of reionization (e. g. Tamura et al., 2019). Finally, there is evidence of dust being present in the IGM from early on in the history of the Universe as a result of winds and mechanical feedback from galaxies (e. g. Imara & Loeb, 2016).

Fig. 3.1 shows an optical (left) and a far infra-red (IR, right) image of the nearby Andromeda galaxy, demonstrating dust absorption and emission respectively: note how optically dark clouds in the centre and spiral arms of the galaxy appear bright in the far IR.

While dust was initially frequently seen as a nuisance that necessitates obscuration corrections of observations[2], its potential as a diagnostic of the physical conditions in environments it is present in was recognized as more sophisticated observational instrumentation became available. Realizing this potential requires understanding of

[1] Schalén (1929) may have arrived at this conclusion first, however, Trumpler (1930), who presumably postulated it independently, is frequently credited; see also Hockey et al. (2014).

[2] Walter Baade, when asked if he would become an astronomer again were he to get a chance to relive his life, is said to have answered somewhat wryly and in reference to the environment dependence of the dust extinction curve (see § 3.1) "Only if the ratio of total to selective absorption is everywhere the same.". Unfortunately, despite considerable research effort, no official account of this anecdote could be found.

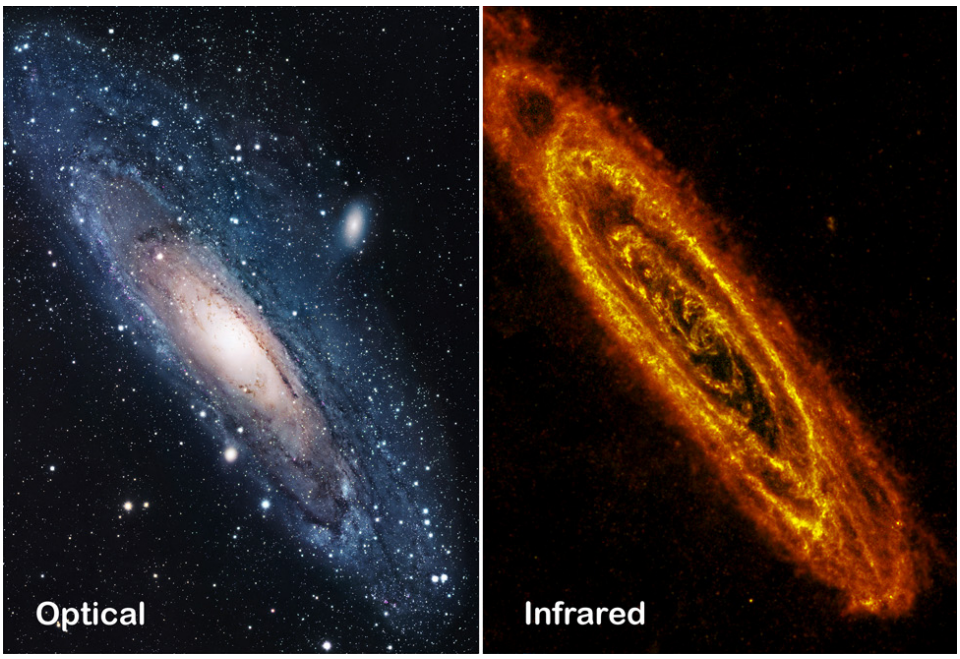

Figure 3.1: The nearby Andromeda galaxy in the optical (left) and far IR (right). ©: ESA/Herschel/PACS/SPIRE/J. Fritz, U. Gent (IR); R. Gendler (optical); images cropped by author.

the physics at play, which, in combination with a desire to better understand the nature of dust itself, has been driving the development of theoretical dust models (see § 3.5) informed not only by electromagnetic observations but also by laboratory experiments on candidate grain materials (e. g. Jäger et al., 2009) and even samples of presolar, interplanetary and interstellar grains found on Earth and in the Solar System (e.g. Srama et al., 2011; Amari et al., 2014; Grün et al., 2019).

Such detailed investigations led to the understanding that cosmic dust plays a potentially critical role in galactic evolution. Grain surfaces can provide catalytic sites for chemical reactions (e. g. molecule formation) and the existence of grains, naturally, means that some fraction of elements[3] is removed from the gas phase. The fraction of sequestered material is likely variable, depending on physical conditions with a continuous exchange between the solid and gas phases taking place (see § 3.4). Moreover, grains can shield molecules from electromagnetic radiation, preventing their dissociation. Dust, therefore, is a driver of the chemistry of astrophysical

[3]This will mostly be heavy elements, although H can be integrated into solids if it chemically bonds to heavier elements. He is chemically inert and volatile and therefore not likely to be present in solids.

plasmas. The formation of H_2 molecules, for example, is believed to frequently take place on grain surfaces. Thermal emission from grains themselves and de-excitation emission from H_2 are important cooling channels for dense molecular clouds, the birthplaces of stars, indicating that dust plays an important role in regulating star formation. Conversely, energetic photons being emitted by young stars and absorbed by grains will contribute to plasma heating via the release of photoelectrons. Finally, grains can influence plasma dynamics by coupling to magnetic fields and by capturing radiation pressure (see § 2.6).

Despite these extensive advances in our understanding, the problem of cosmic dust is by no means solved; much more observational, theoretical and experimental effort will be required to construct a conclusive and detailed picture of its composition, evolution and interplay with gas and radiation the different environments it is observed in.

In this chapter, we will first briefly revisit some observational results regarding dust in the local Universe (§ 3.1). Then we will summarize a recent effort in reconstructing the dust distribution in the vicinity of the Solar System (§ 3.2, Leike et al. 2020a). Afterwards, we will provide an overview of some observational results on dust in the early Universe (§ 3.3), before summarizing what is known about the life cycle of dust (§ 3.4) and providing some detail on a dust model that enables us to describe its interaction with radiation (§ 3.5). Finally, we summarize a numerical study on how galaxies build up their dust content (§ 3.6, Graziani et al. 2020). Excellent general references on observations and physics of dust are Krügel (2002), Whittet (2003), Tielens (2005), Krügel (2007) and Draine (2011a).

3.1 Dust in the local Universe

One of the fundamental pillars of the study of interstellar dust is its wavelength dependent extinction (e.g. Fitzpatrick, 1999), the extinction curve (see Fig. 3.2), measured by comparing a star's observed spectrum to its expected spectrum. Although the exact dependence varies from star to star, a very general finding is that dust preferentially extinguishes blue, green and UV light as opposed to red and IR light at longer wavelengths (e.g. Draine, 2011a).

The detailed dependence of the extinction on wavelength is sensitive to the shape distribution of grains and to their composition. The fact that it varies from line of sight to line of sight indicates variations in grain populations, which are not yet well understood and are still actively being investigated (e. g. Gordon et al., 2019). However, since extinction generally rises towards the UV down to wavelengths of $0.1\,\mu m$, small ($< 0.015\,\mu m$) grains must be abundant; if all grains were larger than these shortest wavelengths, the geometric optics limit would be reached and UV extinction would be grey, i. e. constant.

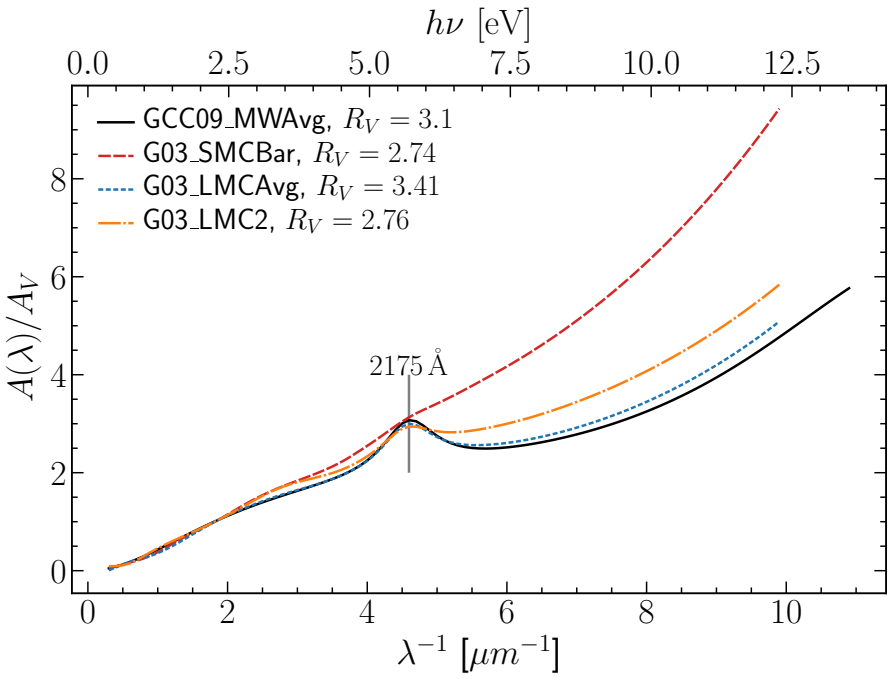

Figure 3.2: Average extinction curves for the Milky Way (MW, black solid), the bar of the Small Magellanic Cloud (SMC, red dashed), and the Large Magellanic Cloud (LMC, blue dotted). Also shown is the extinction curve for the LMC2 supershell (orange dash-dotted). Note that the resolution is not high enough to see features other than the 2175 Å bump (where present). The ratio of visual extinction to reddening, $R_V = A_V/(A_B - A_V)$, is shown for each curve. The data were taken from the `dust_extinction` Python package. See text for more details.

Light from some fraction of the observed stars in our galaxy is found to be polarized. It is difficult to identify a plausible intrinsic mechanism to explain this. Moreover, the degree and direction of polarization exhibit spatial correlation and more extinguished stars show a higher degree of polarization, suggesting that the root cause is to be found in the ISM through which the light propagates. The commonly accepted explanation of this phenomenon, then, is that grains are not spherical and are by some mechanism (e. g. the interstellar magnetic field) aligned on large scales, such that they preferentially extinguish a certain mode of linear polarization. The degree of polarization is found to decline towards the UV, indicating that the grains causing it reach the geometric optics limit and extinguish all polarization modes equally efficiently. One can conclude from this that there is a population of larger (∼0.1 µm)

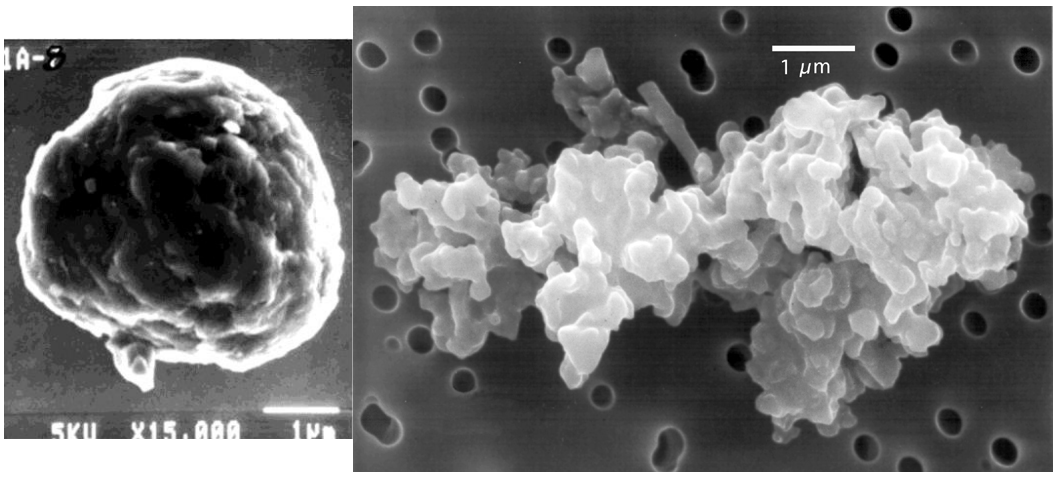

Figure 3.3: A presolar graphite grain extracted from a meteorite (left, Messenger et al. 2014, published under CC BY-NC-ND 4.0) and a porous chondritic interplanetary dust particle collected from the stratosphere composed of minerals and organic material (right, Jessberger et al. 2001, published under CC BY 1.0). The images were taken using electron microscopes; note that the scales as shown are roughly equal.

grains that are non-spherical and aligned to a substantial fraction, whereas smaller grains are either not aligned or spherical, with the latter being implausible.

Apart from the above, the shapes and structures of cosmic dust grains are observationally virtually unconstrained (but see Kirchschlager & Bertrang 2020). Presumably they are distributed over a range from almost perfect homogeneous spheres to "fluffy", porous and layered irregular aggregates with the distributions varying from environment to environment. Fig. 3.3 shows two examples of grains collected from the Solar System. As such, they are unlikely to be representative of general interstellar grain populations (e. g. being several micrometers in size), but they illustrate the radically different possible shapes and structures.

Determining the exact chemical composition of dust, even in the ISM of our Galaxy, has proven challenging and is still an active field of research. An approach that can provide insights into the atomic building blocks of grains is what is referred to as interstellar depletion. The abundance of certain elements in the gas phase as determined from spectroscopy is found to be lower than expected from the composition of stars (e. g. Jenkins, 2009; Ritchey et al., 2018). Depletion varies from line of sight to line of sight and from element to element and the "missing" material is assumed to be locked up in solid grains (e.g. Whittet, 2010), providing abundance constraints for dust models (see § 3.5). C, being around 50 % depleted, along with

the strongly depleted Mg, Si, and Fe and the more weakly depleted but abundant O, presumably contribute most of the dust mass.

The spectroscopic approach to investigating composition, i. e. the unique identification of materials by features in emission or absorption spectra, has successfully and for many years been applied by astronomers to identify ions, atoms and small molecules (e. g. Osterbrock & Ferland, 2006; Ferland et al., 2017; Peimbert et al., 2017). As one moves to larger molecules and solid grains, however, this becomes increasingly difficult. Their spectra resemble continua, showing few distinctive features, while those that do exist are broad, indicating, as one would expect, a certain degree of chemical impurity and making conclusive identification difficult. We will briefly mention some almost universally observed spectral features that are usually associated with certain chemical bonds or compounds, however a detailed discussion is far beyond the scope of this work.

A prominent and frequently observed dust feature is a strong peak in extinction centred almost universally at 2175 Å but with width varying from line of sight to line of sight (cf. Fig. 3.2). The most likely carrier has been identified as some form of sp^2-bonded carbonaceous material such as graphite. It is, however, uncertain if and how a highly structured material like graphite could survive in sufficient abundance in interstellar conditions without being amorphized. Also note that lines of sight have been observed where this feature is not present (e. g. Gordon & Clayton 1998 and see Fig. 3.2), which could be a sign of possible dust evolution indicating the destruction of the carriers of the 2175 Å feature (e.g. Weingartner & Draine 2001a, hereafter WD01a).

At longer wavelengths of 10 µm and 18 µm, features associated with silicates are frequently seen in absorption and emission. Silicates is a generic term here, referring to minerals based on SiO_4, which is assumed to produce both features, such as for example Mg_2SiO_4. The features are generally not sharp, indicating that their carriers are likely amorphous silicates with a low degree of crystallinity (e. g. Kemper et al., 2004). In lines of sight through dense molecular clouds, strong extinction at 3.1 µm, associated with H_2O ice, is observed. This feature is again a sign of grain evolution since it is generally not present in extinction curves through diffuse media. It is interpreted as an indication that refractory grain cores acquire ice mantles in dense, cold clouds, which are presumably lost to photo-desorption in the unshielded conditions of the diffuse interstellar medium.

IR emission spectra of dusty media show several conspicuous features in the range 3 µm to 15 µm which are widely attributed to vibrational transitions in polycyclic aromatic hydrocarbons (PAHs), planar molecules consisting of a number of benzene rings (e. g. Li 2020 but see Jones 2018). Their possible sizes vary considerably, making them intermediates between molecules and grains. Star-forming galaxies can emit a significant fraction of their IR power in the aforementioned features (e. g. Smith et al., 2007), suggesting that their carriers are excited by UV radiation from young stars.

The features are generally associated with atomic gas, while they are systematically suppressed in ionized regions (e. g. Chastenet et al., 2019), indicating that their carriers are destroyed either by ionizing radiation or collisions with hot electrons or, most likely, by a combination of both (see also § 3.5.3). In molecular gas, carrier presence is debated, since the absence of the emission features sometimes observed in molecular regions could be caused by a lack of exciting irradiation instead of the absence of carriers (see, e.g., Ferland et al. 2017, § 5.3 and Chastenet et al. 2019). If the carriers are indeed PAHs, they can contribute to or even dominate the 2175 Å extinction feature[4] by virtue of their carbon skeletons (e. g. WD01a), which would alleviate the need for large quantities of interstellar graphite.

The fact that grains efficiently extinguish UV light has important consequences for the observation of recent star formation, traced by massive and short-lived stars, which emit most of their energy in the UV (e.g. Kennicutt & Evans 2012). These stars are observed to form in groups (OB associations) in dense, dusty molecular clouds (e.g. Garay & Lizano, 1999; de Zeeuw et al., 1999), so that a large fraction of their radiation is often absorbed by dust, which re-emits in the IR, impeding direct observation in the optical/UV bands (see also Fig. 3.1 and § 3.3) and changing galaxy colours (e.g. Lewis et al., 2017).

Though observationally less well constrained, models predict a large dust cross section also in the ionizing UV (13.6 eV to 200 eV; see § 3.5.2). This has interesting implications for the formation of H II regions by ionizing UV radiation, one of the feedback channels of massive stars on the ISM. Despite a long series of studies investigating their spectral line diagnostics; structure, evolution and physical status of the ionized gas in these regions still remain subjects of intense theoretical and observational activity (see e.g. O'Dell 2001; Whitney et al. 2004; Purcell et al. 2009; Winston et al. 2011; O'Dell et al. 2017). Galaxies of the Local Group offer a wide range of H II regions accessible at a level of detail comparable to Galactic observations (Kennicutt, 1984; Massey & Hunter, 1998), but located in differing ISM environments, e. g. with quiescent star formation as observed in M31 (Azimlu et al., 2011) or M33 (Relaño et al., 2016).

Fig. 3.4 shows Herschel's[5] dust-emission-tracing IR view of the RCW 120 bubble located at ~ 1300 pc from Earth. The central structure is on the order of 1 pc in size. It is interpreted as the H II region created by a young star located near the centre of the bubble (not visible in IR) and moving w.r.t. the surrounding material. The star's radiation heats and ionizes the surrounding cold gas and dust, with the resulting thermal and radiation pressure creating a cavity and disrupting its birth cloud.

The connection between the size of H II regions and their electron number density (the so called size-density relation) in observational samples has been investigated

[4] This might, of course, also be true of other carriers.

[5] `http://www.esa.int/Science_Exploration/Space_Science/Herschel`

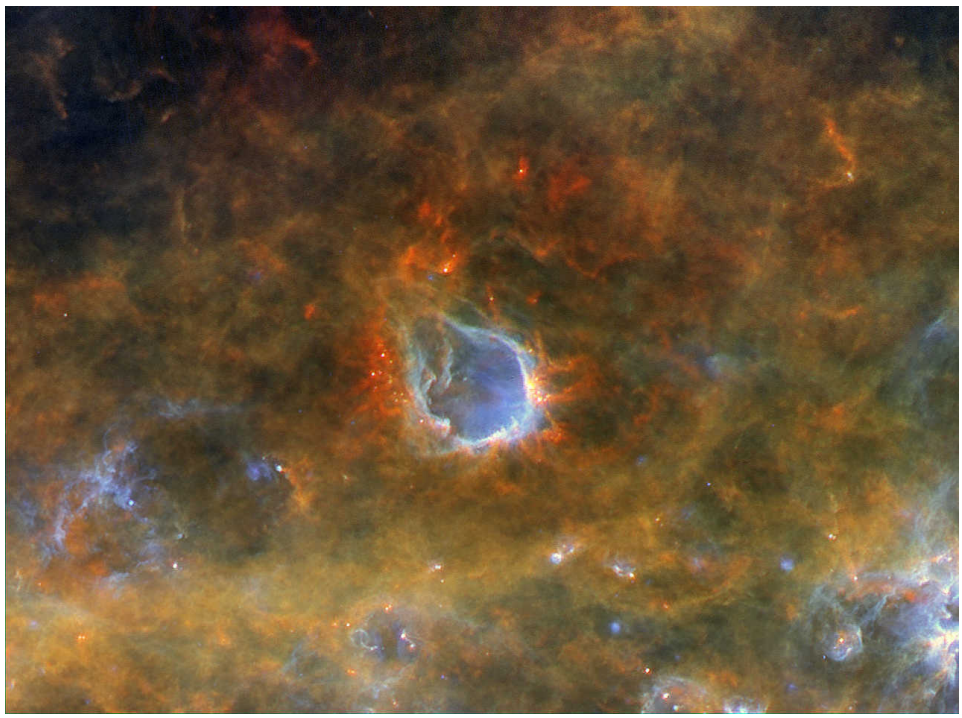

Figure 3.4: The dusty H II region RCW 120 as seen by the Herschel telescope. This is a composite image showing 70 µm (blue), 160 µm (green) and 350 µm (red) data. ©: ESA/Herschel/PACS, SPIRE/Hi-GAL Project; G. Li Causi, IAPS/INAF, Italy.

as tracer of their physical status and structure (see Hunt & Hirashita 2009; Draine 2011b and references therein). Dust certainly plays a role in shaping this relation and has been recognized as crucial to its deviation from pure Strömgren sphere (Strömgren, 1939) expectations (e.g. Inoue et al. 2001; Arthur et al. 2004); see also Ch. 4.

Figs. 3.1 and 3.4 reveal the complex spatial distribution of cosmic dust on different scales. Understanding this distribution is paramount in the interpretation of any observation in electromagnetic bands affected by dust, since radiative transfer models are highly sensitive to it. If both gas and dust have to be accounted for, as in the study of H II regions, additionally the spatially varying relative abundance of gas and dust, usually expressed in the gas-to-dust mass ratio (GDR) or its inverse the dust-to-gas mass ratio ($\mathcal{D}$), has to be accounted for. The average GDR of the MW is around 100, but observations have shown it to vary greatly from ~ 10 to $\sim 10^6$ depending on the environment (e.g. Vuong et al. 2003; Draine et al. 2007; Sandstrom et al. 2013; Rémy-Ruyer et al. 2014; Liseau et al. 2015; Owen & Barlow 2015).

As shown in Fig. 3.1, the dust distribution in galaxies in the local Universe can

be studied using spatially resolved 2D imaging; see, e.g., the DustPedia[6] project. Deriving 3D distributions from such imaging is challenging and not uniquely possible (e. g. De Looze et al., 2014). The only galaxy for which detailed 3D mapping of the ISM is in principle possible is the MW. In § 3.2, we will briefly describe a recent effort in reconstructing the local 3D dust distribution (Leike et al., 2020a).

3.2 The distribution of dust in the vicinity of the Solar System

Surveys of the Milky Way such as Gaia[7] provide unprecedented opportunities to map its 3D structure and ISM. Leike & Enßlin (2019), for example, used the positions and extinction values of stars provided by Gaia to reconstruct the distribution of dust with a resolution of $\sim 2.3\,\mathrm{pc}$ in a $(600\,\mathrm{pc})^3$ box centred on the Sun. Anders et al. (2019) have since combined observational data of the Gaia, ALLWISE, PANSTARRS and 2MASS surveys to construct a consistent dataset of millions of stars including, among other measurements, their position and extinction. This improved dataset has been used by Leike et al. (2020a) to reconstruct the dust distribution in an $800\,\mathrm{pc} \times 800\,\mathrm{pc} \times 600\,\mathrm{pc}$ box with a resolution of $\sim 1\,\mathrm{pc}$. Compared to Leike & Enßlin (2019), the increased box size and resolution have resulted in a factor of ~ 30 more degrees of freedom, while the improved stellar catalogue has provided $\sim 35\,\%$ more sources. The correspondingly increased computational cost and memory requirements necessitated the restructuring and parallelization of a part of the previously used numerical implementation, which was performed within the scope of the present work.

In § 3.2.1 we will briefly describe the methodology used for the dust reconstruction and in § 3.2.2 we will show and discuss selected results.

3.2.1 Information field theoretical inference applied to cosmic dust

The positions and extinctions of stars as provided by Anders et al. (2019), constitute measurement data d on a scalar field s defined over interstellar space; specifically the Gaia G-band dust extinction optical depth density $s(x) = \tau_{\mathrm{e}}^{G}(x)/l$, where x is a point in interstellar space and l is a physical path length (e. g. 1 pc is a reasonable choice).

Information field theory (IFT, e. g. Enßlin 2019) provides a Bayesian framework to make probabilistic statements about field configurations given observational data and some prior assumptions on field properties (e. g. s is positive and exhibits spatial correlation). These assumptions provide important input in favouring physically

[6] `http://dustpedia.astro.noa.gr/`
[7] `https://sci.esa.int/web/gaia`

plausible field configurations among those consistent with the data, since fields often have infinitely many degrees of freedom and thus cannot be uniquely constrained by a finite set of measurements. In practice, the number of degrees of freedom has to be reduced by discretising the field in question, while making sure that the continuum limit is reached, i. e. that quantities of interest are robust against further refinements.

Numerical variational approaches using IFT have been successfully applied to infer fields. Recently, Knollmüller & Enßlin (2019) proposed Metric Gaussian Variational Inference (MGVI), an efficient and accurate inference algorithm which was employed in Leike et al. (2020a) to reconstruct s. For reasons of brevity, we will not go into further detail, only briefly describing the numerical contribution made in the context of this work in § 3.2.1.1 and referring the interested reader to the original literature.

Note that our reconstruction of s is free of assumptions on dust properties, only when deriving quantities from it, e. g. the dust mass density, do such assumptions have to be made. Given current uncertainties (cf. § 3.1), this is a highly desirable property.

3.2.1.1 Computing the response

Assume the positions of a set of stars to be known exactly and the extinction of these stars to be our observational data d. The data are then given by

$$d = R(s) + n \tag{3.1}$$

where R is the response of the instrument to the field s and n denotes stochastic measurement noise. For a star i located in direction Θ_i at distance r_i:

$$R_i(s) = \int_0^{r_i} s(r\Theta_i)\,\mathrm{d}r\,. \tag{3.2}$$

For a discretised field, naturally, the line integral is represented by a sum. The computation of this response and its adjoint operation, which can be thought of as smearing out a given extinction over a path, has to be performed frequently for millions of stars in the MGVI approach to obtain s, such that it accounts for a large fraction of the total computational cost. For the real data, additionally the uncertainty in r_i has to be considered[8], but fundamentally the problem does not change (see Leike et al., 2020a).

Leike & Enßlin (2019) computed the response and its adjoint using a readily available Python sparse matrix implementation. Since stellar positions are fixed, this approach allows to pre-compute the matrices and only perform a multiplication on the fly. However, it requires large amounts of memory, scaling as the product

[8] Θ_i has comparatively negligible uncertainty.

of the number of stars and the number of resolution elements of the field. When considering the stellar catalogue of Anders et al. (2019), the requirement became prohibitive, necessitating the implementation of a custom solution. This was done in the form of a Fortran extension module[9] for Python, which computes the response and its adjoint on the fly using 3D ray-tracing.

The ray-tracing approach requires negligible amounts of memory in addition to what has to be stored in any case (e. g. s). Moreover, it is readily shared-memory-parallelizable over different stars i. The adjoint operation incurs some overhead, however, as atomic operations have to used to avoid race conditions when computing a new estimate of s. After considerable performance analysis and improvement, the ray-tracing approach performed equally fast as the sparse matrix approach on a single core, while showing good scaling up to 20 cores on the hardware used. This allowed for the efficient use of all cores on single shared memory nodes and for additional parallelization (see Leike et al., 2020a), significantly reducing the time to solution.

3.2.2 Results and discussion

We were able to reconstruct s in an $800\,\mathrm{pc} \times 800\,\mathrm{pc} \times 600\,\mathrm{pc}$ box centred on the Sun with a resolution of $\sim 1\,\mathrm{pc}$. Since part of the reconstruction scheme requires the assumption of periodic boundary conditions, we recommend cutting off the outer 30 pc, beyond which correlations should be minimal. This results in an effective volume of $760\,\mathrm{pc} \times 760\,\mathrm{pc} \times 540\,\mathrm{pc}$.

The left panel of Fig. 3.5 shows a Mollweide projection of the dust extinction optical depth in the Gaia G-band in our box as seen from the position of the Sun. The right panel shows the optical depth integrated along the z-direction, i. e. perpendicular to the Galactic plane, with the Sun located at the centre. The maps show dust clouds and filaments ranging from a few to several hundred parsec in size. Although the Local Bubble is clearly visible in the right panel, the reconstructed amount of dust extinction here is relatively high, which might be an artefact (see Leike et al., 2020a).

We hope that summary statistics our reconstruction (see Leike et al. 2020a) are helpful in constraining simulations of the ISM, which reach similar resolution. Moreover, the map might prove useful in understanding the foreground to the CMB created by dust microwave emission. Finally, the combined knowledge of source positions and properties as well as the dust distribution, provides unprecedented opportunities for observationally well constrained radiative transfer investigations to be conducted in the future.

[9] `https://gitlab.mpcdf.mpg.de/mglatzle/gda_futils`

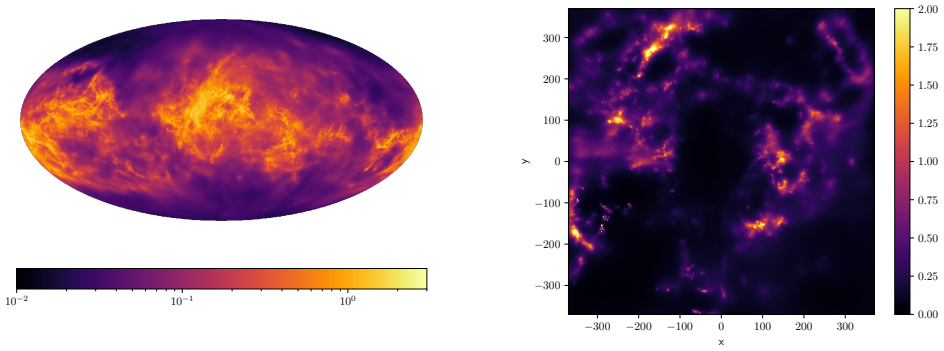

Figure 3.5: Maps of our reconstructed dust extinction optical depth in the Gaia G-band. **Left:** Fig. 2 (a) of Leike et al. (2020a). A Mollweide projection of the entire box as seen from the position of the Sun. **Right:** Fig. 9 (a) of Leike et al. (2020a). The optical depth along a direction perpendicular to the Galactic plane with the Sun being located at $(0, 0)$.

3.3 Dust in the early Universe

The IRAS and COBE space missions allowed for the first time to measure the all-sky IR to sub-millimetre emission of the Universe and showed that it is comparable in energy density to the optical to UV emission. In combination with optical surveys, these measurements proved the existence of a population of star-forming galaxies, significantly obscured by dust. These galaxies have since been the subject of a large number of investigations; see Casey et al. (2014) for a recent review. It has become apparent that at least out to redshifts 2 and 3, a time at which the star formation density of our Universe peaked, only a fraction of the optical/UV emission from young stars can be observed directly (e. g. Madau & Dickinson, 2014). Sub-millimetre ground based instrumentation, in large part specifically ALMA[10] (Hodge & da Cunha, 2020), has allowed to push the limit for dust emission and metal line detections further and recently even well into the epoch of reionization (e. g. Bertoldi et al., 2003; Venemans et al., 2015; Watson et al., 2015; Willott et al., 2015; Laporte et al., 2017; Venemans et al., 2017; Hashimoto et al., 2019; Tamura et al., 2019). The number of such detections remains relatively low and they are biased towards luminous and massive objects like star burst galaxies or those hosting powerful active nuclei. Nevertheless, they show that even "normal" star-forming galaxies[11] can be chemically enriched and very dusty early on in the history of the Universe (e. g. Watson et al.,

[10] `https://www.almaobservatory.org`
[11] We use normal to refer to objects that form a few tens of solar masses of stars per year.

2015). Thus, dust has been closely linked to star formation and galaxy evolution for a large part of the history of the Universe, which poses interesting challenges for theoretical studies of galaxy formation and reionization; see § 3.6 and Ch. 6.

Constraining the properties of dust in distant objects is even more challenging than doing so locally. Spectroscopy of powerful background quasars allows to measure the relative abundances of heavy elements in the gas phase in foreground objects to large distances. In contrast to the case of Galactic observations, intrinsic abundances are unknown for these objects, which exacerbates the understanding of depletion onto dust grains (e. g. De Cia et al., 2016). Background quasars also provide a direct way to measure dust extinction in foreground galaxies (e. g. Kulkarni et al., 2016), however these measurements are rare and suffer from uncertainties in the prediction of the intrinsic spectrum of the background source. These limitations also apply when using spectra of gamma ray bursts to study the dust content and properties of their hosts (e. g. Zafar et al., 2018). If individual sources can not be resolved, as is the case for the stars of distant galaxies, extinction curves can not be measured; instead only "effective extinction" or attenuation curves[12] are available. In addition to the intrinsic extinction properties, these depend on a number of parameters (dust and star distributions, intrinsic properties of stellar populations, radiative transfer effects, ...), which are challenging to disentangle (e. g. Calzetti et al., 2000; Reddy et al., 2015, 2016; Salim & Narayanan, 2020).

Naturally, also measuring and interpreting dust *emission* spectra from distant objects is far more challenging than doing so locally. While the IR emission features associated with PAHs have been detected out to $z \sim 4$ (Riechers et al., 2014), towards the highest redshifts only continuum detections are possible.

The nature of dust grains at high redshift, therefore, while likely different from that in the local Universe due to differing ISM conditions, has to be considered an open question at this point. Future space borne far IR instruments such as SPICA[13], JWST[14] and OST[15] are likely to revolutionize our understanding of this fascinating field, while also providing a wealth of new insights on local Universe dust.

3.4 The life cycle of cosmic dust

Similarly to its composition, the life cycle of cosmic dust is actively being researched and a large number of uncertainties concerning it remain. In this section, we aim to present, without claiming completeness, a short synopsis of important concepts, providing some context for the observations summarized above and the theoretical

[12] See `https:/ / www.github.com/ karllark/ dust_extinction` and `https:/ / www.github.com/karllark/dust_attenuation` for more information.

[13] `https://www.spica-mission.org`

[14] `https://www.jwst.nasa.gov`

[15] `https://asd.gsfc.nasa.gov/firs/`

work discussed below and in the following chapters; see Krügel (2002), Whittet (2003), Krügel (2007), Draine (2011a), Hirashita (2013) and references therein for more details.

Different forms of stellar ejecta, for example outflows from asymptotic giant branch (AGB) stars or remnants of supernovae (SNe), show observational evidence of the presence not only of molecules but also of dust grains (e. g. Rho et al., 2015; Cherchneff & Sarangi, 2017; Dell'Agli et al., 2019). This "stardust" is most likely comprised of particulates of refractory elements and compounds condensing out of the gas phase as the ejecta cool (e. g. Cherchneff & Dwek, 2009; Marassi et al., 2019). Conditions conducive to this process (high density, low temperature, high abundance of refractory elements) are otherwise scarce on galactic scales, such that these are primary candidates for the initial production sites of grains. Once created, a stardust grain might be quickly destroyed again, e. g. by the pulsating atmosphere of its parent AGB star or by the reverse shock passing through its parent SN remnant. Alternatively, it will flow into the ISM, where it begins a complicated and not yet well understood life, governed by collisions with photons, ions, molecules and other grains. Most grains are presumably spun up by these collisions, since they are likely to impart a non-vanishing net angular momentum. Often, they will have a preferential direction, imparting a non-vanishing net linear momentum and thus providing forces (e. g. radiation pressure, gas drag) which, in combination with Lorentz forces and gravity, govern the large scale movement of grains through the ISM. Often but not always, gas and dust are well coupled by collisions so that they move coherently (e. g. Laibe & Price, 2014). A grain can thus, possibly multiple times, pass from one environment of the ISM to another, being subjected to different physical processes in each, a selection of which we describe below.

Collisions of particles with grains can result in them sticking to the grain surface. Electrons, for example, can negatively charge grains (see Ch. 5). Grains can grow by accreting refractory ions or compounds from the gas phase and incorporating them into their solid structure. They can also accrete more volatile material and form mantles around a refractory core. Several grains can coagulate, resulting in large and irregular shapes. Finally, ions can stick to the surface of grains and use them as catalysts, forming compounds that are released back to the gas phase by the energy freed up in the reaction. These processes are more likely to take place in dense and cool environments (e. g. Hirashita, 2013).

More violent collisions tend to happen in, e. g., shocks or hot plasmas (e. g. Draine & Salpeter, 1979b). In a process referred to as sputtering, collisions with plasma constituents return atoms from grain surfaces to the gas phase. Sputtering can occur where plasma and dust have high relative velocities or when dust is embedded in a hot plasma, in which case it is referred to as thermal sputtering (e. g. Draine, 2011a). Violent grain-grain or cosmic ray-grain collisions can shatter grains or even directly vaporize them, completely returning their material to the gas phase. A further

possible fragmentation process is the rotational disruption of grains spun up by collisions with plasma constituents and/or photons to such a degree that centrifugal forces overcome the tensile strength of the grain material (Hoang, 2019; Hoang & Lee, 2019).

The absorption of photons by grains (see Ch. 4) will heat them, can result in the chemical processing and desorption of accreted volatile material/mantles (e. g. Jones et al., 2013) and can remove electrons, giving the absorbing grain a positive charge (see Ch. 5). Under intense irradiation, grains might sublimate or fragment in a Coulomb explosion as their temperature or charge, respectively, rises. Energetic photons could even directly fragment grains.

When a grain absorbs large amounts of energy, either from a single cosmic ray or hard photon or from a multitude of photons heating it up strongly, if it is not destroyed, its structure and chemical composition might be changed. This can result, for example, in crystallization or amorphization (e. g. Gavilan et al., 2016) or in the creation of inclusions chemically distinct from the bulk material (e. g. Jäger et al., 2016).

The life cycle of a grain ends, finally, when all its material is returned to the gas phase by one of the processes described above or it is incorporated into newly forming stars and planets (astration).

An unknown fraction of grains is presumed to be ejected from the ISM into the circumgalactic medium (CGM) or IGM (e. g. Bianchi & Ferrara, 2005; Imara & Loeb, 2016), resulting in a hiatus of the regular life cycle. The hiatus might be short with grains, or their material if they are destroyed during the process, returning to the ISM relatively quickly (galactic fountains). However, some grains will presumably definitively escape the ISM and be removed from the galactic cycle. In the IGM they are likely to evolve slowly and might survive for very long times.

Describing and understanding all the above processes, which might in fact not represent a complete picture of the life cycle of grains and which take place in environments themselves far from being well understood, is an exceedingly difficult task. To date, no model accounting for most of these processes, let alone all of them, has been put forward (see § 3.5). To remain feasible, studies of cosmic dust have to generally focus on a small subset of properties, phenomena, environments, and scales, such as the mass budget and distribution of dust in a cosmological volume (see § 3.6) or the interaction of a dusty plasma with the ionizing frequency band (see Ch. 4 and 5).

When studying the dust budget, to first order, one can use effective models for processes that transfer material between stars, the gas phase and the solid phase[16].

[16] In reality, of course, these processes depend on environmental factors as well as other dust properties, for example the grain charge (see Ch. 5) and size distribution, which would have to be modelled simultaneously.

Observations indicate that outflows from AGB stars presumably dominate stardust production in the Milky Way today with an uncertain contribution from the remnants of supernovae (e. g. Draine, 2009). However, since SNe occur long before ($\sim 5\,\mathrm{Myr}$ after the onset of star formation) low to intermediate mass stars reach the AGB phase ($\sim 10^8\,\mathrm{yr}$), SNe presumably dominated dust production in the early Universe when the first stars reached the ends of their life cycles. Destruction in shocks, thermal sputtering in shock heated gas and astration are likely the dominant dust sinks, with other mechanisms being more exotic. Destruction rates seem to be much higher than the derived stardust injection rates for the Milky Way, indicating that the growth of grains in the ISM must be efficient (e. g. Ginolfi et al., 2018). This conclusion is supported by the fact that many of the elements strongly depleted in the ISM are, to a significant degree, injected into it in gaseous form (e.g. Si). While the underlying surface chemistry is still debated, and growth seems problematic in the very cold medium of molecular clouds (Ceccarelli et al., 2018), this implies that most of the amorphous silicate material present in the ISM of the MW (and presumably other evolved galaxies) has no stellar origin, but must have formed in some still unidentified phase of the ISM, conducive to efficient growth.

In § 3.6 we will describe a numerical study that accounts for stardust injection from AGB stars and SNe, dust growth and destruction in the ISM as well as astration to model how galaxies build up their dust content over cosmic times.

3.5 Dust models

A full understanding of the life cycle of cosmic dust (§ 3.4) would require a microphysical model based on first principles in the framework of which all grain evolution and interaction processes from formation to destruction can be described. Studying the transfer of ionizing radiation through dust and assessing its interplay with ionized gas, for example, requires detailed knowledge of several grain properties, such as cross sections, charging yields and collisional coefficients. No *ab initio* model has been put forward to date and it seems unlikely that this will happen in the foreseeable future as our knowledge of the conditions in which grains exist and the reactions taking place on and within them is still very limited. Consequently, other approaches have to be taken.

One route to arrive at a physical grain model is, first, to propose a chemical composition and a distribution of grain shapes and structures. Second, to compute observable properties from this proposition. Third, to adjust the proposition's free parameters to meet observational constraints. Naturally, this is an iterative process. The most stringent constraints are given by interstellar depletion (dictating the available grain building material), extinction, polarization and dust emission (§ 3.1), however, they are generally insufficient to allow for unique solutions.

This "classical" approach was pioneered shortly after the postulation of the existence of interstellar dust (e. g. Schoenberg & Jung, 1934). In subsequent decades, many different successful models were developed (e.g. Mathis et al. 1977; Greenberg 1986; Li & Greenberg 1997; Li & Draine 2001, hereafter LD01; WD01a; Clayton et al. 2003; Zubko et al. 2004; Draine & Li 2007; Mulas et al. 2013; Siebenmorgen et al. 2014). Two classes of models, accounting for the observational evidence in favour of cosmic dust containing large amounts of carbonaceous material as well as silicates, have been particularly well developed. The first is the family of Silicate-Graphite models (e. g. Mathis et al., 1977) and its later extension to Silicate-Graphite-PAH models (e. g. LD01), which propose two co-existing but separate populations of carbonaceous and silicate grains. The second is the family of core-mantle models, which, given the turbulent conditions prevalent in the ISM, argue in favour of mixing of the two main dust components and propose grains consisting of silicate cores with mantles of carbonaceous material (e. g. Greenberg, 1986).

While the shapes and structures of real cosmic dust grains presumably vary considerably (§ 3.1), models generally assume few and simple shapes to reduce complexity and, given missing constraints, avoid arbitrary choices. If the polarization of light is not accounted for, spherical shapes, possibly with layers or pores/inclusions are frequently chosen (e. g. Mulas et al., 2013). Otherwise, cylindrical or spheroidal shapes are a prominent choice (e. g. Li & Greenberg 1997; Hensley & Draine 2020, in prep.). See also Voshchinnikov (2012) for a review. Simple shapes/structures may not be as unreasonable a choice as one might naively expect, at least as far as interactions of electromagnetic radiation with an ensemble of grains are concerned. Cosmic grains are likely to rotate, such that even when they are aligned on large scales, radiation will "see" an effective grain shape that is much simpler than the reality of a myriad of complex and different grains. However, methods to compute the optical properties of arbitrary grains have been developed (e. g. Purcell & Pennypacker, 1973; Draine, 1988) and used to explore the effects of complex grain shapes, such as aggregates of spheres or spheroids (e. g. Ysard et al., 2018). These studies indicate that effective models are not able to reproduce all associated effects, which might be particularly pertinent to dust in protoplanetary disks (e. g. Tazaki et al., 2019; Kirchschlager & Bertrang, 2020). Naturally, grain interaction processes apart from those with the radiation field also depend on shape and structure (e.g. Ma et al., 2013), however, a discussion of this is beyond the scope of the present work.

As discussed in § 3.1 and § 3.3, observational constraints on dust and, by implication, the grains themselves are not everywhere the same. Consequently, a set of observations corresponding to a certain environment has to be chosen to tune a proposed model. Since usually simple grain geometries are assumed and relatively few materials considered in the chemical composition, the size distribution of grains is generally what gives an initial proposition most of its flexibility to reproduce different sets of observations (e. g. WD01a; Clayton et al. 2003; see Mulas et al. 2013 for an

example of a more complex assumption on chemical composition). Naturally, this can provide valuable insights on differences in grain populations, however, it provides little motivation as to the origin of the differences. Furthermore, it means that the predictive power of "classical" models is limited. A complimentary and more recent dust modelling approach, which tries to improve on these aspects, is to develop a framework that provides prescriptions for how grains evolve in different environments based on a set of assumptions about their chemical composition, for example by building upon the idea of core-mantle grains (e. g. Jones et al., 2013, 2017; Cecchi-Pestellini et al., 2014).

In the context of this work we are mainly interested in developing numerical schemes to investigate the interaction of dust with hydrogen ionizing radiation. Since so much remains unknown about cosmic dust, our strategy is to adopt the well established and comparatively simple Silicate-Graphite-PAH model to compute any concrete values that are required, while keeping numerical implementations model-independent (Ch. 4 and Ch. 5). We defer the exploration of other models to future work. We will furthermore neglect many aspects of the evolution of dust grains, only briefly exploring the processing of PAHs in H II regions (§ 3.5.3, § 4.2.1.1 and 4.2.2) and studying the charging of grains in more detail (Ch. 5). Note that the above does not apply to the complementary work presented in § 3.6, where a different dust model is used and the formation, growth and destruction of dust are studied.

This section is organised as follows. We first present the dust properties we require in § 3.5.1 and then introduce the Silicate-Graphite-PAH model in § 3.5.2. § 3.5.3, finally, discusses the contribution of PAHs to the dust optical depth. The Silicate-Graphite-PAH model offers a prescription for grain charging, which we will use for our implementation in Ch. 5. We decided to also present the prescription there instead of in this section, since it is pertinent to the understanding of our implementation choices.

3.5.1 Optical properties

Photon absorption and scattering[17] by a dust grain are characterised by its frequency-dependent absorption and scattering cross sections, $\sigma_\mathrm{a}(\nu)$ and $\sigma_\mathrm{s}(\nu)$ respectively. $\sigma_\mathrm{e} = \sigma_\mathrm{a} + \sigma_\mathrm{s}$ is referred to as the extinction cross section, and the relative importance of scattering against extinction is quantified by the albedo $\widetilde{\omega} = \sigma_\mathrm{s}/\sigma_\mathrm{e}$. The scattering asymmetry parameter $\langle \cos\theta \rangle$, where θ is the scattering angle and the brackets indicate averaging over scattering events, complements the information about the capability of dust grains to deviate incoming light. We customarily refer to the above-mentioned quantities as the *optical properties* of dust (see Henning & Mutschke

[17] Hereafter, scattering in the context of dust-radiation interactions will always refer to elastic scattering. To our knowledge, inelastic scattering by cosmic dust grains has never been investigated in detail as it is likely too weak to have an effect appreciable outside of laboratory settings.

2010 for a recent review or Bohren & Huffman 1983 for an extensive treatment). They generally depend on a series of grain properties (e.g. chemical composition, solid-state structure, morphology) and environment-dependent conditions (e.g. dust temperature, charge state) and can be determined both theoretically (e.g. Draine 2003b,c) and experimentally (e.g. Henning & Mutschke 2010 or see the *Amsterdam-Granada light scattering database*[18]).

Typically, the optical properties of cosmic dust can observationally only be constrained at photon energies $h\nu < 13.6\,\mathrm{eV}$ (e.g. Cardelli et al. 1989), where the gas component of the ISM does not dominate absorption, and at energies $> 10^2\,\mathrm{eV}$, by means of X-ray scattering haloes (e.g. Smith & Dwek, 1998; Draine & Tan, 2003). In the ionizing UV band 13.6 eV to 200 eV, which is of central importance to the ionization of the hydrogen and helium gas components, one generally has to fully rely on model predictions.

3.5.2 The Silicate-Graphite-PAH model

We adopt optical properties provided by the Silicate-Graphite-PAH model (specifically WD01a; LD01). In this subsection we summarize the main assumptions of the model and present some of its results, as they are necessary to understand the implementation in CRASH(Ch. 4). We refer the interested reader to the original papers for more details.

WD01a and LD01 assume a dust composition consisting of two chemically distinct grain populations: one based on silicate and one based on carbon. For each population, they assume a grain size distribution described by a modified power-law with a smooth cut-off at large sizes ($a \sim 1\,\mu\mathrm{m}$ to $10\,\mu\mathrm{m}$) and a variable slope towards the small-size cut-off at 3.5 Å (see Eqs. (4)–(6) in WD01a and App. A). Silicate grains and large carbon grains (with an effective grain radius $a \gtrsim 100\,\text{Å}$; see Weingartner & Draine 2001b, § 2.1) are assumed to be spherical and composed of olivine and graphite respectively; their optical properties are computed in the framework of Mie theory (e.g. Bohren & Huffman 1983). For the carbonaceous population two log-normal distributions peaking at 3.5 Å and 30 Å are added to provide additional small grains. Small carbon grains ($a \lesssim 20\,\text{Å}$) are given the optical properties of PAHs[19], and transitional properties are used for intermediate size carbon grains (see also Eq. (A.1)). WD01a and LD01 tune their size distributions in order for their dust model to reproduce the observed dust extinction and IR emission of the diffuse

[18] `http://www.iaa.es/scattering`

[19] The optical properties used are guided by observations and laboratory measurements and therefore the actual geometry of the PAHs is irrelevant for this purpose. When modelling aspects where this is not true, PAHs are assumed to be spherical with radius a (cf. Weingartner & Draine, 2001b, Eq. (1)). In the general literature, small PAHs are usually assumed to be planar while larger ones are assumed to be spherical (e.g. Hoang et al., 2010).

Milky Way ISM. The Fitzpatrick (1999) R_V-parametrization of the extinction curve with $R_V = 3.1$ is chosen to represent the observed extinction. The model can also reproduce extinction along many other lines of sight through the ISM of the Milky Way and also of the Magellanic Clouds, where typical extinction differs from that of our galaxy (see § 3.2 of WD01a).

A later version of the model (Draine, 2003a,b,c) provides corrected dust abundances as well as updated material constants. The optical properties of the dust mixture are computed in a wide energy range ($\sim 10^{-4}$ eV to 10^4 eV), using anomalous diffraction theory (van de Hulst, 1957) instead of Mie theory at X-ray energies. These new data[20] are plotted as functions of photon energy in Fig. 3.6 for $R_V = 3.1,\ 4.0$ and 5.5. More specifically, we adopt the WD01a case A size distributions with carbon abundance per H atom in the log-normal populations $b_\mathrm{C} = 60$ ppm and total carbon dust abundance corrected by a factor 0.93 for $R_V = 3.1$, with $b_\mathrm{C} = 40$ ppm corrected by 1.18 for $R_V = 4.0$, and with $b_\mathrm{C} = 30$ ppm corrected by 1.42 for $R_V = 5.5$ (see WD01a and Draine 2003a). While the three lines differ, their qualitative behaviour is very similar, and thus we will restrict ourselves to discussing the $R_V = 3.1$ case. We also restrict the discussion to H-ionizing energies ($h\nu \geq 13.6$ eV) as CRASH performs RT only in this photon energy range. Note, additionally, that more recent cross sections and material constants, taking into account new observations and laboratory data, have been published for the carbonaceous model-grains (Draine & Li, 2007; Draine, 2016). These latest updates are not taken into account here, since the older optical data plotted in Fig. 3.6 are readily available and easily sufficient for the purposes of this work.

The albedo (top panel) starts out at a value of ~ 0.2 around 13.6 eV and remains below ~ 0.5 in the entire UV regime (13.6 eV $< h\nu \lesssim 200$ eV), i.e. dust absorption dominates scattering at these energies. Entering the soft X-ray domain (0.2 keV $< h\nu <$ 3 keV), it rises approximately linearly with $\log(h\nu)$ to ~ 0.6 at 300 eV. From this point onwards up to 3 keV it remains roughly constant on average, so that at these energies more than 50 % of the photon-dust interactions are scattering events. The scattering asymmetry parameter (second panel) rises quickly from ≈ 0.7 at 13.6 eV to unity at 100 eV, i.e. in our energy regime the dust grains are mostly to purely forward scattering.

As CRASH currently neglects scattering in its ray tracing algorithm[21], we investigate the impact of this approximation using $(1 - \langle\cos\theta\rangle)\,\widetilde{\omega}$ (third panel). This parameter measures how strongly photons are deviated from their initial direction of propagation

[20] Available online at `http://www.astro.princeton.edu/~draine/dust/dustmix.html`.

[21] The implementation of radiation scattering in a code accounting for gas ionization and temperature as well as dust as function of time, would severely increase the computational requirements of a single run or even impede reionization simulations. Sophisticated implementations of radiation scattering on dust grains exist (e.g. Camps & Baes 2015; Gordon et al. 2017) but they are generally limited to time independent algorithms and do not account for the gas component.

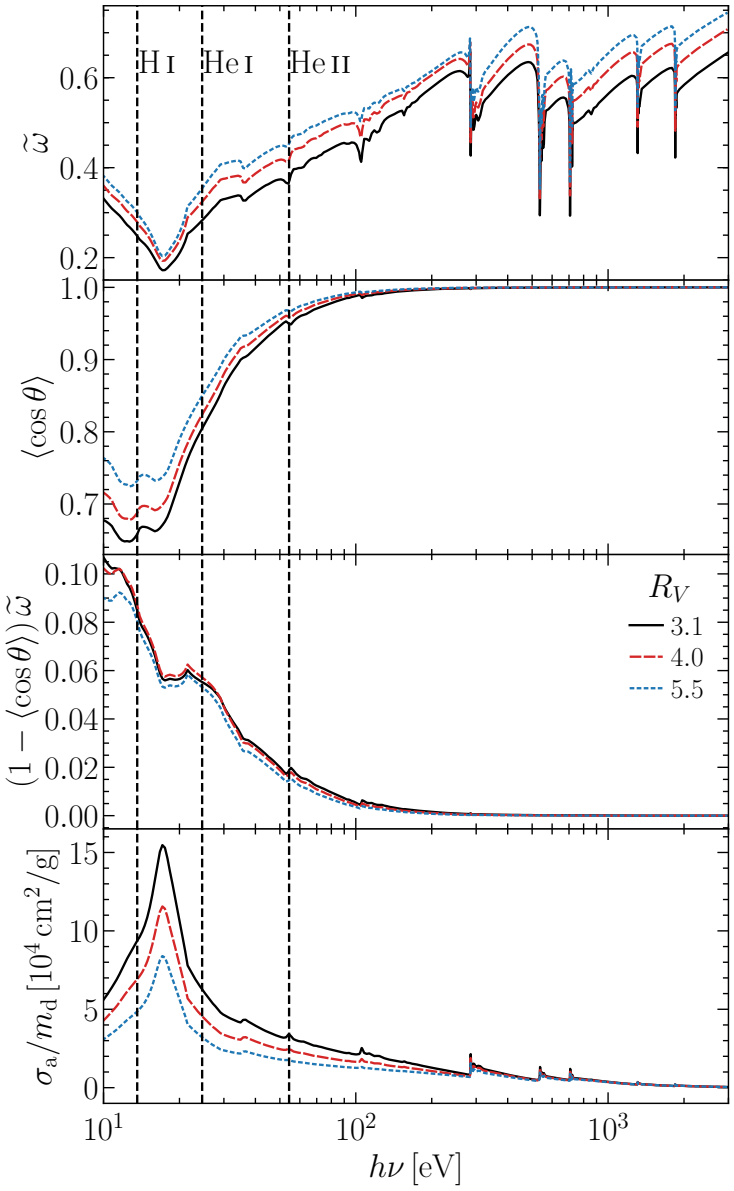

Figure 3.6: Fig. 1 of GCG19. From top to bottom the panels show as functions of photon energy: the albedo $\widetilde{\omega}$, the scattering asymmetry parameter $\langle\cos\theta\rangle$, $(1-\langle\cos\theta\rangle)\,\widetilde{\omega}$ and the absorption cross section per dust mass, σ_a/m_d. The different lines correspond to dust mixtures that reproduce extinction along Milky Way lines of sight with R_V values of 3.1 (solid black), 4.0 (dashed red) and 5.5 (dotted blue) (WD01a; LD01; Draine 2003a,b,c). The ionization potentials of hydrogen and helium are marked with vertical dashed lines. See text for more details.

upon interacting with a grain. If it is zero, no deviation takes place and scattering can safely be neglected. In the range 13.6 eV–3 keV, it remains below 0.1, indicating that neglecting scattering is an acceptable approximation in our ray-tracing scheme, at least with the present dust model and in applications to diffuse gas, as those of our interest. This scheme is, on the other hand, not appropriate to model protoplanetary discs, for instance, and using a different dust model might invalidate our argument. We plan to address scattering in a future release of CRASH after implementing other dust processes that directly impact grain charging and gas ionization (Ch. 5).

The bottom panel of Fig. 3.6, finally, shows the absorption cross section per dust mass. It peaks at ~ 17 eV (i.e. between the H I and He I ionization potentials) and progressively decreases with increasing energy, showing some structure owed to the inner shells of grain constituents.

Since the main goal of our implementation is to investigate the RT through dust and gas (H, He), it is important to compare the relevant cross sections at fixed photon energy. Fig. 3.7 shows the dust absorption cross section (dash-dotted orange) together with the ionization cross sections of neutral hydrogen (solid black) and neutral helium (dashed red) (Verner et al., 1996); these are the primary species competing with dust grains in absorbing ionizing photons. The cross sections are normalized per H nucleus. We assume protosolar gas composition (Draine 2011a, Table 1.4; see also Asplund et al. 2009) and a GDR of 124, as suggested by WD01a and LD01 for the diffuse ISM of our galaxy. With the above assumptions, it is evident that in a neutral gas-dust mixture, dust will only be relevant to absorption at energies of several hundred eV, but note that the GDR can vary strongly (e.g. § 3.1 Mancini et al. 2016; Graziani et al. 2020). Unlike gas (which becomes ionized and thus transparent), however, the opacity of dust in photo-ionized regions does not change significantly in time unless the UV field is strong enough to destroy the grains[22]. Therefore dust can provide time-persistent opacity over a wide photon energy range and might be an important contributor to absorption also at lower energies. For example, a typical stellar radiation field can easily ionize both H I and He I so that the dust grains will, after a certain point in time, compete only with singly ionized helium (dotted blue) while continuously absorbing energy from the UV field in 13.6 eV to 54.4 eV. In reality, however, the situation is much more complex because (i) the presence of atomic metals in the gas mixture (for a discussion including abundance constraints on dust models see Draine, 2003a, 2011a) alters the total optical depth and (ii) the ionization fractions and recombination rates of each species are complex functions of local conditions. It is thus not possible to make a general quantitative statement on the importance of dust absorption in ionized gas

[22] It should be noted that this is not strictly correct. The charge of a grain, e. g., will have an effect on its optical properties (cf. Ch. 5). Also note that grain destruction is not yet implemented in CRASH (see § 4.1) and that different grain types (both size and composition) are expected to behave very differently when exposed to radiation (cf. Ch. 5).

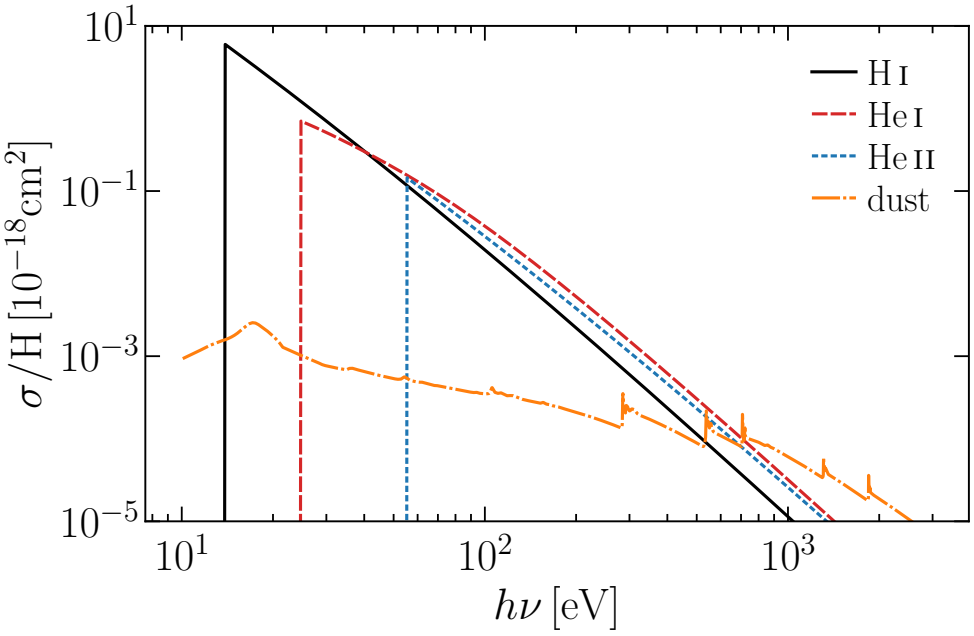

Figure 3.7: Fig. 2 of GCG19. Ionization cross section per hydrogen nucleus as a function of energy for neutral hydrogen (solid black line), neutral helium (dashed red) and singly ionized helium (dotted blue) (Verner et al., 1996). Also shown is the absorption cross section of dust per hydrogen nucleus for $R_V = 3.1$ (dash-dotted orange). Protosolar gas composition and a GDR of 124 were assumed. See text for details.

without detailed numerical modelling. We defer a more detailed discussion and the inclusion of gas phase metals to future investigations.

Our choice of the Silicate-Graphite-PAH model for the purposes of this work is owed to the fact that it is widely used, easily accessible and comparatively simple. On the other hand, this model is primarily designed to explain the various spectral features of dust extinction curves and dust IR emission on an observation by observation basis, i.e. it offers no straightforward formalism to model the evolution of a given dust population. For example, the PAH contribution to the total absorption cross section can not easily be isolated. As PAHs are susceptible to photo-dissociation, it is important to quantify the error introduced by assuming their continuous presence during the RT process. This point is addressed in the following section.

3.5.3 Contribution of PAHs to the dust optical depth

Dust mixtures are known to be sensitive to both UV radiation and gas phase transitions from neutral to ionized. The PAH component, in particular, is susceptible to restructuring and destruction via photo-dissociation (e.g. Voit, 1992; Jochims et al., 1994; Le Page et al., 2001) and collisions with free electrons and ions present in a hot, ionized gas (e.g. Micelotta et al., 2010a,b; Bocchio et al., 2012). The efficiency of the above processes, however, as well as the change in PAH composition induced by them, are not fully understood and are subject of thorough investigations (e.g. Zhen et al., 2016). Observations, nevertheless, suggest PAHs to be systematically depleted in galaxies hosting an active galactic nucleus (Roche et al., 1991; Smith et al., 2007; Jensen et al., 2017) or in H II regions (e.g. Kassis et al. 2006; Whelan et al. 2013; Stephens et al. 2014; Salgado et al. 2016; Chastenet et al. 2019), so that they seem to provide conditions conducive to PAH destruction (but see Compiègne et al., 2007).

While many processes of PAH evolution have been implemented for circumstellar disks (Visser et al., 2007; Siebenmorgen & Krügel, 2010) or to model specific features of galactic H II regions (Giard et al., 1994), a consistent time dependent RT approach including dust mixtures and gas is still missing. It is, in fact, not clear how current models for dust mixtures (see section above) should be modified to derive cross sections excluding the photo-dissociated PAH component.

In this work we perform a first step in this direction by recomputing the cross section of a dust mixture without the PAH component in the framework of the Silicate-Graphite-PAH model. The result will be used in § 4.2.1.1 to asses the impact of the PAHs on the size of ideal dusty H II regions and in § 4.2.2 with a more complex dust distribution and source configuration.

For an immediate comparison with the discussion of the previous section, here we discuss the resulting absorption cross sections, while the details of the modelling are deferred to App. A.

Fig. 3.8 shows the dust absorption cross sections (per mass of full dust mixture) as a function of photon energy. Before introducing any changes in the dust composition, we note that the original Silicate-Graphite-PAH model with $R_V = 3.1$ (solid black line) and our own result when PAHs are included (dashed red line) are in good agreement, with a maximum difference of 9 % at 21.5 eV[23].

A significant reduction of the cross section by a factor of two (orange line, cut model) or three (blue and green lines for split and $b_C = 0.0$ ppm models, respectively) relative to the original data is found at its peak (~ 17 eV) and it remains considerable

[23] The systematic offset between cross sections is likely due to the fact that we adopted a slightly different version of the Wiscombe-Mie code (Warren J. Wiscombe, Mie Scattering Calculations: Advances in Technique and Fast, Vector-Speed Computer Codes, NCAR/TN-140+STR, NCAR TECHNICAL NOTE Jun); see also App. A and App. C.

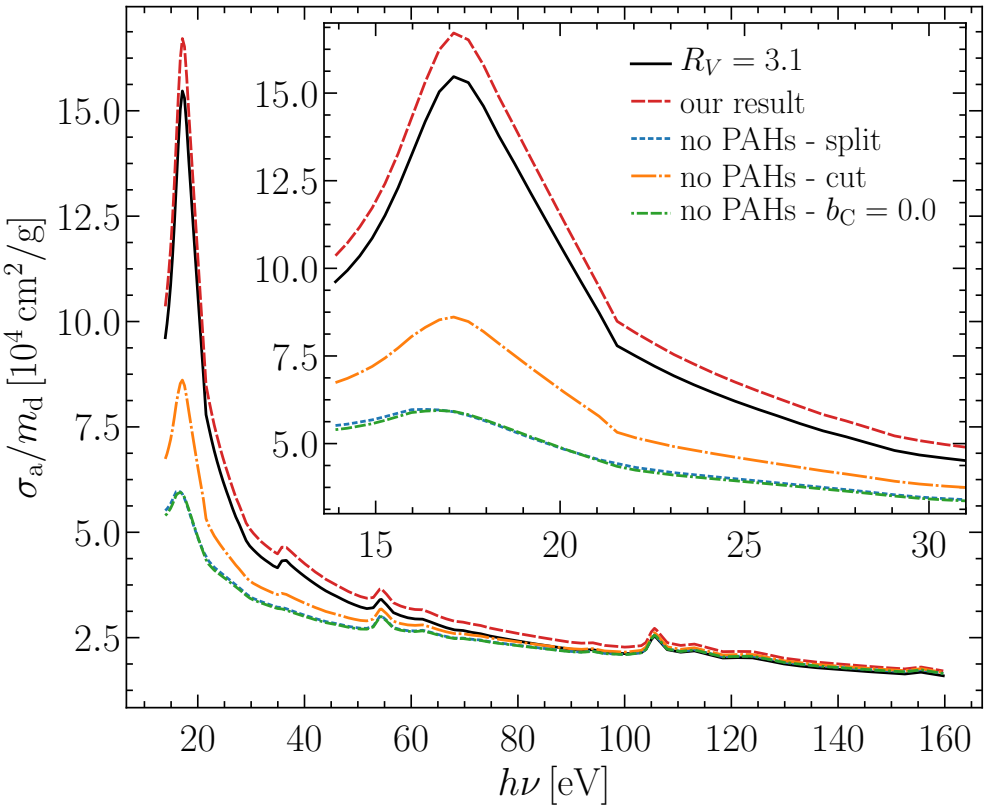

Figure 3.8: Fig. 3 of GCG19. Dust absorption cross section per mass as a function of photon energy for the Silicate-Graphite-PAH model ($R_V = 3.1$) as in Fig. 3.6 (solid black) and recomputed as detailed in App. A (solid red). Cross sections obtained excluding the PAH component are shown for three different assumptions in removing PAHs: the dotted blue line is the result of splitting the carbon grain size distribution into a graphite and a PAH component, the dash-dotted orange line is obtained by cutting the size distribution at a grain radius corresponding to 1000 C atoms, and finally for the dash-dash-dotted green line we set $b_C = 0.0$ ppm, thus removing the two log-normal grain size distributions. For details on these three approaches see App. A. A zoom-in view of the curve in the most relevant energy range 13.6 eV to 30 eV is provided by the inset.

($\sim 20\,\%$) in the energy range up to 30 eV. The differences progressively decrease to $5\,\%$ at ~ 60 eV, and remain at or below this value at higher frequencies because all size distributions converge to the original model, i.e. the PAH component does not contribute significantly anymore to the mixture cross section.

In summary, the PAH component provides an important contribution in absorption in the photon energy range 13.6 eV to 60 eV, while its presence is negligible in the remaining part of the spectrum. In § 4.2 we investigate the impact of this on gas ionization and temperature, using the $b_{\mathrm{C}} = 0.0$ ppm approach to obtain an upper limit on the impact.

3.6 The assembly of dusty high redshift galaxies

The detection of dusty galaxies at high redshifts (see § 3.3) has increased interest in the question of how early chemical enrichment and dust formation take place. Particularly the latter point has frequently been neglected in models in the past. Dust can impact many aspects of the evolution of a galaxy, while itself constantly evolving in its ISM (§ 3.4). In cosmological models, most of these processes can not be accounted for in detail as they take place on unresolved scales. Nevertheless, such studies can shed light on the colours of galaxy populations, on the observability of star formation, and on reionization (see Ch. 6). Comparisons to already existing low and high redshift observations can aid in their interpretation and, conversely, in refining our understanding of the build up of the cosmic dust budget. Finally, predictions of these studies will have to be vetted against future observations (e. g. ALMA[24], JWST[25], ELT[26]), which will certainly include many more high redshift objects than we know of today.

Semi-numerical cosmological models of galaxy formation allow for comparatively cost-efficient dust mass budget computations and have been shown to be useful in the interpretation of observations (e. g. Mancini et al., 2015, 2016). However, they necessarily lack detail compared to fully numerical models including an on-the-fly treatment of dust. Such models are challenging to implement and have only recently become available (e. g. Bekki, 2015; Aoyama et al., 2018; Gjergo et al., 2018; McKinnon et al., 2018; Li et al., 2019).

In this section, we will briefly summarize Graziani et al. (2020), a numerical study focussing on the dust content of galaxies at $z \geq 4$. In § 3.6.1 we describe the numerical model and in § 3.6.2 we discuss selected results. The interested reader is referred to the original publication for more details.

[24] `https://www.almaobservatory.org`
[25] `https://www.jwst.nasa.gov`
[26] `https://www.eso.org/sci/facilities/eelt`

3.6.1 A numerical model of galaxy formation including dust

In Graziani et al. (2020), the SPH galaxy formation code `Gadget` (Springel, 2005), including a multitude of subsequent extensions, was used as a basis to develop `dustyGadget`, which additionally accounts for the formation, growth and destruction of dust grains.

`dustyGadget` builds upon the chemical network of its predecessors, ensuring that ISM enrichment by atomic metals is consistent with dust enrichment. Four grain compositions, with average stoichiometries as indicated in brackets, are taken into account: carbon grains (C), silicates ($MgSiO_3$), alumina (Al_2O_3) and iron grains (Fe). All grains are assumed to be spherical with a radius of $\sim 0.1\,\mu m$.

In each SPH particle, the mass of dust of each composition is kept track of for the entire duration of a simulation. Gas and dust are assumed to be fully dynamically coupled (cf. § 3.4), i. e. no relative movement between the two components is assumed. This is also true for galactic winds, ejecting gas and dust from star-forming regions, possibly even into the IGM. The two phase ISM model introduced by Springel & Hernquist (2003) is adopted, i. e. each SPH particle is assumed to contain a diffuse/hot and a dense/cold phase, which are unresolved and the evolution of which is described using an effective model. As the gas particle evolves, cooling and heating will transfer material between the phases. Star formation will sequester gas and dust from the cold phase into star particles and dying stars will inject gas and dust from star particles into the hot phase.

Dust production by AGB stars, core-collapse SNe (from Pop II/I stars) and pair-instability SNe (from Pop III stars) is considered. In cosmological simulations, the spatial and temporal scales at which the production takes place can not be resolved, so that effective dust yields are adopted. This applies in particular to SNe and the associated reverse shock (see § 3.4). As stars in a star particle reach the ends of their lives, the metals and dust they eject are distributed across neighbouring gas particles, whereby the dust follows the distribution prescription for the atomic metals, in keeping with the assumption of full dynamical coupling.

SNe, naturally, do not only produce stardust but also destroy interstellar dust. In the model, grains in the hot phase are subjected to this process. Since cosmological simulations, again, do not resolve the shocks themselves, an effective model based on the number of SNe exploding in each gas particle at a given timestep has to be adopted. SN explosions are assumed to affect only single gas particles, which is a good approximation for a cosmological simulation, while it does not apply at higher resolutions (e. g. Aoyama et al., 2017).

Grains in the hot phase of a gas particle are furthermore subjected to sputtering by hydrogen and helium nuclei. The return of mass from the solid to the gas phase is computed from an estimate of the sputtering timescale of a spherical 0.1 µm grain

based on temperature and density of the hot phase. Identical efficiencies are used for all grain compositions, which has been shown to be a valid approximation.

In the cold phase, finally, grains grow by accreting material from the gas. Since the cold phase is a subgrid phenomenon and not resolved, this is treated only approximately. The accretion timescale, again assuming a spherical 0.1 µm grain, can be estimated from the cold phase density, temperature and gas metallicity. Density and metallicity are known, but the two phase ISM model does not compute the cold phase temperature, instead assuming it to be constant. A value of 50 K is chosen with results being relatively robust to changes in this parameter.

Note that, at the moment, no other properties of dust and processes involved in its complex evolution (cf. § 3.4) have been accounted for, due to the high modelling complexity and computational cost. Future work will improve on this shortcoming.

3.6.2 Results

In Graziani et al. (2020) results from a cosmological galaxy formation simulation are presented. The simulation was performed on a periodic $30\,h^{-1}$cMpc box using the WMAP7 (Komatsu et al., 2011) ΛCDM cosmology. The box is evolved from $z = 100$ down to $z = 4$ with a resolution of $9 \times 10^6\,h^{-1}\mathrm{M}_\odot$ and $6 \times 10^7\,h^{-1}\mathrm{M}_\odot$ in gas and dark matter, respectively. The formation of Pop III stars is explicitly accounted for, i. e. chemical enrichment is followed from the beginning. We present only selected results here while more details and discussions can be found in the original publication.

Fig. 3.9 shows the total dust mass as a function of the total stellar mass for all galaxies with stellar mass $> 10^{7.5}\,\mathrm{M}_\odot$ formed in different redshift bins as indicated in the individual panels. The blue points correspond to the simulation results, and the yellow points show the dust masses predicted by the Mancini et al. (2015) model applied to the same galaxies. The various symbols show available observations and upper limits (indicated by downward arrows) and their respective uncertainties (see Graziani et al. 2020, Table 2). Note that currently only relatively massive objects are observationally available. The different lines show results from independent semi-numerical studies and will not be discussed here.

The dust budget at the low mass end is dominated by stardust production. Dust mass grows approximately linearly with stellar mass here as stardust formation is balanced by destruction in SN shocks. More massive galaxies that are assembled as time progresses, provide larger reservoirs of cold gas in which dust grains grow efficiently. This leads to a rapid growth in dust mass as a function of stellar mass until saturation is reached when growth is limited by the available gas phase metals, resulting in dust mass again growing linearly with stellar mass, which is a good proxy for metallicity.

Already at $z > 6$ a clear transition away from stardust domination of the dust budget is found. This indicates that grain growth is efficient even with weak chemical

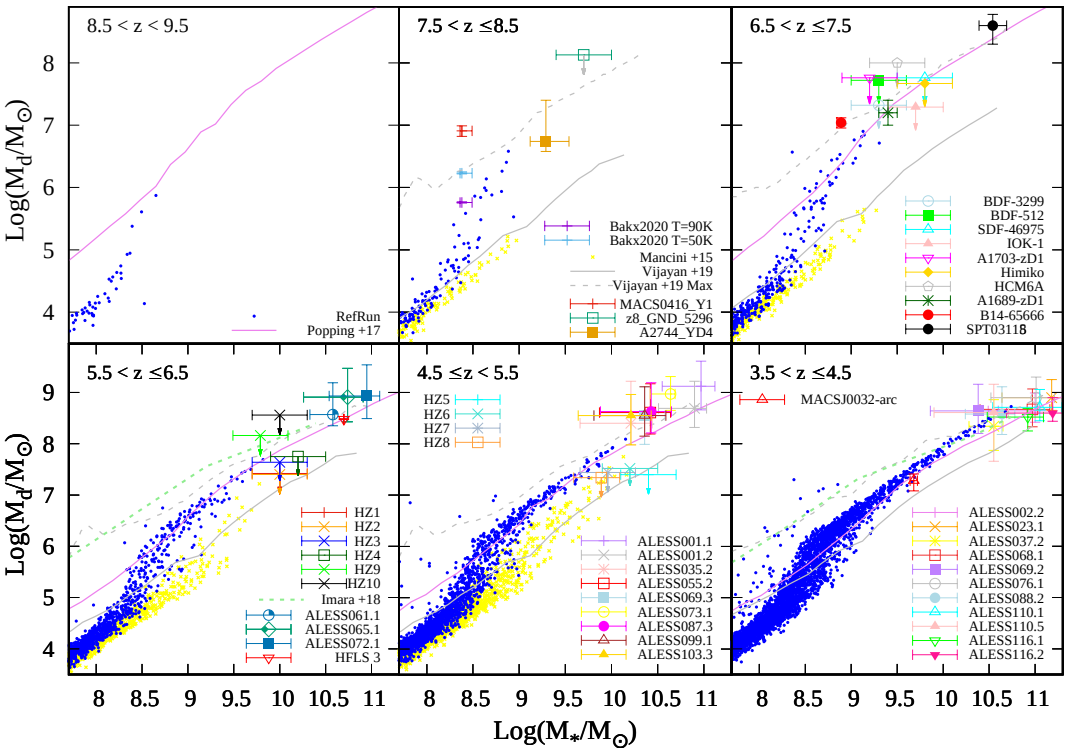

Figure 3.9: Fig. 3 of Graziani et al. (2020). Dust mass as a function of stellar mass for all galaxies with stellar mass $> 10^{7.5}\,\mathrm{M}_\odot$ found in a galaxy formation simulation at different redshifts as indicated in the panels (blue points). Also shown are dust mass predictions using Mancini et al. (2015) on the same objects (yellow points). The various symbols correspond to available observations and upper limits with error bars (see Graziani et al. 2020, Table 2). The lines show independent model results not discussed here. See text and original publication for more details.

enrichment, provided the right conditions are available. This conclusion is supported by the fact that the Mancini et al. (2015) model, in which the density dependence of grain growth efficiency is neglected, consistently predicts lower dust masses.

Overall, the agreement with observations is good. Although, particularly at the higher redshifts, as a result of the small simulation volume and moderate resolution, no or few galaxies with enough stellar mass for direct comparison are found in the box, the trends are encouraging. Note that the efficient grain growth, enabled in the simulation by accounting for its density dependence, is necessary to reproduce observational trends in the higher redshift bins. In the lowest redshift bin, the agreement is excellent, also with MACSJ0032-arc, a relatively small object with normal star formation activity ($\sim 50\,\mathrm{M}_\odot\mathrm{yr}^{-1}$).

Note that dust masses derived from observations are significantly affected by the adopted dust temperature values and emissivity properties. This is particularly problematic when only few or even a single wavelength can be observed, providing very weak constraints. This is illustrated in the $z \sim 7$ panel, where the $z = 8.3$ object MACS0416_Y1 as originally reported (Tamura et al., 2019) lies far above the dust mass values predicted from the simulation. Bakx et al. (2020) recently revised this value having found evidence for a particularly high dust temperature, resulting in a much better agreement with our simulation results.

In Fig. 3.10 we show a map of the dust density distribution around the central galaxy of the most massive halo contained in the simulation box at $z \approx 4$ (dark matter mass $\approx 1.2 \times 10^{12}\,\mathrm{M}_\odot$, virial radius $\approx 250\,\mathrm{kpc}$). The overplotted contour lines show the logarithm of $\mathcal{D}$. The dust distribution is strongly inhomogeneous with $\mathcal{D}$ values of $\sim 10^{-2}$ (i. e. GDR 100 corresponding to the MW average) reached in the centre of the galaxy and regions in the CGM being almost completely devoid of dust. Note that this map naturally lacks much small scale detail (an extreme comparison would be Fig. 3.5), however, future similar versions with somewhat increased resolution could, in combination with an RT treatment, provide useful comparisons for high-redshift observations.

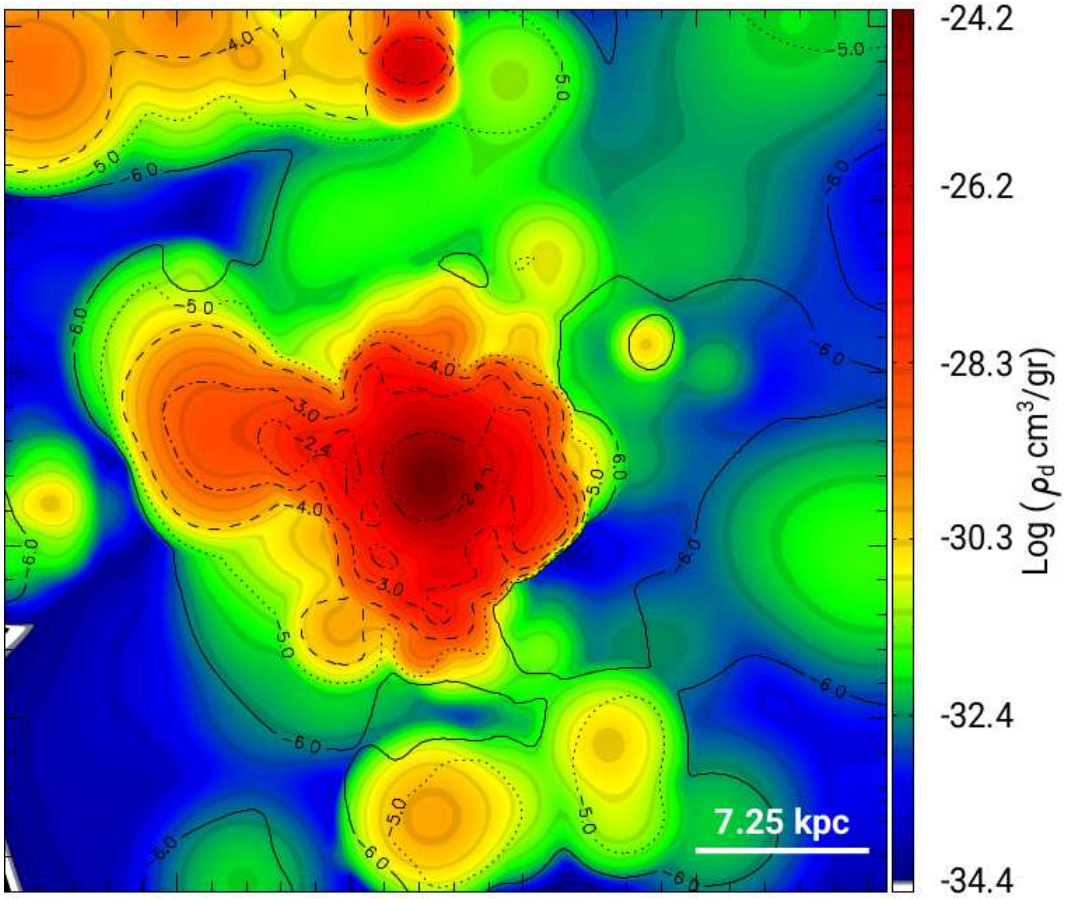

Figure 3.10: Fig. 6 b) of Graziani et al. (2020). The dust mass density distribution around a galaxy at $z \approx 4$ extracted from our simulation. The contour lines show $\log(\mathcal{D})$. See text for details.

Chapter 4

Radiative transfer through gas and dust: absorption

3D radiative transfer simulations are among the most powerful tools available to theorists to investigate many astrophysical phenomena. Very capable codes have been written and, in some cases, published for example for pure dust RT (e.g. Steinacker et al., 2013; Gordon et al., 2017), line RT (e.g. Behrens et al., 2019) and transfer of the ionizing continuum ($h\nu > 13.6\,\mathrm{eV}$, which is recently often coupled to hydrodynamics; see § 2.6) through gas on (sub)galactic scales (e.g. Bisbas et al., 2015a) as well as on cosmological scales (e.g. Iliev et al., 2006, 2009). While separate treatments are useful in the explanation of many phenomena, ultimately, to resemble Nature as closely as possible, the different radiation bands as well as gas (atomic and molecular) and dust physics should be coupled in combined simulations. This, naturally, is very challenging, such that in 3D RT either gas or dust are frequently neglected[1].

As explained in Ch. 3, dust is often present where ionizing photons are produced and it will compete with the gas for their absorption (§ 3.5.2), making the transfer of ionizing radiation through gas and dust an interesting problem with many implications. We are aware of the following 3D ionizing continuum RT codes featuring dust physics models of varying complexity and thus principally capable of investigating it: MOCASSIN (Ercolano et al., 2005), the code used in Wood et al. (2010), ART[2] (Yajima et al., 2012), SEDNA (Bisbas et al., 2015a, § 3.9) and TORUS-3DPDR (Bisbas et al., 2015b). Here we perform our first step towards combining gas and dust RT in CRASH (§ 2.4), which is set apart by a unique combination of features being a time dependent cosmological code including hydrogen, helium and X-ray (§ 2.5) physics, by implementing dust absorption. In Ch. 5, we present a first version of an extension to our implementation which also accounts for the charging of grains.

This chapter is organised as follows: we describe our implementation in § 4.1. In § 4.2, we apply our newly extended RT code to model the impact of the ionizing

[1] The 1D spectral synthesis code CLOUDY (Ferland et al., 2017) likely features the most complete radiation physics model of all codes used in astrophysics, accounting for atoms, molecules and grains. Specialized 1D photon dominated region codes (e.g. Röllig et al., 2007) and 2D codes used in the modelling of protoplanetary discs (e.g Woitke et al., 2009; Bruderer et al., 2014) also generally include some gas and dust physics.

radiation emitted by a single young O–type star in the local Universe on a dust-polluted medium. In this context we also evaluate the contribution of PAHs to dust absorption at ionizing photon energies. We furthermore investigate the effect of dust in the early Universe on small scale reionization by artificially polluting a small cosmic web. This is done in preparation of future applications we envision for our code, one of which is studying the impact of dust production on the evolution and detectability of high redshift objects and their surroundings. We also test our implementation against the analytic solution of a highly idealized configuration (App. B).

4.1 Implementation in CRASH

Here we describe the modifications which enable CRASH (§ 2.4) to account for dust absorption in RT simulations. We start discussing how we abstracted this problem to achieve an implementation that is extendable and independent of any specific dust model.

The most general way to obtain the necessary data from a dust model is by interpolation of pre-computed tables, which is therefore our method of choice. Any chosen dust model might provide properties for a predefined dust mix, or it might provide properties for several components (e.g. grains of a specific size and composition) which can be combined to form a grain population; it is therefore clear that a general dust RT code should support the concept of a dust species, i.e. a set of properties representing one component of a grain population[2]. Furthermore, in realistic applications dust will not be distributed homogeneously in space (§ 3.2, § 3.6), and its properties (composition, ionization, grain size, temperature, etc.) may also be functions of location and time. An RT code accounting for dust, therefore, needs to be able to track not only the dust abundance but also its properties, possibly per species, at each point of the discretised domain during the entire RT process. This has the additional advantage that radiation effects on dust grains (such as heating, ionization, metamorphism and destruction) can be accounted for in detail, and their coupling to gas temperature and ionization can be modelled in the photo-ionization equations. The initial dust distribution and properties can then be self-consistently modified during the RT.

While the dust treatment implemented is very simple in that it only accounts for dust absorption (i.e. removal of photons from the ionizing flux by dust), the above considerations were kept in mind during the development, so that introducing a more refined dust modelling is relatively easy in the present code framework (Ch. 5).

In the spirit of the modular architecture of CRASH, we created a new software module to include dust following the standard CRASH framework: the dust module

[2]To avoid confusion, in this work we will use "dust species" exclusively in the context of CRASH to refer to this concept.

is configurable by an ASCII text file, which is loaded along the already existing configuration files for other modules. The file specifies which dust species are considered and from where to load the tables with their optical properties and other dust-related initial conditions. These comprise the following 3D fields:

- the dust mass density ρ_d [$\mathrm{g\,cm^{-3}}$]
- the fraction of mass y_k in each dust species k,

which are mapped onto the computational grid. To switch between different models, only a configuration change is required, as model-specific values are loaded from files during simulation initialization.

A FORTRAN TYPE DUST_SPECIES has been created to represent a single dust species and to hold the tables provided by the adopted model. The 3D variability of dust in the computational domain is described with a map of DUST_IN_CELL TYPE variables holding the mass density of dust ρ_d and the species mass fractions y_k in a single cell. According to the frequency sampling adopted in the CRASH spectra, the absorption cross section per mass is computed at each centre-bin frequency ν by taking the mass fraction weighted average of the species cross sections:

$$\frac{\mathrm{d}\sigma_\mathrm{a}(\nu)}{\mathrm{d}m_\mathrm{d}} = \sum_k y_k \frac{\mathrm{d}\sigma_{\mathrm{a},k}(\nu)}{\mathrm{d}m_{\mathrm{d},k}}\,. \tag{4.1}$$

These can be obtained by interpolation of the DUST_SPECIES tables during CRASH initialization to avoid impacting algorithm performance during photon propagation.

When a photon packet crosses a cell, we account for dust absorption by adding a new term to the optical depth τ_ν from Equation (2.18):

$$\tau'_\nu = \tau_\nu + \rho_\mathrm{d} \frac{\mathrm{d}\sigma_\mathrm{a}(\nu)}{\mathrm{d}m_\mathrm{d}} l\,, \tag{4.2}$$

with the cast path l. Equation (2.21) thus becomes:

$$\Delta N_{i,\nu} = \frac{\tau_{i,\nu}}{\tau'_\nu} \Delta N_\nu\,, \tag{4.3}$$

where i, as before, labels the gas components. The photons absorbed by dust are simply removed from the flux; they do not affect the dust status in any way, i.e. its contribution to the optical depth of the cell stays constant in time. This is, naturally, a point to be improved upon in the future by taking into account radiation processes that modify dust properties and by including the gas to dust coupling they introduce. Photoemission of electrons from grains, for example, has already been implemented and will be discussed in Ch. 5.

Apart from the modifications discussed here, the RT proceeds as in § 2.4 and § 2.5.2; specifically the gas ionization equations have not been modified.

4.2 Results

In this section we present the results of RT simulations in different idealized environments: a dusty H II region created by an O–type star (§ 4.2.1) and a small, cubic cosmological volume with an edge length of $0.5h^{-1}$ cMpc in which a few bright stellar type sources propagate their ionizing radiation through dust-enriched gas. The latter test case (§ 4.2.2) is an adapted version of Test 4 introduced in Iliev et al. (2006) and further discussed in Graziani et al. (2013).

The purpose of these simulations is to verify that our code produces sensible results in simplified configurations mimicking different astrophysical environments in which dust is directly observed (e.g. galactic H II regions) or its existence is inferred (e.g. high-z cosmic webs).

Hereafter, the gas is always assumed to be composed of 92 % H and 8 % He by number. At the beginning of any simulation the gas is assumed to be fully neutral and to have a temperature of 100 K. In simulations featuring dust, we assume the dust composition to be the same throughout the entire simulated volume and time.

4.2.1 Dusty, stellar-type H II regions

The configuration we study here oversimplifies the typically clumpy, chemically diverse, dynamic and turbulent star-forming environment, by making the following assumptions[3]:

- The cubic simulation volume of $(85\,\mathrm{pc})^3$ contains homogeneous and static gas with a number density $n_{\mathrm{gas}} = 1\,\mathrm{cm}^{-3}$. This value is typical of the diffuse ionized medium and should be appropriate for an evolved, low-density H II region (e.g. Anantharamaiah 1986; Roshi & Anantharamaiah 2000). The Cartesian grid mapping the volume has a resolution of $N_{\mathrm{c}} = 256$ cells per side, corresponding to a spatial resolution of roughly 0.3 pc.

- We pollute the medium with dust using a fixed GDR. Our reference value is GDR = 124, as proposed by WD01a and LD01 for the diffuse ISM. We also explore cases with GDR = 50 and 1000. Similarly, we adopt $R_V = 3.1$ in the reference case and explore models with $R_V = 4.0$ and 5.5 (cf. Fig 3.6).

- The O–type star is modelled as an ideal black-body source with spectral temperature $T_{\mathrm{bb}} = 4 \times 10^4\,\mathrm{K}$ and emission rate of ionizing photons $Q_0 = 10^{49}\,\mathrm{s}^{-1}$. These values are appropriate for a powerful O–star (Martins et al., 2005). The source spectrum spans the energy range 13.6 eV to 160 eV and

[3] It should be noted that the problem of the expansion of dusty H II regions is far more complicated as dust efficiently couples with radiation (see 2.6). Self-consistent modelling of this problem is beyond the scope of the present work.

it is discretised into $N_\mathrm{f} = 67$ frequency bins with adaptive spacing chosen such as to ensure good sampling of the relevant cross sections (cf. Fig. 3.7). We use 2×10^9 photon packets to sample the source emission. Such a high number is necessary to reach convergence, since especially the dust free and the GDR = 1000 cases proved to be very sensitive to Monte Carlo noise.

- As the lifetime of a massive O–type star ($\lesssim 10\,\mathrm{Myr}$, e.g. Raiteri et al. 1996) is typically much longer than the ideal ionization timescale for a Strömgren sphere (Draine, 2011a, Eq. (15.6)), the H II regions observed in our Galaxy are often assumed to be in equilibrium. We run our simulations for $t_\mathrm{f} = 10\,\mathrm{Myr}$ and find that ionization equilibrium (in H and He) is reached after approximately $1\,\mathrm{Myr}$[4], while temperature equilibrium is only reached towards the end of the simulations.

Fig. 4.1 shows spherical averages of hydrogen and helium ionization fractions as well as gas temperature as functions of distance r from the stellar source. All lines show results at the final simulation time t_f, but correspond to different values of GDR and/or dust models. For comparison we also show the dust-free case. Moreover, we define, somewhat arbitrarily, the radius of the ionization front (I-front) as the one at which $x_{\mathrm{H\,II}}$ drops below 0.9 .

First note that, in absence of dust, CRASH computes an I-front position at radius $r \sim 64\,\mathrm{pc}$. When the medium is polluted by dust using our reference values (dashed red line), the I-front recedes by $\sim 4\,\mathrm{pc}$ (or 6 %) due to the additional contribution to the total optical depth. Also note that homogeneously distributed dust does not change the slope of the ionization front, which maintains its sharp transition to neutral gas. The increase in optical depth naturally depends on the value of GDR and on the model assumptions leading to variations in the corresponding cross section (see Fig. 3.6). Changing R_V at constant GDR, for example, produces small displacements consistent with the lowering of the dust cross section with increasing R_V value.

Close to the source helium is doubly ionized, and $x_{\mathrm{He\,II}}$ is correspondingly smaller than unity. Absorption by dust does not have a strong effect on the helium ionization fractions inside the H II region until the GDR value is decreased below 100, at which point also the He II front begins to recede. This is due to the dust cross section being a factor of two or three larger at H I-ionizing energies than at He I-ionizing energies[5].

[4] To reach equilibrium, time dependent RT codes require several ideal ionization times ($\sim 10^5\,\mathrm{yr}$ in this case), as simple analytic estimates of such timescales do not account for recombinations that have to be balanced by the ionizing source (e.g. Iliev et al., 2006).

[5] We find that when the H II and He II fronts coincide in the dust free medium, as is the case for very hot black-body spectra (cf. Draine, 2011a, Ch. 15), they recede jointly in dust polluted media.

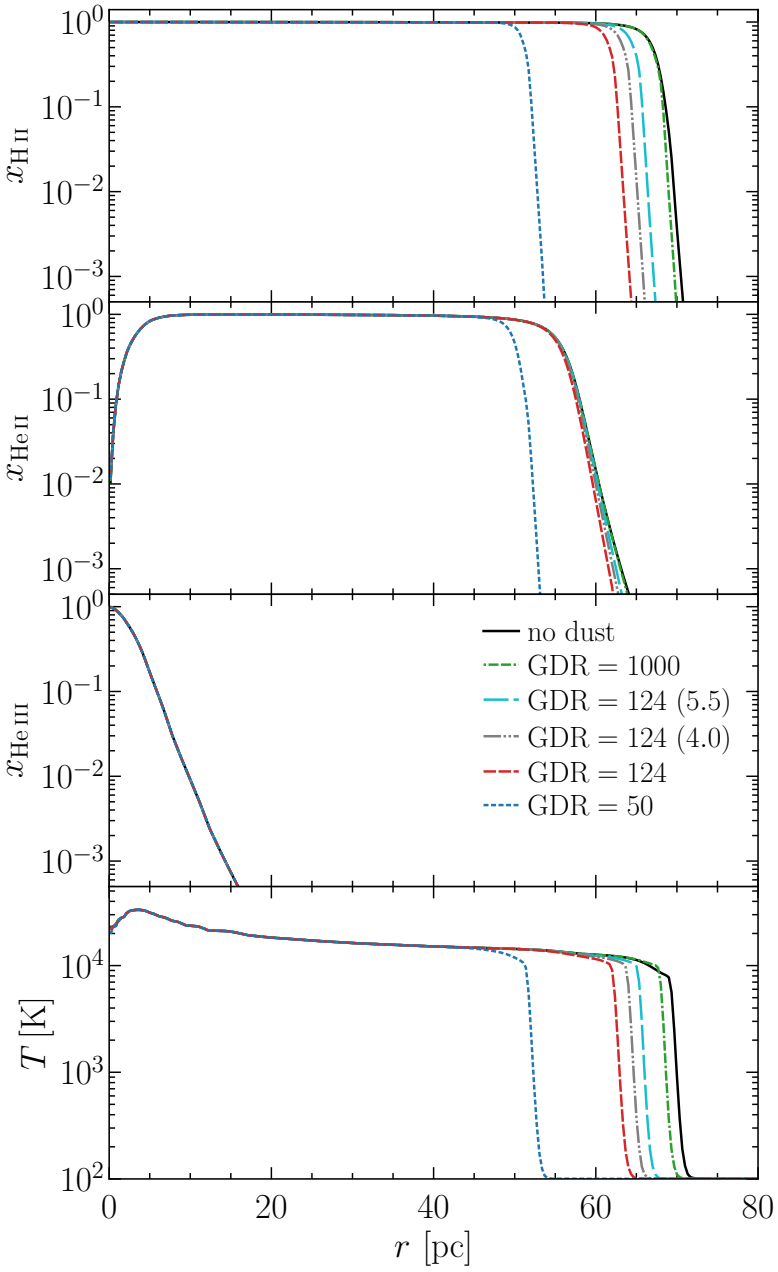

Figure 4.1: Fig. 4 of GCG19. Spherical averages of (from top to bottom) H II fraction, He II fraction, He III fraction and T as functions of distance from the black-body source after 10 Myr for $R_V = 3.1$ and various GDRs as indicated in the labels. As a comparison, we also plot the dust free case (solid black line) and our reference GDR of 124 but with $R_V = 4.0$ and 5.5 (indicated in brackets; see § 3.5.2).

The gas temperature profile (bottom panel) reaches values around $T \sim 10^4\,\mathrm{K}$ where hydrogen is ionized and quickly drops in the neutral region. Helium provides some additional heating close to the source. As in the case of $x_{\mathrm{H\,II}}$, absorption by dust reduces the radius of the heated bubble but does not change the structure in the inner region.

In Fig. 4.2, using the same layout as that of Fig. 4.1, we show the results of exploring different values of the gas number density n_{gas} and source ionizing power (i.e. emissivity Q_0 and black-body temperature T_{bb}), but keeping GDR = 124 (dashed lines). The values chosen for T_{bb} and Q_0 are the highest mentioned in Martins et al. (2005, Table 1) for solar metallicity O V stars. For each simulation we also show the corresponding dust free results (solid lines). Our goal here is to obtain a feeling for the possible variation in size of dusty H II regions as predicted by our code.

By increasing the gas number density to $10\,\mathrm{cm}^{-3}$ and $100\,\mathrm{cm}^{-3}$, the front recedes to 12 pc and 2 pc, respectively, compared to 64 pc for our reference run. The helium ionization regions show the expected behaviour, increasing in size with decreasing density/increasing emissivity and vice versa. Note in the bottom panel that the temperature close to the source is predicted to be higher for weaker sources/higher gas density. This is clearly unphysical and it is owed to the fact that for consistency we used the same spatial resolution of 0.3 pc for all simulations. When we choose more appropriate resolutions to resolve the smaller Strömgren spheres produced at higher densities, this problem is resolved (see inset in last panel).

The effect of dust absorption, again, consists in reducing the size of the ionized regions, while leaving their inner structure unchanged.

We also briefly discuss the effect of dust on ionization fronts in media of lower densities ($n_{\mathrm{gas}} \sim 10^{-3}\,\mathrm{cm}^{-3}$), such as the diffuse IGM. Since photon mean free paths are relatively long, transitions from ionized to neutral gas tend to be more extended and feature long low-ionization tails in these cases. We find that the primary effect of dust pollution then is the cut-off of these tails and that only low values of GDR result in a size reduction of the highly ionized region. This effect can also be seen in the simulations we discuss in § 4.2.2.

Hunt & Hirashita (2009) and Draine (2011b) compiled several observational data sets of galactic and extra-galactic H II regions. Hunt & Hirashita (2009) interpret the observed size-density relation in terms of dynamical semi-analytic models including dust absorption and featuring time dependent Q_0. Starting from different initial densities they account for H II region expansion, but retain the assumption of a homogeneous medium. Draine (2011b), on the other hand, interprets the observations in terms of static models that account for radiation pressure on dust creating central densities lower than those close to the ionization front. Our model equilibrium H II regions are too small for a given density, even in dust free cases, to agree with the observational results. This might indicate that our values for Q_0 are too low (cf.

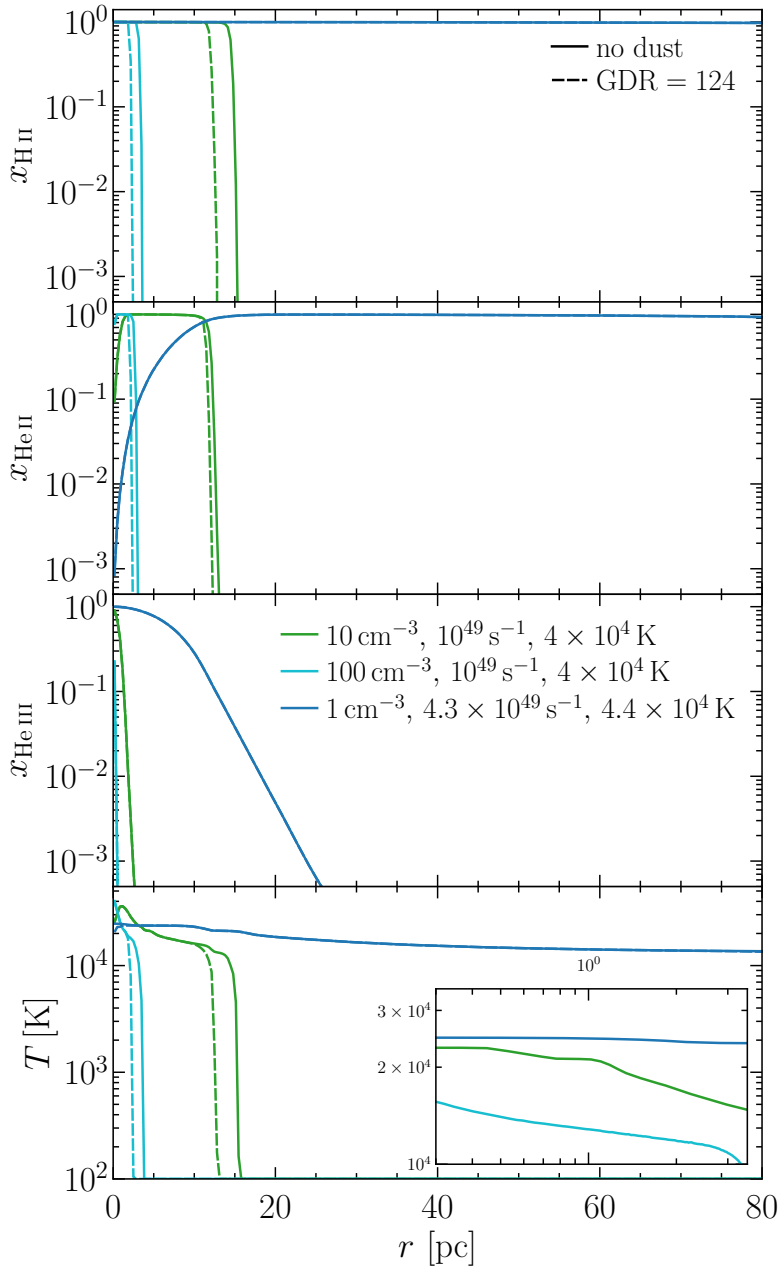

Figure 4.2: Fig. 5 of GCG19. As Fig. 4.1 but showing results of simulations varying the gas number density and source ionization power: (n_{gas}, Q_0, T_{bb}) = ($10\,\mathrm{cm^{-3}}$, $10^{49}\,\mathrm{s^{-1}}$, $4\times10^4\,\mathrm{K}$) in green, ($100\,\mathrm{cm^{-3}}$, $10^{49}\,\mathrm{s^{-1}}$, $4\times10^4\,\mathrm{K}$) in light blue, and ($1\,\mathrm{cm^{-3}}$, $4.3\times10^{49}\,\mathrm{s^{-1}}$, $4.4\times10^4\,\mathrm{K}$) in blue. Dashed lines refer to simulations with GDR = 124, while solid lines correspond to results for dust free media. In the bottom panel we also show the temperature profile of high resolution runs close to the source.

Hunt & Hirashita, 2009, § 4.4), or that the assumption of a homogeneous medium should be removed by accounting for spatial variations of gas density or clumpiness of dust polluted regions. A detailed comparison of these models to our code could provide interesting insights but would go beyond the scope of this work.

After discussing the equilibrium configurations found in our simulations, we now go over to investigating the effect of dust on the time evolution of H II regions. Fig. 4.3 shows the growth in time of the ionized bubble at different GDR values, and Fig. 4.4 shows the expansion speed of the corresponding ionization fronts as a function of time. While initially all fronts coincide and propagate at the same speed, slowdown, dropout and stagnation of fronts in the order of increasing GDR value can be observed at later times when the photons have to traverse a considerable dust column in order to reach the front. The slowdown due to dust absorption might have implications for the overlap of ionized bubbles and consequently for the percolation of dusty media containing several sources (see also § 4.2.2). Note that we lack the numerical precision to accurately compute speeds lower than $\sim 10\,\mathrm{km/s}$ and that we attribute the premature speed drop in the dust free case to this fact.

A word of caution concerning all above findings is necessary at this point, since our limited dust implementation is not directly coupled to the gas. We work on implementing also grain charging, which results in grains and gas sharing the free electron population[6]; this introduces direct feedback of dust on gas recombination and cooling, since energetic photo-electrons released from the grains will provide an additional channel for the radiation field to heat the gas. Whether grains provide net heating or cooling thus likely depends on the specific environment being considered (e.g. Weingartner & Draine, 2001b). The current state of our charging implementation is discussed in Ch. 5.

4.2.1.1 The impact of PAHs

In this section we quantify the impact of PAH removal (§ 3.5.3) on the ideal H II region size of our simple model. Ideally, one should couple the evolution of the PAH population to the RT in time by directly implementing PAH destruction and creation processes in the gas chemistry. However, here we take a far simpler approach and compare simulation runs adopting mixtures with and without PAHs to assess the maximum possible effect on the spherical H II profiles at equilibrium time.

After verifying that the differences between the dust cross sections we computed and those directly provided (see solid black versus dashed red lines in Fig. 3.8) have no significant impact, we discuss the effects of removing the PAH component (in

[6]Note that in general dust will not significantly impact the free electron density in ionized regions, since there is far more mass (and therefore electrons to be released) in the gas than in the dust. In photon-dominated regions, on the other hand, gas-dust reactions can change the electron density (Abel et al., 2008).

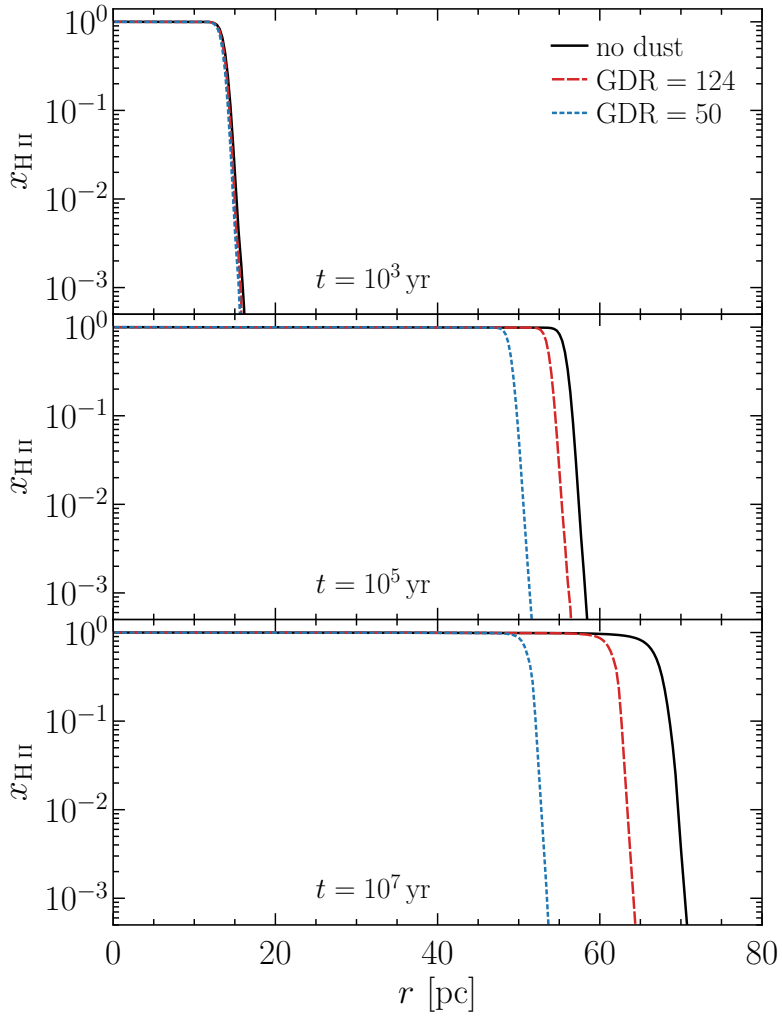

Figure 4.3: Fig. 6 of GCG19. Spherical averages of $x_{\mathrm{H\,II}}$ as function of distance from the black-body source for the dust free case and GDR values 50 and 124 at simulation times 10^3 yr (upper panel), 10^5 yr (middle) and 10^7 yr (lower).

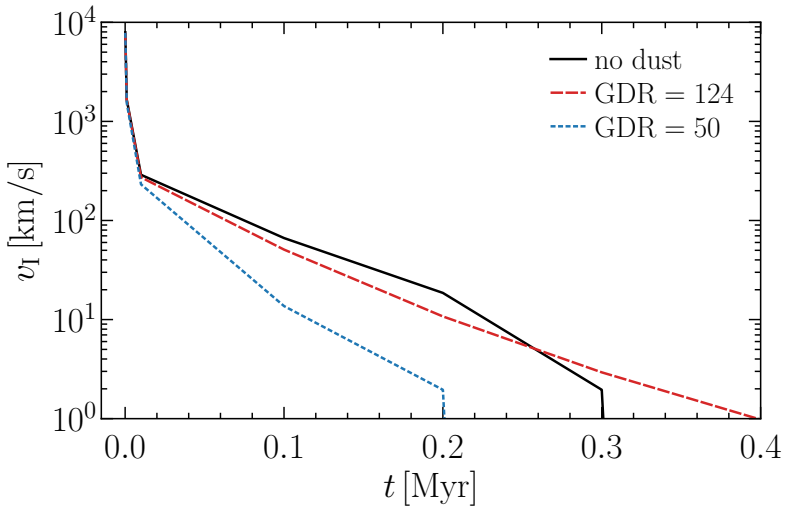

Figure 4.4: Fig. 7 of GCG19. Expansion speed of the H II ionization front as a function of simulation time for the dust free case and GDR values 50 and 124.

the $b_{\rm C} = 0.0\,$ppm approach) in Fig. 4.5 using the example of our reference case (GDR = 124) and the case of GDR = 50.

In our reference case, the effect of the PAH component can be appreciated only in the I-fronts of the hydrogen and temperature profiles, which lie between the full dust and no dust cases as expected, while it is completely negligible in the ionization fractions of helium. This is in line with the finding from the previous section that dust absorption leaves the inner structure of ionized regions unchanged and only affects their fronts. It is thus interesting, albeit purely coincidental, to note that in the GDR = 50 case, the removal of the PAH component nullifies the effects of the dust in the He II profile, while it provides almost identical fronts to the full dust GDR = 124 case in both hydrogen and temperature profiles.

We also tested the PAH impact on the I-front velocity profiles of the H II region, finding that in the GDR = 124 case the absence of the PAH component results in a front speed equivalent to the dust free case (black line in Fig. 4.4). For GDR = 50, instead, the front expands at a rate similar to that of full dust GDR = 124 case.

We have verified that the above conclusions hold qualitatively also if the source has a black body spectral distribution peaking at $\sim 17\,$eV, where PAHs provide the highest absorption, finding no evidence for a strong dependence of our results on the spectral shape.

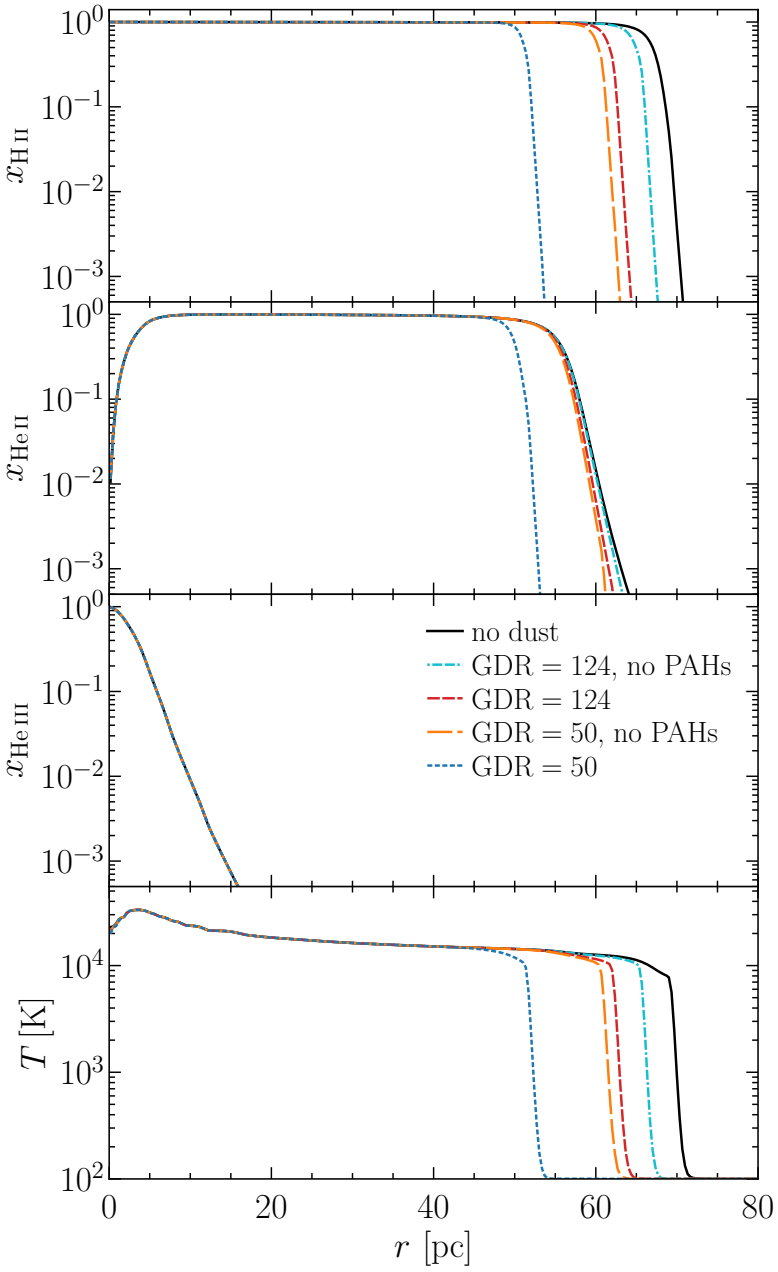

Figure 4.5: Fig. 8 of GCG19. As Fig. 4.1, but showing results including (excluding) the PAH contribution to the cross section for GDR = 124 in dashed red (dash-dash-dotted cyan) and for GDR = 50 in dotted blue (long dashed orange). For reference, we also show the dust free case (solid black).

The impact of the PAH component will be explored again in § 4.2.2 to investigate a more complex scenario involving a realistic cosmic web and a combination of sources.

4.2.2 RT through a dusty cosmological volume

Here we examine the combined effect of several stellar-type sources on a small cosmic web artificially polluted with dust. This allows us to investigate if a diffuse dusty medium can affect the global pattern of overlapping H II regions with respect to a dust free medium and thus change the morphology and timing of the resulting small scale reionization driven by galactic sources.

To mimic the above process, we adopt the simulation set-up of Test 4 of the *Cosmological Radiative Transfer Comparison Project* (Iliev et al., 2006), which was later adapted by Graziani et al. (2013) to investigate the effects of atomic-metal pollution. We only briefly describe the RT configuration here and refer to the original papers for more details. The simulation has a box size $L_\mathrm{b} = 0.5h^{-1}\,\mathrm{cMpc}$ ($h = 0.72$), a grid resolution $N_\mathrm{c} = 128$ (corresponding to a spatial resolution of $4h^{-1}\,\mathrm{ckpc}$), a volume-averaged gas density $\langle n_\mathrm{gas}\rangle \approx 2.3 \times 10^{-4}\,\mathrm{cm}^{-3}$ and $t_\mathrm{f} = 0.5\,\mathrm{Myr}$ starting at redshift $z = 9$. The cosmological density evolution is not accounted for. A total of 16 hard black-body type sources ($T_\mathrm{bb} = 10^5\,\mathrm{K}$) with emissivities $Q_0 \sim 10^{52}\,\mathrm{s}^{-1}$ are distributed throughout the volume, and their spectra are sampled using 21 frequencies. 10^8 photon packets are emitted per source, resulting in sub-permille variations of volume averages when compared to test runs with 2×10^8 packets.

The gas number density in a slice cut of the simulation volume is shown in Fig. 4.6. The plane of the slice cut has been selected to intercept one of the most luminous sources as also done in Graziani et al. (2013).

We pollute the medium with dust by simply scaling the gas mass in each cell with a GDR of 124. Note that this, though guided by literature results, is an essentially arbitrary choice and most likely an overestimation of the dust abundance at $z = 9$, which is observationally unconstrained. Moreover, the restrictions concerning dust evolution and its consequences on extinction as discussed in Ch. 3 apply. Our simulation can therefore only give first qualitative results assuming early and efficient dust pollution, which is not inconceivable at this scale. To emulate a decrease of GDR with increasing distance from galactic centres (e.g. Giannetti et al., 2017), we also perform a test using overdensity ($\Delta = n_\mathrm{gas}/\langle n_\mathrm{gas}\rangle$) dependent GDRs. We find that the results shown in the following remain largely unaffected when using GDR = 124 in cells with $\Delta > 100$, GDR = 500 for $10 < \Delta < 100$ and GDR = 1000 (10^6) in all other cells, even though doing so decreases the total dust mass in the simulation volume to $\sim 15\,\%$ ($\sim 5\,\%$) with respect to the constant GDR case. In future studies we plan to investigate initial conditions generated by hydrodynamic simulations that treat dust in a self-consistent manner (cf. § 3.6). The spatial dust distribution is, however, also highly uncertain from the point of view of such simulations, especially

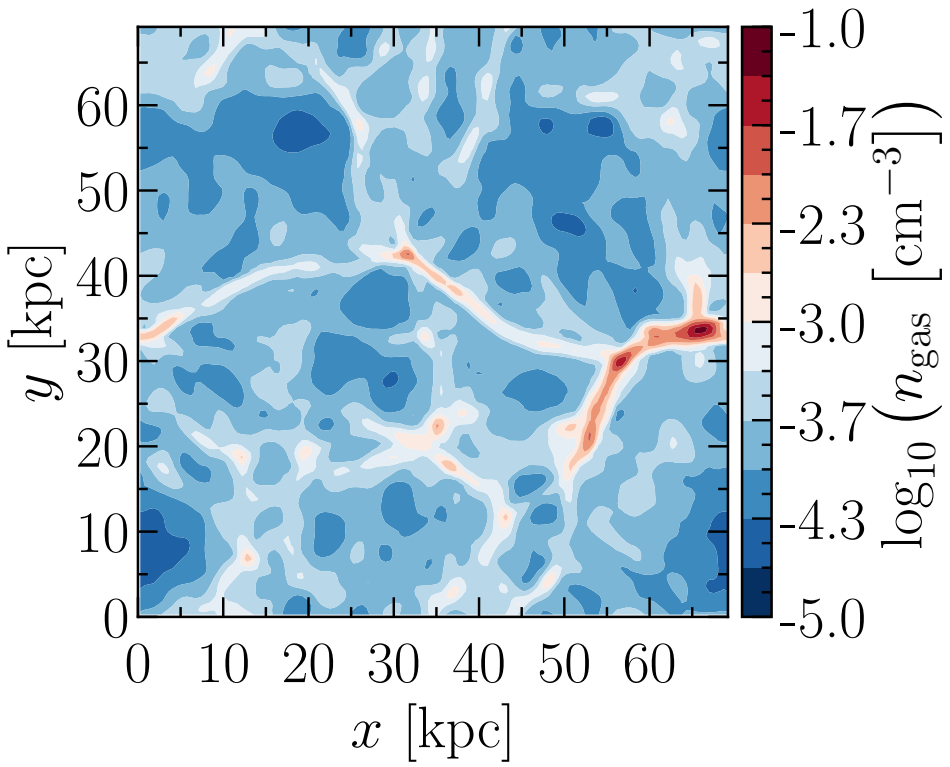

Figure 4.6: Fig. 9 of GCG19Contour map of the gas number density in a slice cut of the simulated cosmological volume.

on the circumgalactic medium scale, where it strongly depends on the adopted feedback model.

In Fig. 4.7 we present contour maps of the plane shown in Fig. 4.6 at the time $t = 5 \times 10^4$ yr, comparing results obtained without dust (left), with the full dust mixture (middle) and with PAH free dust (right). The volume averaged H ionization fractions are 0.14, 0.12 and 0.13, respectively. First note that, owed to the shape of the spectrum of the sources, He II regions tend to be more extended than H II regions (see also Graziani et al., 2013, Fig. 3 and § 5.2.3). Moreover, it is difficult to investigate the shape of a single ionized region as there are multiple sources in the main overdense filament seen in Fig. 4.6, and at the chosen time several ionized bubbles already overlap. In the top panels, where ionized hydrogen is shown, we immediately note the sharpening of ionization fronts. The degree of H II region overlap

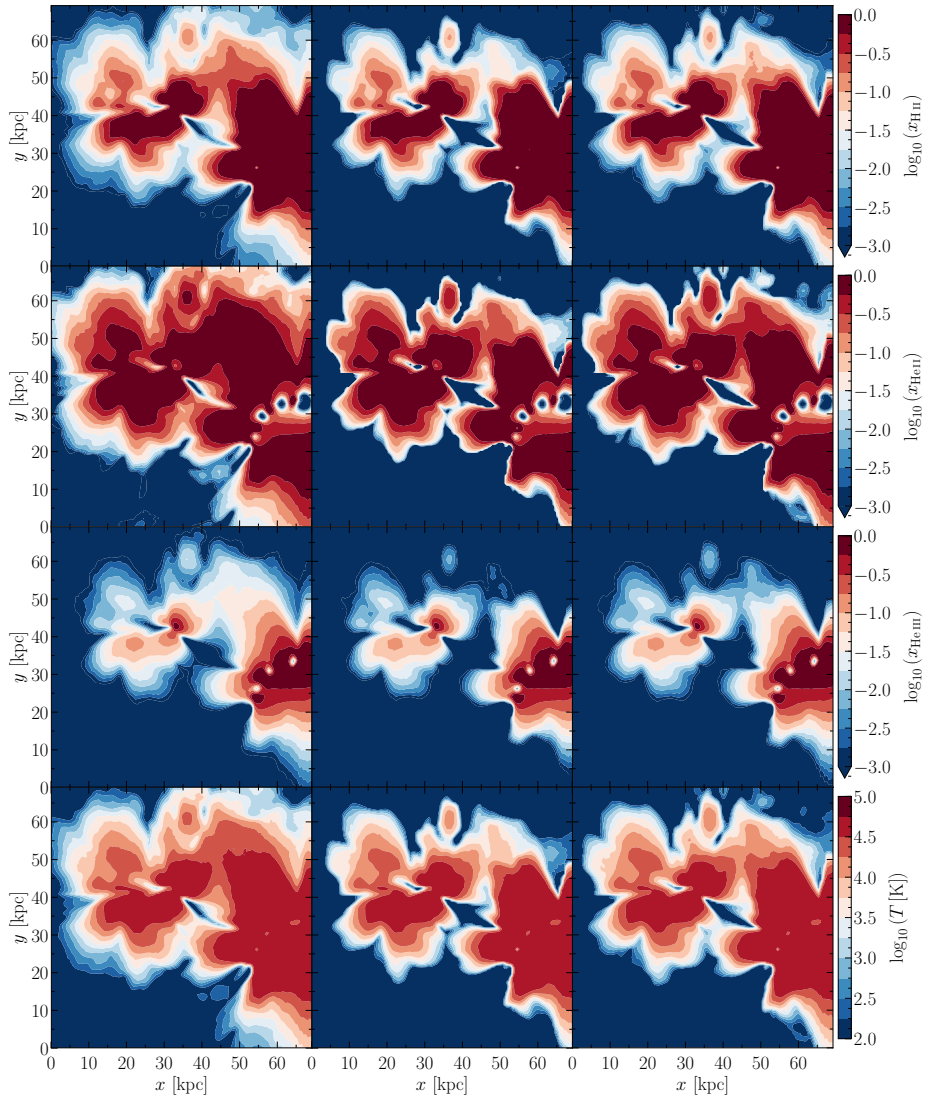

Figure 4.7: Fig. 10 of GCG19. Contour maps of a slice cut through the simulation volume at time $t = 5 \times 10^4$ yr. From top to bottom the panels show: H II fraction, He II fraction, He III fraction and temperature. The columns show dust free results, results with full dust pollution and results with PAH free dust pollution from left to right.

is consequently reduced by the presence of dust, changing the spatial distribution of the ionized regions in the polluted medium. An even more pronounced effect is visible in the $x_{\mathrm{He\,II}}$ and $x_{\mathrm{He\,III}}$ patterns, where the ionizing flux subtracted by the dust also favours a faster helium recombination. In the bottom panel, the gas temperature distribution is shown. The indirect effects of dust absorption on the gas temperature are evident in the form of a less progressive transition between cold ($T \sim 10^2\,\mathrm{K}$) and hot ($T \sim 10^4\,\mathrm{K}$) gas. We call particular attention to two points: first, note how at coordinates (45 kpc, 45 kpc) in the second row the highly ionized regions overlap in the dust free case, whereas they hardly touch in the dust polluted case. Second, one can appreciate at (40 kpc, 35 kpc) how self-shielding neutral pockets can survive longer in the presence of dust.

The effects of removing the PAH component correspond to what one would expect from our study of single H II regions, i.e. without PAHs the I-fronts fall between those of the dust free and full dust cases. We do therefore not discuss the right column in more detail.

The volume averages of $x_{\mathrm{He\,II}}$ and T are most affected by the presence of dust. In Fig. 4.8 we therefore show their time evolution. At 0.2 Myr, the dust free case has a volume averaged $x_{\mathrm{He\,II}}$ (T) of 0.54 ($3.2 \times 10^4\,\mathrm{K}$), which is reduced by 20 % (25 %) in the full dust case and 12 % (16 %) in the PAH free case.

To investigate the dependence on the spectral shape of all the above findings, we performed simulation runs in which we used $T_{\mathrm{bb}} = 4 \times 10^4\,\mathrm{K}$ black-body spectra for the sources, while keeping all the other parameters fixed. The associated shift in the spectrum peak primarily results in less helium ionization and in a lower average gas temperature, but qualitatively the above observations still hold.

Dust can offer significant absorption at ionizing energies. The simple cases studied here show sensitive alterations of size, shape and time evolution of ionized regions: ionization fronts get sharpened, the size of fully ionized regions is reduced changing their degree of overlap and the gas temperature is lowered. These effects can certainly have a strong impact on small scale RT simulations, where dust is known to be present and its spatial extent can be resolved. It should be considered, however, that other physical processes currently not included in our implementation can be important. In particular, dust photo-heating is likely to have an impact on the gas temperature and will have to be accounted for in the future. Further observational and numerical investigations of the spatial distribution, abundance and physical properties of dust are required in order to critically examine the assumptions made, to determine the appropriate physical set-up of future RT simulations and to precisely quantify the impact of absorbing grains on the final ionization and temperature patterns created in the many different environments of both the ISM and the IGM.

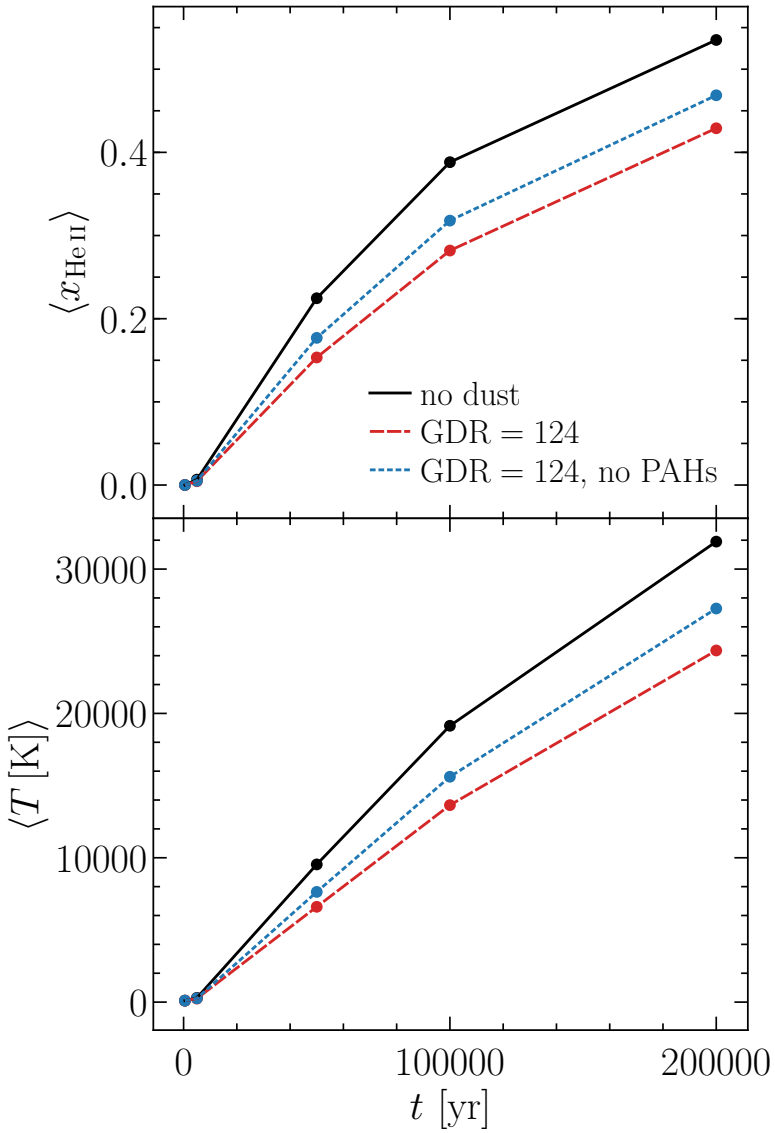

Figure 4.8: Fig. 12 of GCG19. Time evolution of the volume averaged $x_{\rm He\,II}$ (top panel) and T (bottom) for our dust free (solid black line), GDR = 124 (dashed red) and PAH free (dotted blue) run.

Chapter 5

Radiative transfer through gas and dust: charging

The evolution of a cosmic dust grain is driven by interactions with the surrounding gas (e.g. collisions with ions and molecules), the ambient radiation field (e.g. absorption, scattering, photo-electron emission), and other grains (e.g. coagulation, shattering). These will generally result in the grain obtaining a non-zero electric charge eZ, with the elementary charge e, which in turn heavily affects subsequent interactions. Below we revisit some aspects of the dust life cycle with an emphasis on the role of grain charge, which was neglected in our discussion in Ch. 3 to keep it concise.

In cold molecular clouds, likely shielded from UV radiation, grains can interact with highly penetrating X-/cosmic rays and their secondary products, inducing changes in grain charge. This process has a strong impact on grain surface chemistry because it alters the rate of ion adsorption and the efficiency of ice mantle formation (e.g. Ivlev et al., 2015). Where the density of dust is sufficiently high, as in proto-planetary disks or dense cloud cores, the grain size/shape distribution evolves through coagulation and fragmentation, processes that strongly depend on grain charge (e.g. Dominik & Tielens, 1997; Akimkin et al., 2020). This has profound implications for the dust optical properties and thus for the extinction curve (e.g. Hirashita, 2012). Recent, spatially resolved ALMA[1] observations of proto-planetary discs (e.g. Birnstiel et al., 2018), as well as far IR/sub-mm observations of variations in dust opacity along ISM lines of sight containing dense clouds, provide evidence for such grain size/shape evolution (e.g. Köhler et al., 2012; Tazaki et al., 2019).

In the diffuse, warmer ISM, grains are exposed to a wider photon energy range and their interaction with the radiation field is complicated by the possible presence of electrically charged PAHs[2] (e.g Siebenmorgen et al., 2014). As the ambient medium becomes hotter and ionized, grain destruction channels (e.g. sputtering) open up, the efficiency of which also depends on grain charge (e.g. Murga et al., 2019).

Finally, in extreme environments illuminated by gamma-ray bursts or active

[1] `https://www.almaobservatory.org`

[2] PAH emission features are generally associated with atomic gas, while they are suppressed in ionized regions. The presence of PAHs in molecular gas is debated (see § 3.1).

galactic nuclei, high energy photons could increase grain charges to excessive values and induce Coulomb explosions (e.g. Waxman & Draine, 2000; Tazaki et al., 2020).

When studying the growth of grains in the ISM, their charge has to be considered, as the arrival rate of candidate ions for accretion (e.g. Si II) can be significantly modified by a non-zero charge (e. g. Zhukovska et al., 2018). Since grain growth in shielded, cold clouds seems problematic due to ice mantle formation (Ceccarelli et al., 2018), photo-electric charging could play a significant role in the growth process of all grains stable to radiation exposure. Small grains, which account for most dust surface area and are found to be more likely to be negatively charged compared to larger particles (e.g. Ibáñez-Mejía et al., 2019), are primary candidates for accreting positive ions (e.g. Weingartner & Draine, 1999) and thus accounting for most of the ISM growth. Note that there is a general consensus among recent hydro-dynamical and semi-analytic models of galaxy formation (e.g. Mancini et al. 2015; McKinnon et al. 2017; Popping et al. 2017; Gioannini et al. 2017; Aoyama et al. 2018; Graziani et al. 2020) that some form of grain growth is necessary to reproduce the total mass of dust in galaxies across cosmic timescales (see § 3.6 and also § 3.4).

Charge is a parameter of fundamental importance to the dynamics of grains in a plasma (e.g. Melzer, 2019). This has been studied in some detail in the interplanetary plasma (e.g. Mendis & Rosenberg, 1994), where direct observations and even in-situ measurements are available. It likely also plays a crucial role in stellar and galactic winds, which are often dusty (e. g. § 2.6 and Veilleux et al. 2005). Coulomb drag on charged grains, for example, could significantly alter the dynamics of H II regions (Akimkin et al., 2015, 2017) and radiation-pressure-driven winds (Hirashita & Inoue, 2019).

Grain charging contributes to regulating the thermal status of a plasma via photo-electric emission (e.g. Draine, 2011a); as described in van Hoof et al. (2004), small dust grains dominate the photo-electric heating and cooling contribution of dust and could, in fact, be quite important in certain environments.

Finally, note that the interaction of photons with dust will be influenced by its charge. For example, the photo-electric yield (§ 5.1.2) of positively charged grains is reduced w.r.t. neutral grains, which could enhance photo-destruction, as it inhibits photo-electrons from carrying away energy absorbed by the grain (e.g. Murga et al., 2019). Furthermore, absorption and scattering cross sections are different for neutral and charged grains (e.g. Bohren & Hunt, 1977; Heinisch et al., 2012; Kocifaj & Klačka, 2012; Kocifaj et al., 2012). This could impact dust extinction but also temperatures and emission spectra, especially of very small grains. For low charge numbers ($|Z| \sim 1$), the change in the absorption cross section of several PAHs has been investigated (e.g. Malloci et al., 2007) and is accounted for in some form by many dust models (e.g. LD01; Draine & Li 2007; Mulas et al. 2013). For other candidate components of cosmic dust populations, such studies seem to be missing;

the same applies to radiative transfer models that self consistently account for this effect.

While dust evolution is profoundly impacted by the charging process, to our knowledge, no available galaxy formation model explicitly accounts for it since the physics regulating the process of charging depends on a number of variables at the ISM scale, poorly constrained or unresolved in numerical simulations: e.g. the free electron temperature, the plasma ionization status and chemical composition, as well as the presence of a UV and/or X-/cosmic ray flux. The relevant environmental conditions are difficult to reproduce in sub-grid models. Also note that all the above quantities can significantly vary both across galactic environments (e.g. Ibáñez-Mejía et al., 2019) and in time, as a result of the progress of star formation. Dependencies on the solid state properties of the grains (e.g. amorphous vs crystalline), on their shapes (e.g. spherical vs aggregates, Ma et al. 2013), sizes and chemical compositions (e.g. silicate vs carbonaceous dust) further complicate the theoretical modelling of the process (Draine & Sutin 1987; Weingartner & Draine 2001b; Weingartner et al. 2006, hereafter DS87; WD01b; WDB06).

Photo-ionization codes are a powerful tool to study grain charging and provide insights for galaxy formation models, since they follow the radiation field and gas ionization, which provides electrons to be accreted by grains. To our knowledge, charging is only accounted for by CLOUDY (Ferland et al., 2017; van Hoof et al., 2020) (in 1D) and MOCASSIN (Ercolano et al., 2003, 2005, 2008) (in 3D), with both codes providing steady state solutions, i.e. disregarding any temporal evolution.

Grain charging in CLOUDY was first introduced by Baldwin et al. (1991). Their approach consists of computing a surface potential for each considered grain material (e.g. graphite, silicate) at each point in space, neglecting grain size dependencies or averaging them out. MOCASSIN has adopted this approach and refined it by explicitly considering the strong grain size dependence (see § 5.1).

In van Hoof et al. (2004) a major upgrade to the grain model of CLOUDY was performed. A Mie theory (Mie, 1908; van de Hulst, 1957; Bohren & Huffman, 1983) implementation, based on Hansen & Travis (1974), was introduced in order to be able to work with arbitrary size distributions of spherical grains of arbitrary composition. In each bin of the size distribution chosen for each composition, intrinsic (absorption and scattering opacities) and derived (temperature, charge) physical grain properties are computed. The process of grain charging, in particular, is implemented in the form of a "hybrid" model (van Hoof et al., 2004; Abel et al., 2005), which modifies the treatment introduced in WD01b with the aim of resolving the charge distribution (see § 5.1.3) of small grains ($a < 1\,\mathrm{nm}$), while computing an average charge for large grains. This allows to capture the physics of small grains in detail while avoiding the computational cost associated with computing charge distributions of large grains.

In this chapter, we present a first implementation of the grain charging process in CRASH and we discuss the spatial distribution of grain charges in typical H II regions

created by a single star and a stellar population including binaries. The chapter is organised as follows: § 5.1 briefly reviews the required grain charging physics and the temporal evolution of the process is discussed in § 5.1.3. The numerical implementation in CRASH is presented in § 5.2 and first results are discussed in § 5.3. Details on improvements to our framework since the publication of GCG19 (Ch. 4) can be found in App. B and App. C, and details on how electron yields (§ 5.1.2) are computed in App. D. Finally, we compare our implementation to the analytic solution of highly idealized configurations in App. E.

5.1 Grain charging processes in a plasma

In this section we summarize the principal grain charging processes active in an astrophysical plasma pervaded by a radiation field. As in § 2.2, the plasma is described by its number density $n_{\mathrm{gas}}\,[\mathrm{cm}^{-3}]$, its temperature $T\,[\mathrm{K}]$ and ionization state; the cosmological abundance ratio is assumed for hydrogen and helium (i.e. $f_{\mathrm{H}} = 0.92$ and $f_{\mathrm{He}} = 0.08$), while molecules and atomic metals are not accounted for.

Hereafter, we follow the approach of WD01b, who base their prescription for collisional charging on DS87. In light of the capabilities of our RT code (§ 2.5), we also account for the extension of their photo-electric charging prescription to X-ray energies described in WDB06. WD01b and WDB06 use the framework of the Silicate-Graphite-PAH model (§ 3.5.2), which, as in GCG19 (Ch. 4), we will adopt where concrete values are required while aiming to keep any numerical implementation general.

5.1.1 Collisional charging

A dust grain will be subject to collisions with charged particles of any species present in the plasma[3]. For large grains, the collisional cross section can be approximated to first order, i.e. by assuming monopole-monopole interaction between the particle and the grain, neglecting perturbations of the grain's charge distribution[4] caused by the incoming particle. A proper treatment for small grains, on the other hand, should account for the fact that the incoming charge could polarize the grain, creating an "image potential" (Jackson, 1962) and significantly enhancing the cross section. See DS87 for details.

Free electrons are the most important collision partners due to their high abundance and velocities. Upon collision with a grain, an electron may be reflected or transmitted and escape to infinity. On the other hand, it may stick to the grain with a probability

[3] Collisions with neutral particles are not of interest here.

[4] N.b.: "charge distribution" here refers to the physical distribution of charge inside a single grain, which is assumed to be spherically symmetric when undisturbed. It is different from the charge distribution mentioned in the introduction of this chapter and discussed in § 5.1.3.

given by the sticking coefficient s_e, adding a negative charge and lowering Z. s_e is highly uncertain and it depends on grain properties (composition, a, Z) and the electron's kinetic energy[5]. If the electron's kinetic energy is high enough, the collision could free one (or more) secondary electron(s), increasing Z (see Draine & Salpeter 1979a).

Collisions with ions present in the plasma (e.g. H II) can also occur, but ions are generally less abundant and slower than electrons and will thus collide less frequently with dust grains. If a collision takes place, the ion is most likely neutralized by electrons from the grain[6], increasing Z. The resulting atom may be released back to the gas phase or it may remain adsorbed to the grain, the outcome being inconsequential to Z. Adsorption likely occurs in partially ionized media, where grains carry negative charges (see the introduction of this chapter and, for an extended discussion, Zhukovska et al. 2018).

Grain-grain collisions, finally, are rare in tenuous media and are thus neglected in our discussion.

Given the above, the charging current experienced by a grain of some composition due to thermal collisions with plasma species i (excluding secondary ionization in the case of electrons), can be expressed as follows:

$$J_i = q_i n_i s_i(a, Z) \sqrt{\frac{8kT}{\pi m_i}} \hat{J}(T, a, Z, q_i)\,, \tag{5.1}$$

where n_i is the number density of species i, q_i its charge, m_i its mass and s_i its sticking/neutralization coefficient. Expressions for $\hat{J}$ can be found in DS87. The charging current due to thermal electrons ejecting secondaries ($J_\mathrm{sec,gas}$) has been modelled by Draine & Salpeter (1979a, § III a) ii)).

In the top panel of Fig. 5.1 we show the electron charging rate coefficient $\alpha = J_\mathrm{e}/(-en_\mathrm{e})$ as a function of the plasma temperature for neutral grains of different sizes. Note that due to the associated uncertainties, WD01b provide identical prescriptions for J_e for both carbonaceous and silicate grains, even though there is likely a composition dependence in reality. α varies strongly with grain size, as expected due to the variation in geometrical cross section. Note, however, that despite their smaller sticking coefficient, the rate coefficient (and thus rate) for small grains is enhanced. One would expect a factor of $\sim 10^6$ between the rates for the 0.001 µm and the 1 µm grain, but at 100 K the resulting value is only $\sim 10^5$ due to the small grain effect discussed above.

[5]The latter and the composition dependency are neglected by WD01b (see their § 3.1).

[6]Neutralization of the incoming ions is likely to occur because the minimum energy required to remove an electron from a bulk solid (the so called work function, e.g. Willis et al. 1973), is generally smaller than the ionization potential of individual atoms, although for grains finite size effects apply. WD01b assume a constant neutralization coefficient $s_\mathrm{n} = 1$ for all ions.

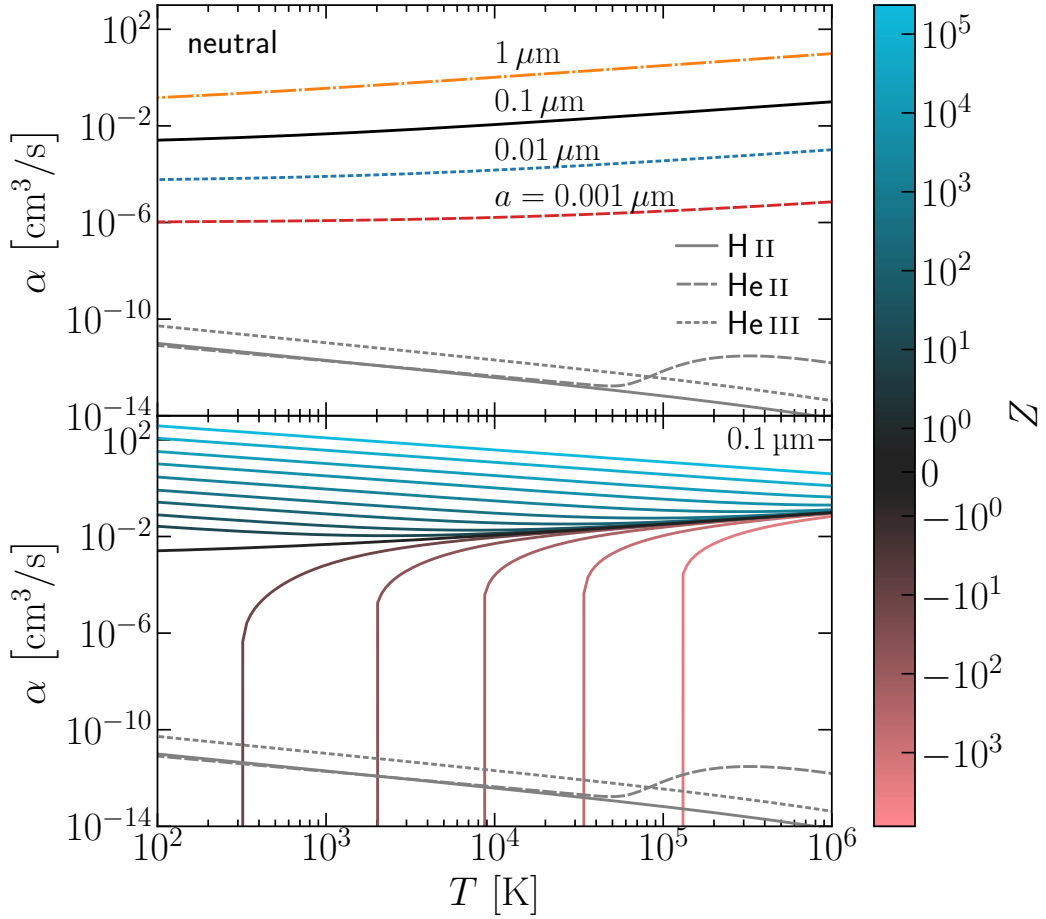

Figure 5.1: Electron charging rate coefficient as a function of plasma temperature for neutral grains of different sizes (top panel, indicated by the line style and colour) and for a grain of 0.1 µm with different charge numbers (bottom panel, indicated by line colour as shown by the colour bar in symlog scale). Also shown are the hydrogen and helium recombination rate coefficients (grey lines, cf. Fig. 2.2).

In the bottom panel, we show α for $a = 0.1\,\mu\mathrm{m}$ and different charge numbers as indicated by the line colour. Hereafter, $0.1\,\mu\mathrm{m}$ is our reference grain size as it is typical of the diffuse ISM and it will be represented by a solid black line in its neutral state. The lower limit on the charge numbers shown is set by auto-ionization (cf. WD01b, Eq. (24)), while the upper limit is set by Coulomb explosion, assuming a tensile strength $S_{\max} = 10^{11}\,\mathrm{dyn\,cm^{-2}}$ for both grain materials (cf. WDB06, § 10.2.1). The auto-ionization limit for carbonaceous grains is slightly lower, so it was chosen here. Positive grain charges result in a higher charging rate due to Coulomb focussing, which is more efficient for slower electrons (low temperatures). For negative charges, the rate is zero at low T until the electrons have enough kinetic energy to overcome Coulomb repulsion, at which point it very steeply rises, soon reaching values comparable to those of the neutral case.

For comparison we also show the hydrogen and helium recombination rate coefficients in both panels (grey lines, cf. Fig. 2.2).

5.1.2 Photo-electric charging

An astrophysical plasma will generally be pervaded by electromagnetic radiation, resulting in the absorption of photons by grains (cf. Chs. 2, 3 and 4). Fig. 5.2 shows the volume-normalized absorption cross section as a function of photon energy $h\nu$ for grains represented by homogeneous spheres of graphite (top panel) and silicate (bottom panel) of different radii (lines), computed in the Silicate-Graphite-PAH framework as described in App. C. The computation assumes neutral grains, but these values are also adopted for charged grains, since no prescription for the computation of their cross sections is available[7]. For $h\nu < 200\,\mathrm{eV}$ and $a < 0.1\,\mu\mathrm{m}$, different resonances are present across grain compositions, while larger grains show a flat dependency on $h\nu$[8]. At X-ray energies, absorption edges are visible since photons can interact with single constituent atoms. Finally, note that the increase of σ_a/a^3 at $h\nu < 10\,\mathrm{eV}$ present for small graphite grains corresponds to the 2175 Å extinction bump (cf. Draine 2011a, Fig. 24.1 and § 3.1).

A photon absorbed by a dust grain may eject electrons from it, thus increasing Z. The average number of electrons ejected following an absorption event with a fixed set of parameters is referred to as photo-electric yield Y. WD01b have computed separate yields for carbonaceous and silicate grains at low photon energies ($h\nu \leq 20\,\mathrm{eV}$) accounting for the dependence on a and Z. Note that at these energies, electrons are ejected primarily from the band structure of a grain.

WDB06 updated the yield computation to treat additional processes occurring for $20\,\mathrm{eV} < h\nu \lesssim 10\,\mathrm{keV}$. High-energy photons can eject electrons from the inner shells of a grain's atoms, possibly inducing a cascade of Auger electrons if the first electron

[7] Cross sections for singly charged PAHs, however, are provided (see LD01 and App. A).
[8] Referred to as "grey" absorption.

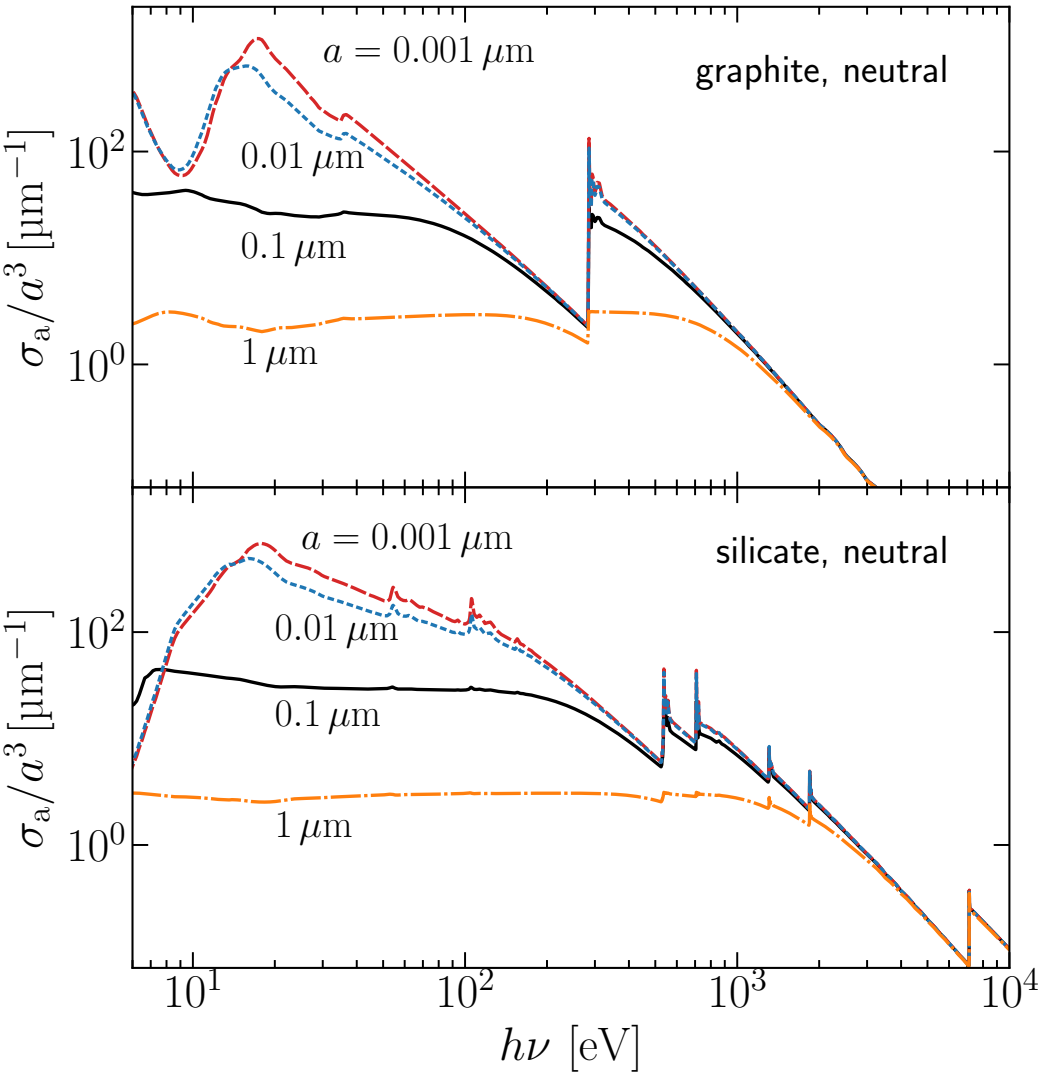

Figure 5.2: Absorption cross sections normalized to volume for neutral graphite (top panel) and silicate (bottom panel) grains of different sizes (indicated by the line style and colour) as functions of photon energy.

comes from a shell below the highest occupied one. In analogy to the secondary ionization process occurring in a gas photo-ionized by X-rays (see Graziani et al. 2018 and § 2.5), photo-electrons released with high energy can themselves excite secondary electrons before leaving the grain. WDB06 provide an expression for each process and sum up all contributions to compute the total yield Y:

$$Y = Y_{\rm band} + Y_{\rm inner} + Y_{\rm A} + Y_{\rm sec}\,, \tag{5.2}$$

where $Y_{\rm band}$ is the band structure yield, $Y_{\rm inner}$ accounts for inner atomic shells which are not part of the band structure, $Y_{\rm A}$ is the associated Auger yield, and $Y_{\rm sec}$ denotes the secondary yield, which is computed for each of the three previous yields.

Fig. 5.3 shows Y for $Z = 0$ as a function of $h\nu$, for different grain radii (lines) and materials (panels). The yields are computed using our implementation following WDB06 (see App. D) and are tabulated in order to be included in our RT code (see § 5.2).

Grains of our reference size 0.1 µm (black lines) show an increasing trend up to $h\nu \sim 20\,\mathrm{eV}$ and a successive decrease until $h\nu \sim 50\,\mathrm{eV}$, where their yield starts to increase again up to X-ray energies ($h\nu \sim$ keV). A strong dependence on the grain radius, concerning both trends and absolute values, is evident by comparing with other lines. Note, for example, that at $h\nu \sim 300\,\mathrm{eV}$, the value of Y (for both materials) changes by a factor of 100 as a goes from 1 µm (big grains, orange line) to 1 nm (very small grains, red line). For very small grains, Y rapidly saturates to high values meaning that the photo-electric process is very efficient at all ionizing energies. Comparing lines with the same colour across panels, one notices also a strong dependence on chemical composition.

The dependence of Y on the initial Z for our reference grain size is shown in Fig. 5.4. As in the bottom panel of Fig. 5.1, lines from red to light-blue indicate the transition from the lowest possible charge number to the highest possible charge number. The Coulomb potential of positively charged grains, as expected, rapidly suppresses the photo-electric efficiency as indicated by the sudden decrease of Y when $\log(Z) \geq 2$. For negative charge numbers, on the other hand, the expulsion of an electron is more likely when the incoming photons have energies $h\nu \leq 20\,\mathrm{eV}$, while at higher energies, differences to the neutral case are weak. Again, a strong difference can be seen between grain materials; note, for example, that, at $h\nu < 8\,\mathrm{eV}$ for very negatively charged silicate grains $Y \sim 1$, in opposition to the neutral case.

In analogy to the collisional case, given a radiation field with specific radiation energy density u_ν, we can express the charging current experienced by a grain of some composition due to photo-ejections as follows:

$$J_{\rm pe} = e \int \mathrm{d}\nu \frac{c u_\nu}{h\nu} \sigma_{\rm a}(\nu, a) Y(\nu, a, Z)\,. \tag{5.3}$$

The excess electrons attached to negatively charged grains are assumed to occupy energy levels above the valence band by WD01b. As a result, photo-detachment of

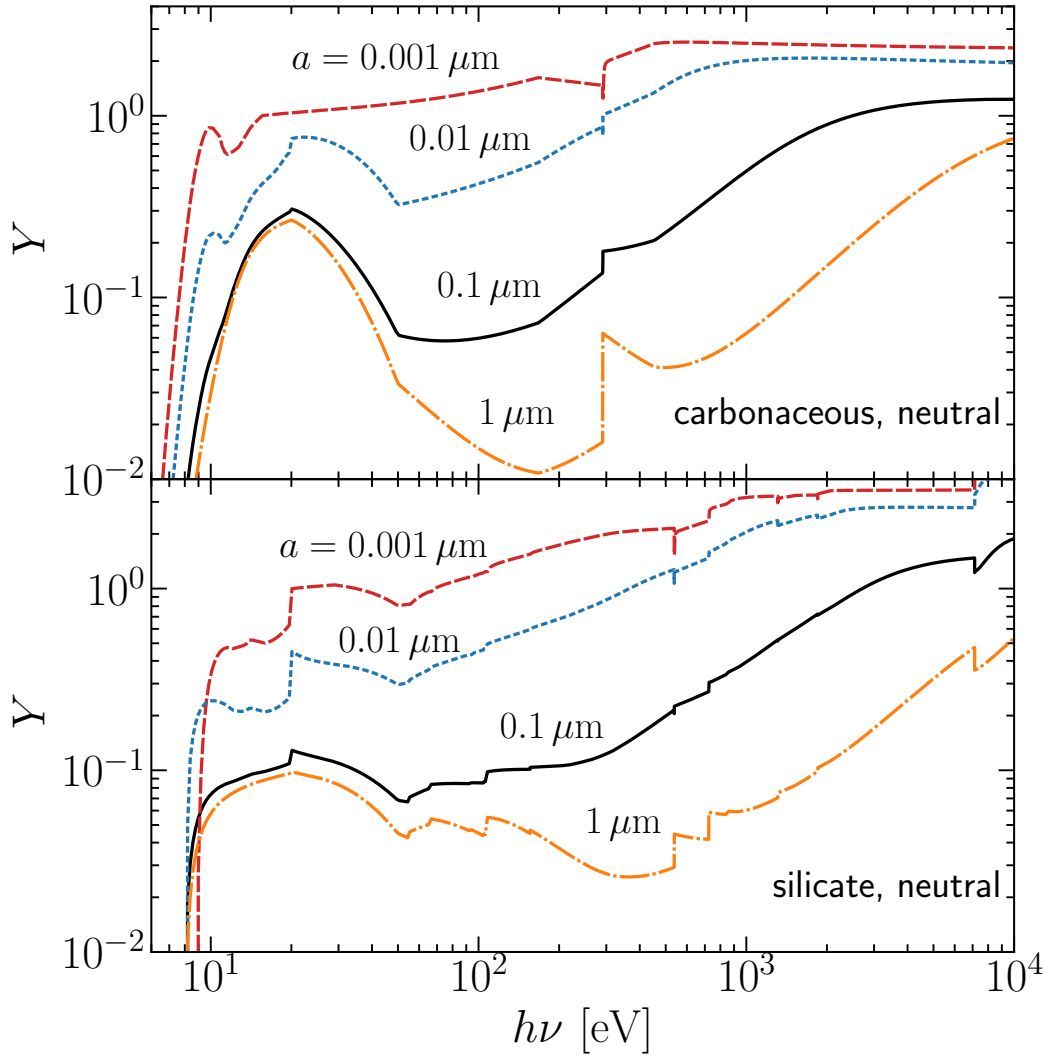

Figure 5.3: Photo-electron yield as a function of photon energy $h\nu$ for carbonaceous (upper panel) and silicate (lower panel) grains of various radii a (line styles and colours) with initial charge $Z = 0$.

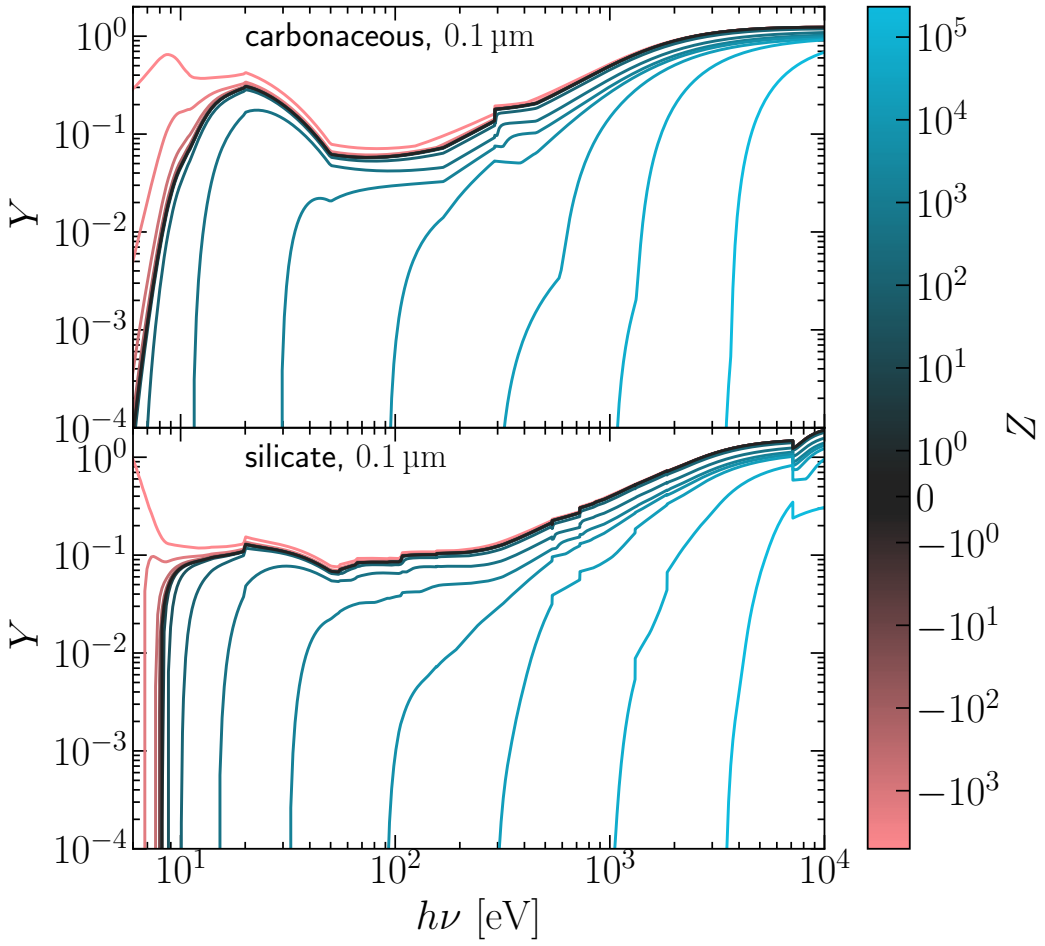

Figure 5.4: Photo-electric yield as a function of photon energy $h\nu$ for carbonaceous (top panel) and silicate grains (bottom panel) of our reference grain radius $a = 0.1\,\mu\text{m}$. Line colours indicate different values of Z as shown by the colour bar (symlog scale).

these electrons has to be accounted for in the form of a separate current $J_{\rm pd}$, which is computed analogously to $J_{\rm pe}$:

$$J_{\rm pd} = e \int {\rm d}\nu \frac{c u_\nu}{h\nu} \sigma_{\rm pd}(\nu, a, Z)\,, \tag{5.4}$$

with the cross section $\sigma_{\rm pd}$ described in WD01b, § 2.3.3 and $Y_{\rm pd} = 1$.

5.1.3 Time evolution of a grain's charge

Not all charging currents discussed in § 5.1.1 and § 5.1.2 are relevant under all circumstances. When considering ionizing radiation, $J_{\rm pd}$ is subdominant to $J_{\rm pe}$. Where a strong radiation field is present, $J_{\rm pe}$ will also dominate over collisional charging with ions ($J_{\rm ion}$). Finally, in photo-ionized regions, where usually $T \sim 10^4\,{\rm K}$, $J_{\rm sec,gas}$ provides a second order contribution. For these reasons, in the preliminary discussion presented here, $J_{\rm pd}$, $J_{\rm ion}$ and $J_{\rm sec,gas}$ will be neglected.

In analogy to the case of ions (e. g. He I, He II, He III), for a given set of conditions, a grain can be in a number of different charge states with varying probability. The associated probability distribution is referred to as grain charge distribution (e. g. WD01b, Fig. 9). The number of available and typically occupied charge states, especially for large grains, however, is many times higher than in the case of ions. For this reason, we will use a simplified treatment here and consider the temporal evolution of only a single charge[9] for given grain properties, described by

$$e\frac{{\rm d}Z}{{\rm d}t} = J_{\rm pe} + J_{\rm e}\,. \tag{5.5}$$

In a steady state[10], the above equation becomes a root finding problem in Z:

$$J_{\rm pe}(Z) + J_{\rm e}(Z) = 0\,. \tag{5.6}$$

5.2 Implementation in CRASH

In this section we describe the numerical implementation of grain charging in the latest release of CRASH (§ 2.5, Graziani et al. 2018), extended in GCG19 (§ 4.1) to account for dust absorption in the hydrogen ionizing band $h\nu \in [13.6\,{\rm eV}, 10\,{\rm keV}]$.

[9] Note that this charge is not quantized. It can be thought of as an approximation to the average charge of a population of grains, but it will generally differ to some degree from the average of their real charge distribution.

[10] The steady state solution corresponds to the "equilibrium charge" of WDB06, § 7, which they find to be close to the average of the real charge distribution for large grains and even for small grains if charge numbers are high. The equilibrium charge is also what is computed in the approaches of MOCASSIN and CLOUDY (for large grains); see the introduction to this chapter.

The code version adopted here features a significant number of improvements in both algorithmic and engineering aspects, resulting, most significantly, in greatly improved behaviour when simulating media with high dust density, as documented in App. B.

To account for grain charging, we first expanded the list of initial conditions to include 3D maps of the charge at simulation start of each dust species k, $Z_k(t_0)$. Furthermore, the DUST_SPECIES TYPE (§ 4.1) has been extended to load tables of the electron charging rate coefficient as a function of plasma temperature and grain charge $\alpha_k(T, Z)$, as well as the photo-electric yield as a function of photon energy and grain charge $Y_k(h\nu, Z)$. The tables can be provided by any dust model, keeping the implementation general, while the data-set of built-in models has been expanded by including tables of the relevant quantities for the Silicate-Graphite-PAH model, computed as discussed in § 5.1. The DUST_IN_CELL TYPE has been consistently extended to store the charge of each species in the cell.

A fully self consistent treatment of dust charging[11] in our time dependent scheme would require solving a system consisting of Eqs. (2.12), (2.16), a set of equations (one per dust species) in the form of Eq. (5.5), and correspondingly updated closure relations (2.13). Since grain charging timescales ($\sim e/(J_{\mathrm{pe}} - J_{\mathrm{e}})$, Draine & Lazarian 1998) can be many orders of magnitude shorter than hydrogen and helium ionization/recombination timescales (cf. Fig. 5.1), time integration of such a system is extremely challenging. The timesteps adopted in CRASH are adaptive, since a cell is updated every time it is crossed by a photon packet, but they are on the order of the gas recombination time scale and thus generally much longer than the dust charging timescale. Reaching small enough timesteps would require prohibitive numbers of photon packets or a complete restructuring of the CRASH algorithm to enable the use of implicit solvers, which are known to be difficult to combine with MCRT schemes (Noebauer & Sim, 2019). We therefore take a different approach and assume grain charges to always be in steady state at the timescales CRASH resolves, i.e. we evolve the grain charge of each species in each cell from steady state to steady state as the environment (radiation field, temperature, ionization state) changes.

More precisely, every time a cell is crossed by a photon packet, we compute the number of photons of each frequency absorbed by each dust species $\Delta N_{k,\nu}$ using Eq. (4.3). Since it is heavily affected by MC sampling noise, we accumulate this quantity over a number N_{d} of packet crossings to obtain a robust estimate of its time average $\Delta N^{\mathrm{acc}}_{k,\nu}/\Delta t_{\mathrm{d}}$, where Δt_{d} is the time since the last charge computation. We then use a root finder to solve Eq. (5.6) for the new charge value Z_k, approximating the photo-electric charging current:

$$J_{\mathrm{pe},k} = \frac{e}{\Delta t_{\mathrm{d}}} \sum_{\nu} \Delta N^{\mathrm{acc}}_{k,\nu} Y_k(h\nu, Z_k)\,, \tag{5.7}$$

[11] Neglecting the grain charge distribution; cf. § 5.1.3.

and the electron charging current:

$$J_{\mathrm{e},k} = -en_{\mathrm{e}}\alpha_k(T, Z_k)\,, \tag{5.8}$$

where Y and α are computed by interpolation on the pre-loaded tables and n_{e} and T take the current cell values. We verified that a value of $N_{\mathrm{d}} \sim 100$ is typically required to overcome MC noise[12]. Finally, note that we account for the dust contribution to n_{e}, we do not yet, however, account for the dust contribution to cooling and heating of the plasma (cf. § 2.2.3).

A detailed validation of our approach in complex time dependent configurations is still outstanding. It might be problematic in the case of very small grains, for example, as their charging timescales could reach values comparable to those of the gas. The preliminary results presented below are not affected by this, since they correspond to global equilibria of their respective configurations.

In GCG19 (Ch. 4), our simulations included only one dust species with properties corresponding to the average of a grain population. When considering only absorption, this does not constitute an approximation (Steinacker et al., 2013), however, since we now account also for charging, we have to resolve a given grain population in composition and size, as these strongly affect the charging process. A typical run might now include eight dust species (see below). This is demanding in terms of memory requirements, which scale with the product of the number of computational cells, dust species and frequency bins (to compute $\Delta N^{\mathrm{acc}}_{k,\nu}$). The memory cost is especially high in cases investigating ISM environments, where the dust generally pollutes a large part of the domain, but note that in realistic cosmological simulations the dust-contaminated domain is usually limited to the environments of star-forming galaxies, significantly limiting the number of enriched cells.

The new features documented above will be employed in the following to study a series of ideal H II region configurations. We consider eight dust species, spanning the radii $a \in \{0.001, 0.01, 0.1, 1.0\}$ µm and the compositions graphite and silicate in the Silicate-Graphite-PAH framework[13]

5.3 Results

In this section we investigate the grain charges attained in H II regions created by sources with multi-frequency spectra emitting in the hydrogen ionizing band. We will here consider a realistic dust population consisting of the eight species mentioned

[12] The total number of packets crossing a typical cell during a simulation $\gg N_{\mathrm{d}}$.

[13] We use carbonaceous charging properties (α and Y, cf. § 5.1) for the graphite grains, since no pure graphite prescription is available. This is not fully self consistent as small carbonaceous grains are tuned to the properties of PAHs, which we do not consider in this chapter, but given the associated uncertainties it is certainly acceptable.

above. Since for the time being we do not account for PAHs, we use the MRN (Mathis et al., 1977) graphite/silicate size distribution with normalizations as given by WD01a to determine their relative abundances.

5.3.1 Black body source

The basic simulation setup we use here is identical to that of the reference run in GCG19, § 5.1 (cf. § 4.2.1). We therefore only summarize the most important properties: a source with a black body spectrum ($T_{\mathrm{bb}} = 10^4\,\mathrm{K}$) is placed in the corner of an $(85\,\mathrm{pc})^3$ box with a constant gas density $n_{\mathrm{g}} = 1\,\mathrm{cm}^{-3}$ and cosmological abundances of H and He mapped onto a Cartesian grid with 256^3 cells. The medium is polluted with dust at a GDR of 124. We run the simulation for 10 Myr, ensuring that equilibrium in temperature and ionization is reached, while using 2×10^9 photon packets to reach good MC convergence. Initially, gas and dust are neutral and the gas temperature $T = 10^2\,\mathrm{K}$.

Fig. 5.5 shows the radial profiles of the charges of grains of different sizes (lines) and materials (panels) in the final equilibrium configuration. Close to the source, all grains are positively charged, but they attain negative charges as the photon flux becomes weaker when moving away from the source. At the hydrogen ionization front ($\sim 60\,\mathrm{pc}$), the number density of free electrons is drastically reduced, resulting in grain charges becoming more positive again. In contrast to the monofrequency cases presented in App. E, however, the residual flux of high-energy photons beyond the ionization front results in weak ionization of the gas and thus a non-zero number density of free electrons, which keeps the charges negative instead of neutral.

Note that even the highly idealized H II region investigated here features a complex charge structure, predicting spatially strongly varying conditions for grain evolution.

5.3.2 A young stellar population

Here we approximate the conditions surrounding a young stellar population born in a dusty high redshift galaxy.

We use `pyBPASS`[14] to obtain the BPASS v2.2.1 (Stanway & Eldridge, 2018) spectrum of a single stellar population including binaries with an initial metallicity of $0.1 Z_\odot$, a Chabrier initial mass function (Chabrier, 2003) with an upper limit of $300\,\mathrm{M}_\odot$, an age of 5 Myr, and a mass of $10^6\,\mathrm{M}_\odot$. The resulting spectrum in the range 13.6 eV to 500 eV is shown in Fig. 5.6 (solid black line) along with the binned version (dashed red line, 70 bins) we use in CRASH. Note that it extends into the X-ray regime, which we can consistently account for. We place this source in the corner of a $(60\,\mathrm{pc})^3$ box containing a homogeneous, cosmological H-He mixture at a density of $10\,\mathrm{cm}^{-3}$ and dust at a GDR of 50. These parameters are motivated by

[14] `https://gitlab.mpcdf.mpg.de/mglatzle/pybpass`

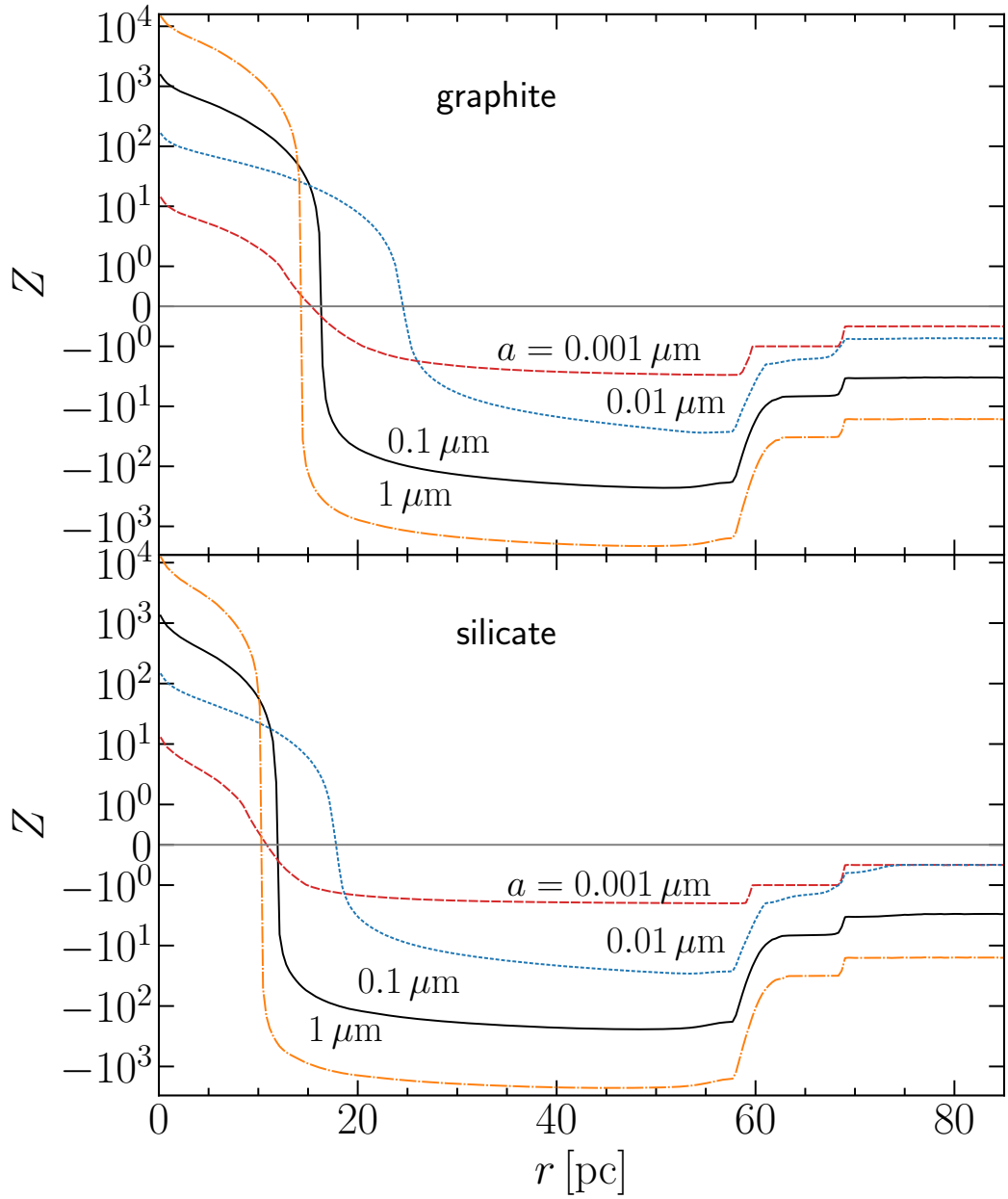

Figure 5.5: Grain charge at equilibrium as a function of distance from an ionizing black body source for a simulation including eight species of grains with different sizes (line styles) and chemical compositions (panels). The horizontal line is drawn to guide the eye. See text for details.

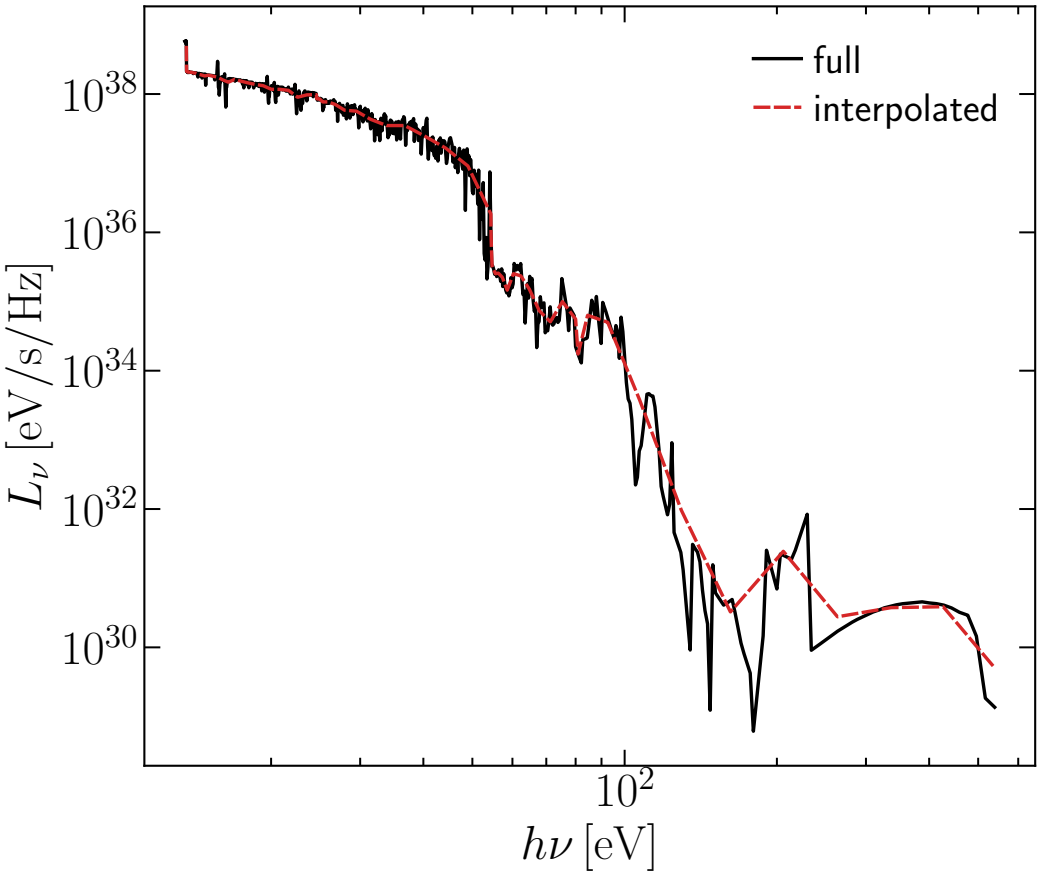

Figure 5.6: The spectrum of a young, low metallicity stellar population as predicted by BPASS (solid black line). Also shown is the binned version used in CRASH (dashed red line). See text for details.

the values found for young stellar populations and their surroundings in the epoch of reionization ($z \gtrsim 6$) in Graziani et al. (2020) (cf. § 3.6).

Fig. 5.7 shows the resulting radial profiles of the charges of grains of different sizes (lines) and materials (panels) at equilibrium. The qualitative behaviour is similar to that seen in Fig. 5.5, however, the harder spectrum results in significantly higher charge values close to the source. It also results in more negative charges outside the ionization front ($\sim 30\,\mathrm{pc}$), where it provides stronger partial ionization of the gas. Finally, in the $\sim 2\,\mathrm{pc}$ region closest to the source, the Coulomb explosion limit is reached for the smallest (0.001 µm) grains of both compositions. Our numerical scheme does not account for grain destruction yet, so it sets the grain charge to zero here.

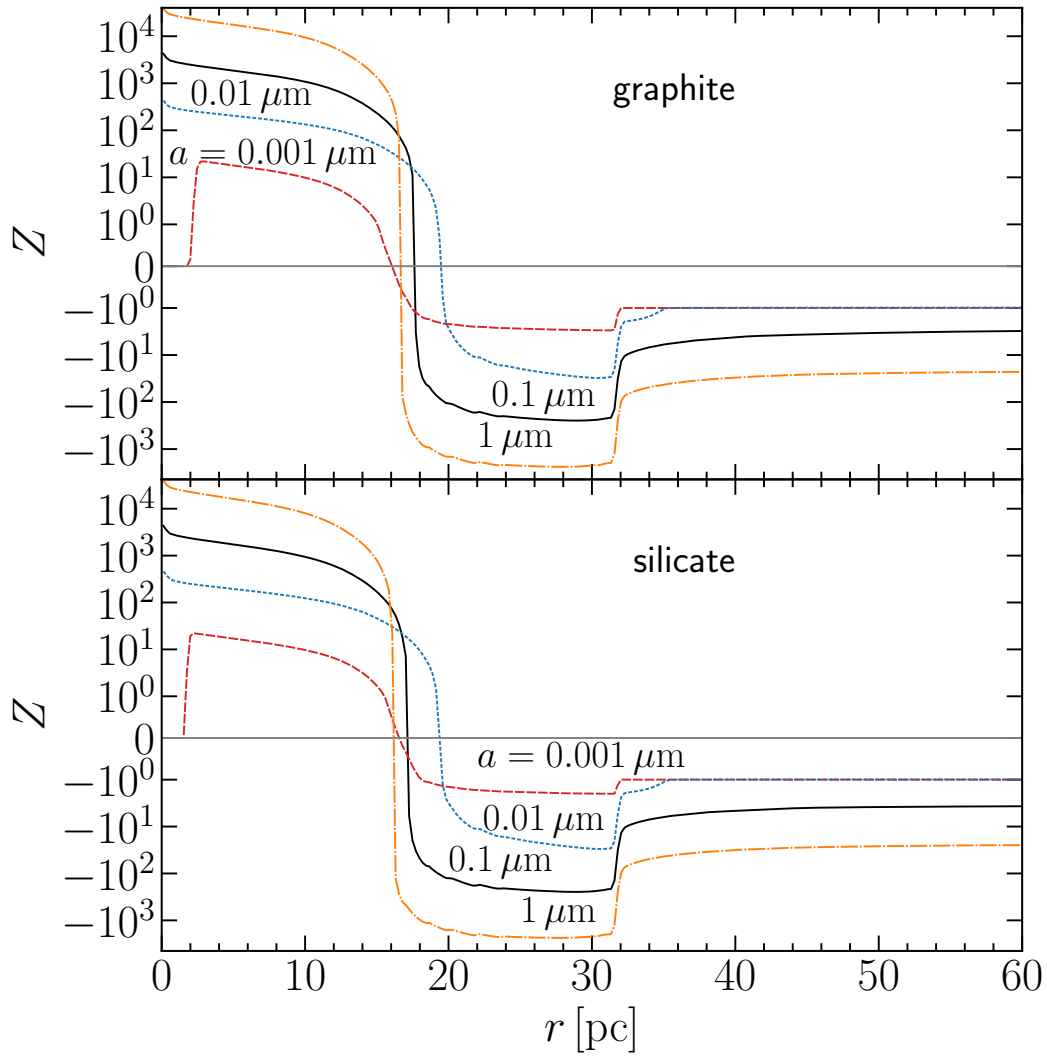

Figure 5.7: Like Fig. 5.5, but for a source with the spectrum of a young stellar population as provided by BPASS. See text for details.

The results presented here clearly show the potential of our implementation to investigate grain charging and some of its consequences as discussed in the introduction to this chapter. The case of high energy radiation causing partial gas ionization and thus making available electrons to negatively charge grains is particularly interesting, as this could be conducive to the growth of grains. Naturally, a closer investigation is required, taking into account diffuse matter and source distributions representative of the ISM, as well as further radiation bands, which could increase the photo-electric charging rate and drive grain charges towards more positive values.

Chapter 6

Outlook: the escape of ionizing radiation from galaxies

In this section we provide a short description of an ongoing project, focussed on determining the multi-frequency escape fraction of ionizing radiation from early galaxies. We briefly introduce the problem, describe the work performed so far, present early results and discuss possible future steps.

In the current standard paradigm, reionization (cf. § 1.2) is assumed to be driven by the ionizing radiation produced by the stars of early galaxies (e.g. Meiksin, 2009; Wiklind et al., 2013). One of the most important parameters in characterising this scenario is the escape fraction of ionizing photons, $f_{\rm esc}$, i.e. the fraction of the photons produced by stars that actually arrives at the intergalactic scale and contributes to (re)ionizing the IGM. $f_{\rm esc}$ remains, despite considerable effort, highly uncertain both from an observational as well as from a theoretical/numerical point of view. For reasons of brevity we will not review the extensive literature on this topic. Bian & Fan (2020), Gazagnes et al. (2020) and Smith et al. (2020) provide good starting points for the recent observational literature, while Paardekooper et al. (2015), Ma et al. (2016), Xu et al. (2016) and Rosdahl et al. (2018) do so for the numerical literature.

Fig. 6.1 sketches the challenges associated with a numerical determination of $f_{\rm esc}$. The radiation emitted by a star has to cross its H II region, the (remnants of the) molecular cloud it was born in and the ISM and CGM of its host galaxy before arriving at intergalactic scales. All of these environments, naturally, have strongly differing physical properties. Reionization is thus a multi-scale radiative transfer problem and $f_{\rm esc}$ connects the different scales. The involved dynamical range is too large to be captured in a single simulation and instead requires approaches focussing on different scales. Although difficult to depict in a sketch like Fig. 6.1, a 3D treatment is essential as the escape fraction will strongly depend on the position of a star in a galaxy and also on the direction of propagation of the radiation. Moreover, given the shape of the H/He absorption cross sections (cf. Fig. 2.1), a strong frequency dependence is expected.

The recent discovery of comparatively large amounts of dust in galaxies at high

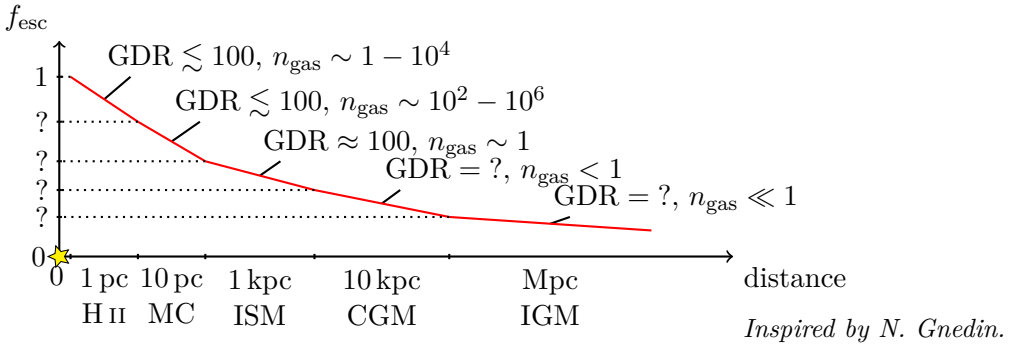

Figure 6.1: Escape fraction of ionizing radiation emitted by a star as a function of distance. The radiation has to traverse the star's H II region, its parent molecular cloud (MC) and the ISM and CGM of its host galaxy before reaching the IGM. At each step an unknown fraction is absorbed. To illustrate how different these environments are, we show GDR and gas density values [cm^{-3}] typical of each in the local Universe.

redshift (cf. § 3.3), even well before reionization ended, and corresponding results from cosmological simulations (cf. § 3.6), further complicate the picture. It is unclear whether dust absorbed significant amounts of ionizing radiation and at what scales its contribution was most important.

In this project, we use CRASH to perform RT post-processing on galaxies from the TNG50 galaxy formation simulation (Nelson et al., 2019; Pillepich et al., 2019) with the goal of determining the multi-frequency escape fraction on ISM to CGM scales. TNG50 is particularly well suited for such a study as it provides a unique combination of a comparatively large cosmological volume of $(35\,\mathrm{h}^{-1}\mathrm{cMpc})^3$ with high resolution ($8.5 \times 10^4\,\mathrm{M}_\odot$ in baryonic mass). A large simulation volume is required to obtain a representative sample of the galaxy population, while high resolution is crucial to provide as much detail as possible on the small scales at which ionizing radiation is produced.

The first phase of the project, which has been completed, consisted of developing a sound framework for the computation of f_{esc}. This phase was highly technical and thus will only briefly be sketched here. From any given TNG50 shapshot, we select DM halos with stellar mass $> 10^6\,\mathrm{M}_\odot$ as smaller halos are too poorly resolved. For each halo, we consider the gas and stars contained in a cube with an edge length of double the halo's virial radius centred on the deepest point of its gravitational potential well. As TNG50 uses the moving-mesh scheme Arepo (Weinberger et al., 2019), we re-grid the matter distribution onto a Cartesian grid, matching the spatial

resolution of the input data. Using `pyBPASS`[1], we obtain spectra including binary contributions from 13.6 eV to 150 eV for the stellar particles, with which we then perform RT in post-processing on each halo. We find that radiative equilibrium is reached on timescales much shorter ($\sim$ Myr) than the time difference between TNG50 snapshots and therefore consider each snapshot independently. After reaching radiative equilibrium, we compute the optical depth τ_ν in each considered frequency bin ν from each stellar particle to the virial radius of the halo using an Monte Carlo ray-tracing scheme. The escape fraction is then given by:

$$f_{\rm esc}^{\nu} = {\rm e}^{-\tau_\nu} \,. \tag{6.1}$$

For each halo, we perform two runs, once considering hydrogen and helium as absorbers, and once additionally accounting for dust. Unfortunately, TNG50 has no intrinsic prescription for dust enrichment, only accounting for atomic metals. In our fiducial model, we therefore assume a constant fraction of metals (0.4 by mass) to reside in dust. This is a frequently used approach motivated by local observations, however, it does not hold true at all times (e.g. De Vis et al. 2019 and Graziani et al. 2020, c.f. § 3.6), resulting in an over-estimate of the dust abundance at low metallicities. If our work reveals a strong dependence of $f_{\rm esc}$ on dust, a more careful approach might be required. We adopt dust properties from the Silicate-Graphite-PAH model for $R_V = 3.1$, as discussed in Ch. 3.

Despite its high resolution, TNG50 does, naturally, not resolve the smallest scales around young stars. Our approach can therefore not account for the escape fraction from the molecular cloud scale, requiring a sub-grid model. In our fiducial approach, we assume $f_{\rm esc}^{\rm sub} = 0.1$. Simulations of star-forming molecular clouds indicate that this is a lower limit for their life-time-averaged escape fraction (Kim et al., 2019). The impact of this parameter on our results will have to be carefully investigated and a more complex sub-grid model accounting for age and metallicity of stellar populations might be required.

Fig. 6.2 shows $f_{\rm esc}^{\nu}$, i.e. the fraction of photons emitted by all stellar particles which are not absorbed inside the virial radius, for exploratory runs of five galaxies (indicated by line colour and labelled by ID) at $z = 6$. The galaxies reside in intermediate mass halos ($\sim 10^{10.5}\,{\rm M}_\odot$). Results without (solid lines) and with dust (dashed lines) are shown. $f_{\rm esc}^{\nu}$ exhibits strong variation from galaxy to galaxy but a qualitatively similar frequency dependence with sharp drops at the ionization frequencies of the different gas species, reaching its highest value towards the He II ionization potential, as the H I and He I cross sections drop. Above this edge, it remains low, growing slowly with photon energy. This is owed to the fact that He II gets ionized less strongly by stellar spectra, even if they include the effects of binaries. Dust absorption exhibits no significant effect on $f_{\rm esc}^{\nu}$. Note that this naturally does

[1] `https://gitlab.mpcdf.mpg.de/mglatzle/pybpass`

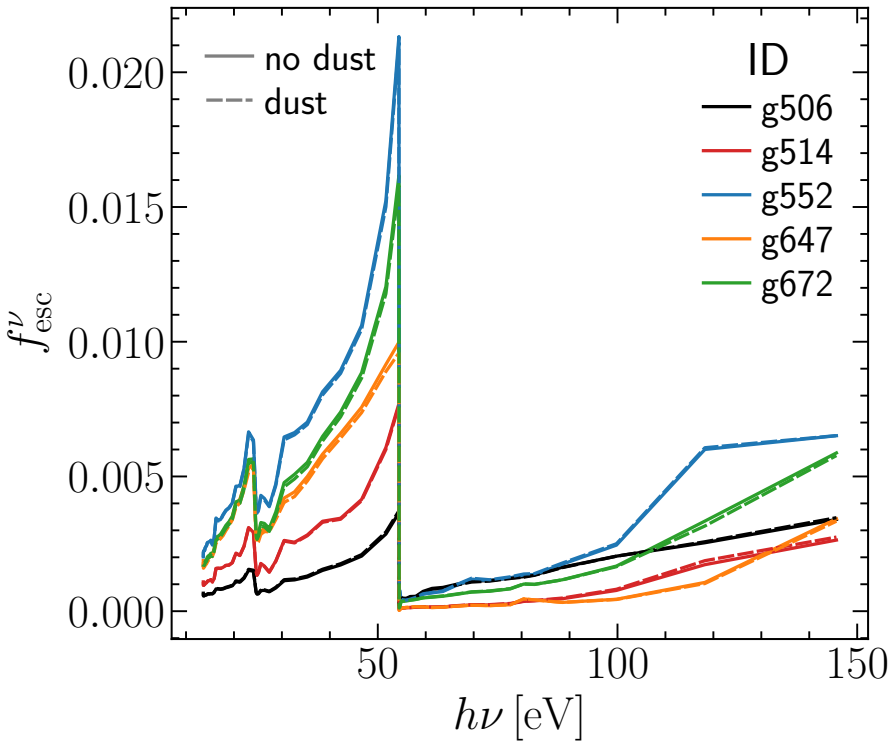

Figure 6.2: Escape fraction as a function of photon energy for five different galaxies of intermediate mass (line colours). Results excluding (solid lines) and including (dashed lines) dust as an absorber are shown. See text for more details.

not preclude a significant contribution of dust on scales which we do not resolve and that furthermore it might be different for galaxies in other mass ranges.

At the time of writing, dusty and dust free runs have been completed for more than one hundred halos covering a wide mass range at redshifts 6, 8 and 10. Analysis of this large dataset will allow to determine interesting directions to investigate. Sets of runs with different configurations will then likely be required to explore the free parameters mentioned above. Finally, studies of representative numbers of galaxies will allow, among other possibilities, to assess consistency with observational constraints on the number of ionizing photons impinging on the IGM at different redshifts (Mason et al., 2019) or to predict the average ionizing spectrum driving reionization.

Chapter 7

Summary and conclusions

Cosmic dust has long been recognized to profoundly impact the chemical and thermal evolution of the ISM of the Milky Way and local galaxies in a complex manner, as grains interact manifoldly with the gas phase and absorb, scatter, and re-emit photons in a wide frequency range. It has also been detected in more distant objects, with recent observations suggesting that star-forming galaxies have been dusty as early as the Epoch of Reionization and thus for a large part of the Universe's history. For these reasons, dust physics is rapidly being integrated into galaxy evolution simulations at all epochs. The presence of dust around galaxies suggested by such simulations, indicates that it is an important ingredient of feedback processes also on CGM and IGM scales.

Consistently accounting for radiative and chemical feedback in numerical simulations is challenging as it requires modelling radiative transfer, the formation, distribution and spectral properties of cosmic lighthouses (e.g. stars and quasars), as well as the dynamics, spatial distribution and microphysics of gas and dust. This thesis investigates different aspects of the above problems, with a focus on implementing the interaction of ionizing radiation with gas and dust in the cosmological RT code CRASH.

The transfer of ionizing radiation emitted by stars and quasars through gas and dust requires a multi-frequency approach. Thus, first, the physics of the ionizing UV and X-rays were investigated and contributions made to Graziani et al. (2018), where CRASH was extended to account for X-rays in addition to the UV (see Ch. 2). It is shown that due to their low cross section, X-rays emitted by quasar-like sources produce heated, weakly ionized regions extending far beyond the ionization fronts created by the UV. The new X-ray extension, combined with the dust treatment discussed below, enables an improved description of the extra-galactic H II regions created by dusty high-redshift quasar hosts and their impact on the process of reionization.

With the aim of obtaining suitable initial conditions for future RT simulations, contributions were made to two studies investigating the distribution and production of dust in the local and high redshift Universe (see Ch. 3). First, a high resolution

reconstruction of the dust distribution in the solar neighbourhood from Gaia[1] data (Leike et al., 2020a) is presented. Complex filamentary structure, the statistics of which have the potential of constraining numerical models of the ISM, is found. The second study (Graziani et al., 2020) is a large scale simulation of the dust budget of high redshift galaxies. The model is in good agreement with the relatively high dust contents recently inferred from observations for diverse galaxies at $z \geq 4$. Grain growth in the ISM is found to be crucial to obtain the required dust masses.

For the remaining work, the Silicate-Graphite-PAH dust model is adopted and the detailed implementation of its prescriptions is discussed in Chs. 3 and 5.

In Ch. 4 an extension of CRASH is presented (GCG19), which accounts for dust absorption in the UV and X-ray bands in a time-dependent scheme and consistently with gas ionization. As a first application, idealized configurations of dusty media around stellar sources are studied. By spanning a wide range of gas densities and gas-to-dust ratios (typical of both galactic and extra-galactic H II regions) a framework is created to interpret results of future, intricate configurations of gas, dust and radiation sources, as predicted by hydrodynamical simulations of galaxies. Dust absorption is found to sharpen ionization fronts and, when grains are abundant, to reduce the size of H II regions, introducing a time delay to their overlap.

As natural follow-up to the work on absorption, grain charging by UV/X-ray radiation is addressed in Ch. 5 (Glatzle et al., 2020, in prep.). Significant numerical and algorithmic challenges had to be overcome to integrate charging into the time dependent scheme of CRASH. A series of tests and comparison with analytic predictions show that the implementation provides reliable results in idealized configurations around young stellar populations, also in the presence of binary stars with spectra extending to the soft X-rays. Strong dependencies of the spatial charge distribution on the spectral shape of the sources, as well as grain composition and size are found. Despite some shortcomings of the implementation, the new scheme should be applicable at ISM and CGM scales. Note that grain charges remain largely unconstrained at all scales and further investigations are required to build a more complete understanding of their environmental dependence, as the charge value of a grain plays a crucial role in its evolution, e.g. through interactions with gas particles.

Finally, in Ch. 6 initial work is presented on a study of the escape fraction of ionizing radiation from galaxies at redshifts > 6, a central parameter in the current standard paradigm of reionization. The escape fraction is to be determined by post-processing high resolution galaxies from the Illustris-TNG50 simulation with CRASH. To accomplish this numerically demanding task, a sophisticated computational pipeline has been implemented, allowing the processing of a large number of objects. A first series of runs has been completed and is awaiting detailed analysis.

[1] `https://sci.esa.int/web/gaia`

Appendix A

Modelling the effect of PAH destruction on the dust cross section

Since no comprehensive model of the processing of PAHs in H II regions is available for the Silicate-Graphite-PAH model, it is not clear how one should modify a given grain size distribution and thus the resulting cross section of a dust mixture to account for it. We explore three different approaches here, presented in detail in the following. Note that we never change the distribution of silicate grains.

As described in § 3.5.2, the Silicate-Graphite-PAH model does not feature a separate PAH population, but PAHs are rather modelled as a part of the carbonaceous grain population. Specifically, LD01 introduce in Eq. (3) a PAH "weight" $\xi_{\mathrm{PAH}}(a)$, where a is the effective grain radius, which they use to make a transition from graphite to PAHs in the absorption cross section of carbon grains (see Eq. (2) of LD01). The total optical depth per distance l due to absorption by carbon dust with cross section $\sigma^{\mathrm{carb}}(a,\nu)$ and grain size distribution $\mathrm{d}n^{\mathrm{carb}}/\,\mathrm{d}a$ is then computed as:

$$\begin{aligned}\frac{\tau^{\mathrm{carb}}(\nu)}{l} &= \int \mathrm{d}a \frac{\mathrm{d}n^{\mathrm{carb}}}{\mathrm{d}a}\sigma^{\mathrm{carb}}(a,\nu) \\ &= \int \mathrm{d}a \frac{\mathrm{d}n^{\mathrm{carb}}}{\mathrm{d}a}(\xi_{\mathrm{PAH}}\sigma^{\mathrm{PAH}}(a,\nu)) + (1-\xi_{\mathrm{PAH}})\sigma^{\mathrm{gra}}(a,\nu))\,,\end{aligned} \tag{A.1}$$

with PAH ($\sigma^{\mathrm{PAH}}(a,\nu)$) and graphite ($\sigma^{\mathrm{gra}}(a,\nu)$) cross sections as defined in WD01a.

In our first approach, which we refer to as "split", we propose to split the carbon grain population into a PAH and a graphite population, i.e. we define grain size distributions

$$\frac{\mathrm{d}n^{\mathrm{PAH}}}{\mathrm{d}a} = \xi_{\mathrm{PAH}}(a)\frac{\mathrm{d}n^{\mathrm{carb}}}{\mathrm{d}a} \tag{A.2}$$

and

$$\frac{\mathrm{d}n^{\mathrm{gra}}}{\mathrm{d}a} = (1-\xi_{\mathrm{PAH}}(a))\frac{\mathrm{d}n^{\mathrm{carb}}}{\mathrm{d}a}\,. \tag{A.3}$$

With these definitions, the total carbon dust optical depth becomes:

$$\begin{aligned}\frac{\tau^{\mathrm{carb}}(\nu)}{l} &= \int \mathrm{d}a \left(\frac{\mathrm{d}n^{\mathrm{PAH}}}{\mathrm{d}a} \sigma^{\mathrm{PAH}}(a,\nu) + \frac{\mathrm{d}n^{\mathrm{gra}}}{\mathrm{d}a} \sigma^{\mathrm{gra}}(a,\nu)) \right) \\ &= \frac{\tau^{\mathrm{PAH}}(\nu)}{l} + \frac{\tau^{\mathrm{gra}}(\nu)}{l} \,.\end{aligned} \tag{A.4}$$

To account for H II region processing, we then set $\mathrm{d}n^{\mathrm{PAH}}/\,\mathrm{d}a$ to zero when computing cross sections.

The motivation for this approach lies in excluding the contribution to the cross section attributed to PAHs in the Silicate-Graphite-PAH model. This does, however, result in a size distribution (see dashed red line in Fig. A.1) unlikely to represent physical reality, since it features a kink at 50 Å and rises again towards the lower size limit, while the smallest PAHs are expected to be the most susceptible to photo-dissociation (e.g. Bocchio et al., 2012).

Draine & Li (2007) use q_{PAH}, the mass fraction of dust contained in carbonaceous particles with fewer than 1000 C atoms, to quantify the PAH content of a given grain size distribution. Although the PAH destruction efficiency is unlikely to feature a sharp transition specifically at 1000 C atoms (roughly 13 Å in effective radius), we base our second approach, referred to as "cut" (dotted blue line in Fig. A.1), on this definition and sharply cut the carbon grain size distribution here when computing cross sections for H II region processed dust. Otherwise the carbon grains are treated as in the original model.

In the third approach we set $b_{\mathrm{C}} = 0.0\,\mathrm{ppm}$ while keeping all other parameters of the size distributions fixed. This removes the two log-normal distributions that WD01a add to the power-law distribution for the carbonaceous grain population, significantly reducing the number of small carbon grains. We then proceed as in the cut case described above. This approach is motivated by the fact that the MW3.1_00 model from WD01a (see also Draine & Li, 2007, Table 3), which also does not include log-normal distributions, is used to fit dust emission from regions of expected low PAH content (Draine & Li, 2007; Chastenet et al., 2019). It produces the most plausible distribution (dash-dotted orange line) and predicts essentially the same cross section as our split approach (see Fig. 3.8).

To explore the effect of our modified grain size distributions, knowledge of the absorption cross section as a function of photon energy and grain size is required. We can therefore not rely on the published tables of population-averaged cross sections as in § 3.5.2. Instead, we follow the prescriptions given in WD01a, LD01 and Draine (2003a,b,c) to directly compute cross sections. For the purposes of the discussion in Ch. 4, we can restrict our attention to the energy range 13.6 eV to 160 eV, since none of the spectra we used there extends beyond this range[1]. As stated in § 3

[1] But see App. E.

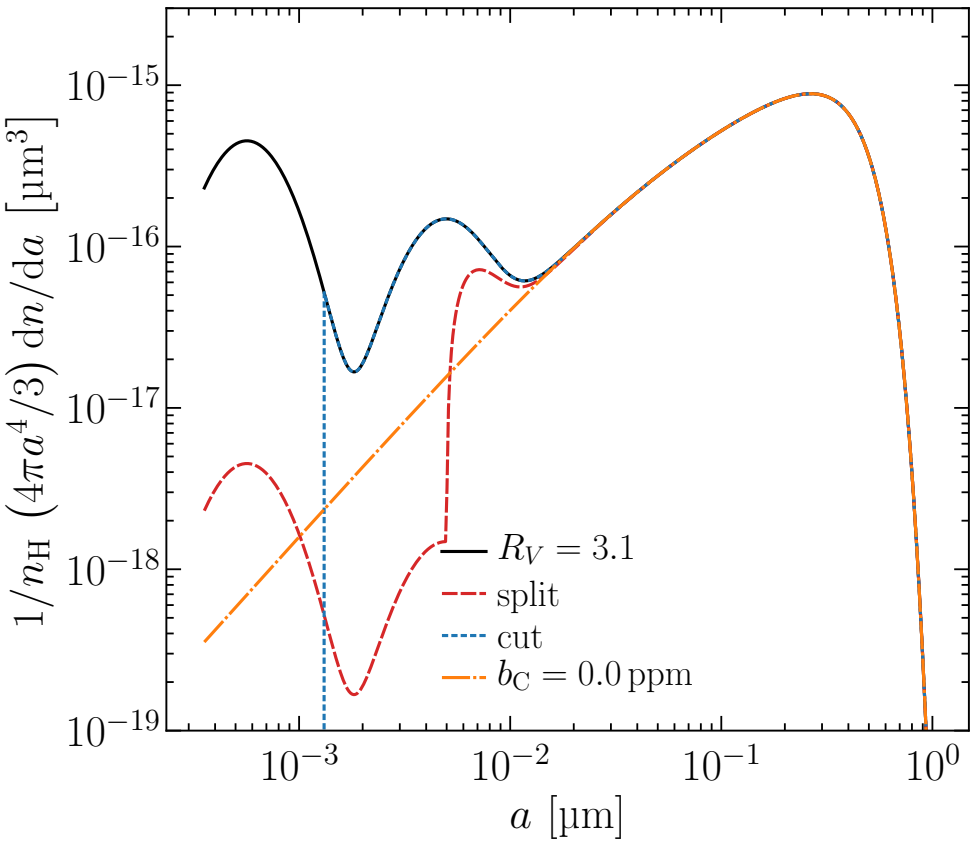

Figure A.1: Fig. B1 of GCG19. Volume distributions for different carbonaceous grain populations. The black solid line shows the unmodified distribution for $R_V = 3.1$ and $b_{\rm C} = 60\,{\rm ppm}$ as in WD01a, with the other lines showing our approaches to modelling H II region processing of dust as discussed in the text. The split, cut and $b_{\rm C} = 0.0\,{\rm ppm}$ approach result in a dust (including silicate grains) mass density reduction by 6.1 %, 4.7 % and 6.3 % relative to the unmodified distribution, respectively. Cf. Draine & Li (2007).

of Draine (2003c), the Wiscombe Mie theory code was used to compute graphite and silicate cross sections for $x = 2\pi a/\lambda < 2 \times 10^4$, with λ the photon wavelength, while anomalous diffraction theory (van de Hulst, 1957) was used otherwise. For $h\nu = 160\,\mathrm{eV}$ and $a = 10\,\mu\mathrm{m}$ (generous upper limit of the grain size distribution), $x \approx 8100$, so that we use Mie theory[2] in the entire energy range. For silicate grains we used the tabulated values of the WD01a "smoothed astronomical silicate" dielectric function[3]. For graphite, on the other hand, we use the Draine (2003c) dielectric functions[4] for grain sizes of 0.01 µm and 0.1 µm, and we interpolate these linearly in grain size. For the PAH cross section we use Eqs. (5) to (11) from LD01, although only Eqs. (5), (6) and (7) are relevant for our energy range. In this regime the cross sections of neutral and ionized PAHs are identical. Cross sections for energies up to $\sim 31\,\mathrm{eV}$ as a function of grain size are also provided by DustEM[5] (Compiègne et al., 2011) in precomputed tables, which can alternatively be used as input for our framework. We verified that using these data gives results in good agreement with those from the direct Mie computation.

[2] We obtained a version of the Wiscombe code at `http://scatterlib.wikidot.com/mie`.

[3] Provided at `http://www.astro.princeton.edu/~draine/dust/dust.diel.html`.

[4] Provided in tabulated form at the same URL. Note that the E⊥c dielectric function plotted in the bottom panel of Draine (2003b, Fig. 1) was erroneously plotted against $h\nu$ [eV] instead of λ^{-1} [µm^{-1}] as indicated (B. Draine, private communication).

[5] `http://www.ias.u-psud.fr/DUSTEM/`

Appendix B

Comparison with analytic solution: absorption

Strömgren (1939), assuming strongly idealized conditions, developed a well known approximate analytic expression for the hydrogen ionization fraction as a function of distance from a star in ionization equilibrium with the gas surrounding it (e.g. Draine, 2011a), which Petrosian et al. (1972)[1] later extended to include dust in the form of a homogeneously distributed absorber of radiation. Raga & Lora (2015) improved on the Petrosian et al. (1972) solution with a more complex approach. In the regime we investigate below, both agree very well with the exact (up to numerical integration errors) solution, obtained by integration of the differential equation describing the change in ionizing flux with distance from the central star (e.g. Raga & Lora, 2015). As the gas density decreases, the agreement tends to worsen, with Petrosian et al. (1972) predicting sharper ionization fronts (see Raga & Lora, 2015, Fig. 3).

In Fig. B.1 we show $x_{\mathrm{H\,II}}$ as a function of distance normalized to the Strömgren radius from the ionizing source as computed by CRASH (solid lines) as well as the corresponding solutions of the numerical integration (dashed lines) as discussed in Raga & Lora (2015). The simulations shown in this figure are set up as described in § 4.2.1, with various values for n_{gas} (line colours) and GDR (panels). For a meaningful comparison, we have made the following changes:

- He abundance is set to zero;
- the source emits monchromatic photons at 13.6 eV;
- the gas temperature is set to 10^4 K in the entire simulation volume and kept constant during the simulation;
- case B recombination is enabled.

As our scheme is time dependent, we must compare the ionization structure obtained once an equilibrium configuration is reached to a solution obtained explicitly assuming

[1] Note that there is a typo in Eq. (7) of the paper. $1 - y^{3/4}$ should read $1 - y^3/4$.

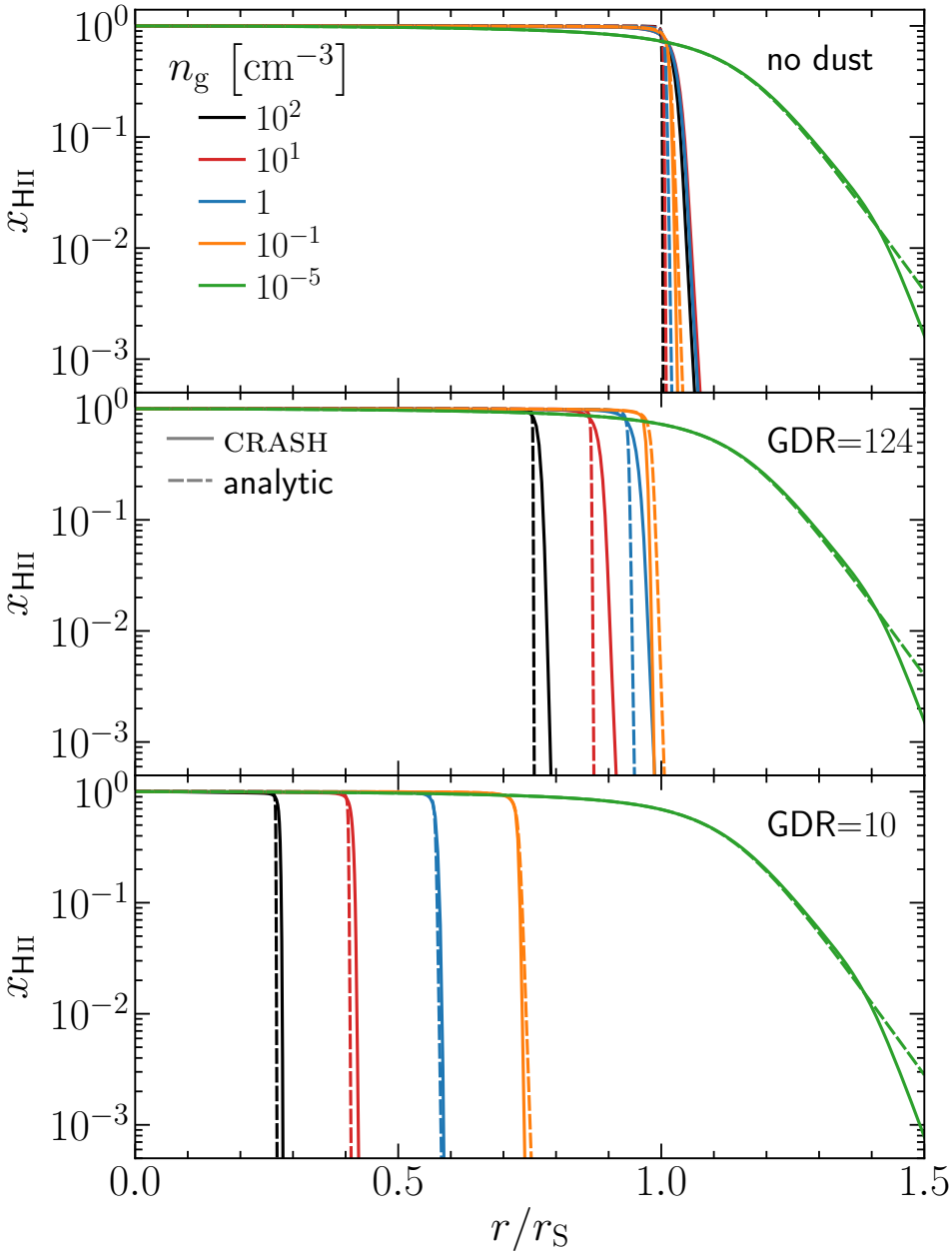

Figure B.1: Hydrogen ionization fraction in equilibrium as a function of distance from the ionizing source normalized to the Strömgren radius for different gas densities (line colours) and different gas to dust mass ratios (panels). The analytic solution (cf. Raga & Lora, 2015) is shown in dashed and the corresponding CRASH results are shown in solid. See text for details.

equilibrium. Despite this stark difference, the agreement of the results is excellent in a wide range of gas number densities and values of GDR.

Note that we discovered an inconsistency in how ionizing photons absorbed by dust were counted in the CRASH version used in GCG19 (Ch. 4). This inconsistency resulted in too many photons being removed from photon packets and thus an overprediction of dust absorption. The effect is strongest in the regime of high gas densities and low GDRs, in which we reported disagreement with the analytic solution in GCG19, App. A and which we, in light of our interest in more tenuous environments and this disagreement, avoided in the other simulations presented in GCG19. The issue has been fixed and we now find much better agreement with the analytic solution in a wide parameter range including the formerly problematic regions, as illustrated by Fig. B.1.

Appendix C

New dust cross sections

Since we encountered problems in reproducing the absorption cross sections of Silicate-Graphite-PAH mixtures using the Mie code by Wiscombe (cf. § 3.5.3, App. A), after the publication of GCG19 we adopted the Mie implementation used in Cloudy (cf. Ch. 5), which provides less functionality but is also less complex. Conveniently, it also applies anomalous diffraction theory in the appropriate limits (cf. App A). We extracted the relevant portions of source code and combined them into an independent C/C++ library. Moreover, we wrote a CPython extension with a NumPy universal function[1] wrapper for the main routine, such that, after compilation, it can conveniently be called from Python with full support of NumPy array arguments. The code has been published[2].

Using this new library in combination with dielectric functions and PAH cross sections as described in App. A, we find far better agreement with the published cross sections at all wavelengths.

[1] `https://numpy.org/doc/stable/reference/ufuncs.html`
[2] `https://gitlab.mpcdf.mpg.de/mglatzle/cosmic_dustbox`

Appendix D

Computation of photo-electric yields

Following WD01b and WDB06, we implemented a Python framework to compute the photo-electric yield for a grain of a given species (carbonaceous or silicate), size and charge at a given photon energy $h\nu$. Here we provide some details on our implementation, an experimental version of which has been made publicly available[1].

In the computation of the photon attenuation length l_a (see WD01b), we use the same dielectric functions as in App. A and App. C to be consistent.

In § 5, WDB06 state first that they use $E_{\mathrm{A},i,s,j}$ when evaluating the electron escape length l_e to compute $y_{0,\mathrm{A}}$ (Eq. (16)). In the next paragraph, however, they state that they use $\Theta_{\mathrm{A};i,s}$ when evaluating $y_{0,\mathrm{A}}$ ($\Theta_{\mathrm{A};i,s}$ also appears as an argument to $y_{0,\mathrm{A}}$ in Eq. (16)). It is not clear to us where $\Theta_{\mathrm{A};i,s}$ could be required to evaluate Eq. (16) other than as a replacement for $E_{\mathrm{A},i,s,j}$ as the argument to l_e. This would, however, effectively introduce a direct dependency of the initial Auger electron energy on the energy of the photon that created the inner shell vacancy, the filling of which initiates the Auger emission process. We do, therefore, not use $\Theta_{\mathrm{A};i,s}$ in Eq. (16) (or anywhere in our calculation, for that matter) and evaluate l_e using $E_{\mathrm{A},i,s,j}$.

When computing secondary electron yields (§ 6), WDB06 adopt bulk values for the initial energy of primary electrons ejected from band structure and inner shells (e.g. $E_{e,\mathrm{band}} = h\nu - W$) in the evaluation of Eq. (18). For consistency with the computation of primary yields, we set $E_{e,k} = \Theta_k$. This has no discernible effect on the results (see next paragraph) and is certainly negligible in light of all other uncertainties in the properties of grain materials.

In the top panel of Fig. 5.3, we reproduce Fig. 4 from WDB06 with very good agreement. The only difference discernible to the eye is the first peak in the $a = 0.001\,\mu\mathrm{m}$ curve at $\sim 10\,\mathrm{eV}$. While our peak reaches ~ 0.9, their peak reaches only ~ 0.7. This is owed to a small bug in the code that was used to plot Fig. 4 of WDB06 (J. Weingartner, private communication).

[1] `https://gitlab.mpcdf.mpg.de/mglatzle/cosmic_dustbox`

Appendix E

Comparison with analytic solution: charging

The analytic solution to the idealized, equilibrium dusty H II region problem used in GCG19, App. A (App. B) provides the hydrogen ionization fraction $x_{\mathrm{H\,II}}$ and the ionizing photon flux as a function of radius from the source. While it is possible to modify it to account for dust charging (cf. Osterbrock & Ferland, 2006, § 7.7), here we take a simpler approach. For typical GDRs (~ 100), if hydrogen is highly ionized, dust charging will not appreciably change the number density of free electrons. This is clearly the case close to the source, while it is not necessarily true towards the ionization front. We therefore compute the grain charge using $x_{\mathrm{H\,II}}$ and the flux as given by the analytic solution, starting from the source and moving outward until we reach a point where the thus predicted charge value would result in a change of the free electron number density of more than one percent. At this point we stop the computation.

Fig. E.1 shows spherical averages of the grain charge Z for CRASH simulations featuring dust populations consisting of grains of a fixed radius (lines) and composition (panels). The simulation setup is identical to that of the simulations shown in Fig. B.1 with $n_{\mathrm{g}} = 1\,\mathrm{cm}^{-3}$ and GDR = 124, except for the fact that all dust mass is comprised of identical grains. Initially, the grain charge is set to zero and it is then evolved until equilibrium is reached. We show the analytic solution as discussed above only for $a = 0.1\,\mu\mathrm{m}$ so as to not overcrowd the plot.

Close to the source, the charge values are positive due to the high ionizing flux. At some distance, a transition to negative charge values takes place as free electrons from hydrogen ionization continue to be highly abundant, while the flux strongly decreases. The transition is sharper for larger grains. The charge then remains negative up to the ionization front where it returns to the initial zero value. The position of the ionization front varies depending on grain size and composition, since we keep the mass of dust constant and small grains offer a higher opacity per mass (cf. Fig. 5.2). The agreement with the analytic solution is excellent up to $\sim r_{\mathrm{S}}$, where we stop computing it as it is no longer valid. This is also true for the other grain sizes (not shown).

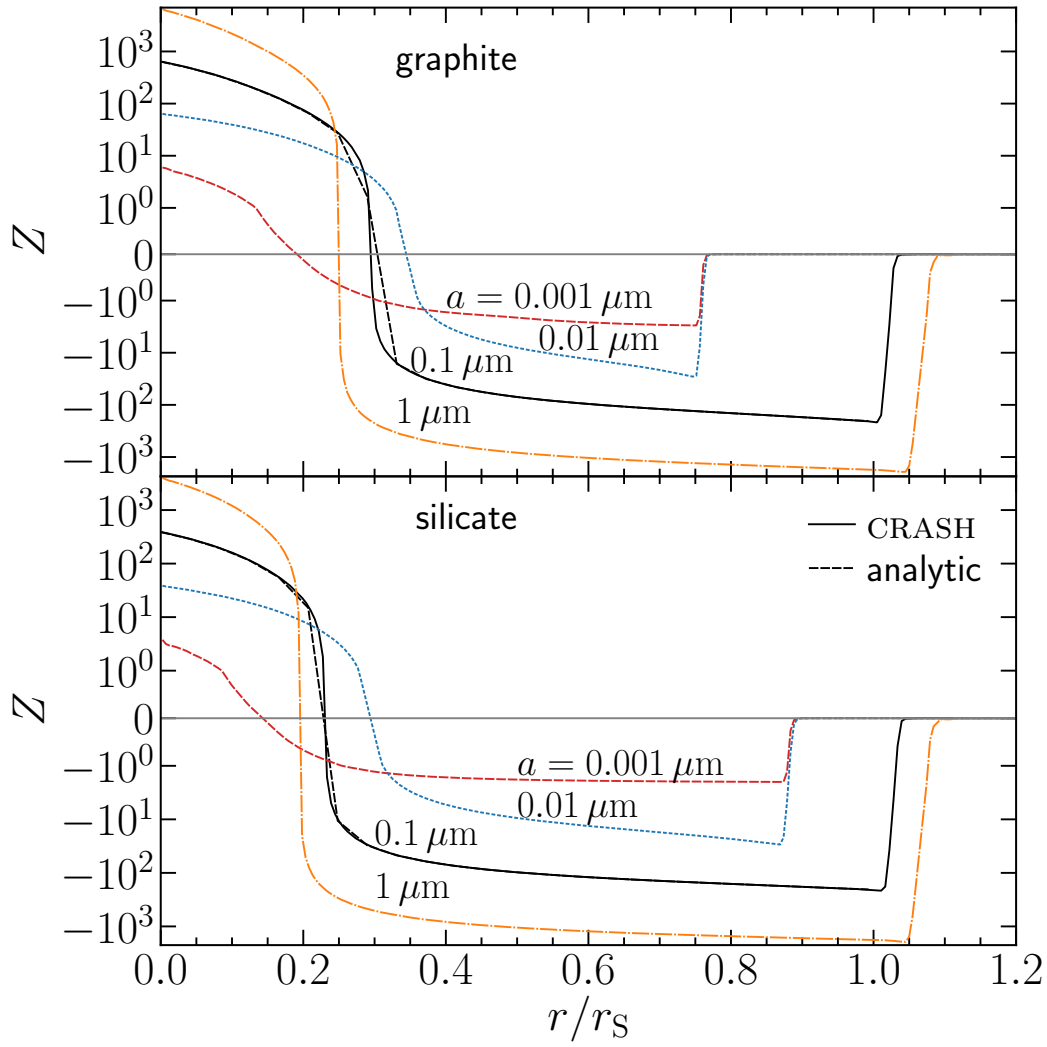

Figure E.1: Grain charge at equilibrium as a function of distance from an ionizing source emitting at 13.6 eV normalized to the Strömgren radius for simulations including grains of different sizes (line styles) and chemical compositions (panels). The gas number density is $1\,\mathrm{cm}^{-3}$ and GDR= 124. For $a = 0.1\,\mu$m, we also show an analytic estimate (dashed black) for comparison to CRASH (solid black). The horizontal line is drawn to guide the eye. See text for details.

Bibliography

Abbott B. P., et al., 2016a, Phys. Rev. Lett., 116, 061102

Abbott B. P., et al., 2016b, ApJ, 826, L13

Abel N. P., Ferland G. J., Shaw G., van Hoof P. A. M., 2005, ApJS, 161, 65

Abel N. P., van Hoof P. A. M., Shaw G., Ferland G. J., Elwert T., 2008, ApJ, 686, 1125

Adrián-Martínez S., et al., 2016, Phys. Rev. D, 93, 122010

Akimkin V. V., Kirsanova M. S., Pavlyuchenkov Y. N., Wiebe D. S., 2015, MNRAS, 449, 440

Akimkin V. V., Kirsanova M. S., Pavlyuchenkov Y. N., Wiebe D. S., 2017, MNRAS, 469, 630

Akimkin V. V., Ivlev A. V., Caselli P., 2020, ApJ, 889, 64

Ali A., Harries T. J., Douglas T. A., 2018, MNRAS, 477, 5422

Amari S., Zinner E., Gallino R., 2014, Geochim. Cosmochim. Acta, 133, 479

Anantharamaiah K. R., 1986, J. Astrophys. Astron., 7, 131

Anders F., et al., 2019, A&A, 628, A94

Angulo R. E., Springel V., White S. D. M., Jenkins A., Baugh C. M., Frenk C. S., 2012, MNRAS, 426, 2046

Aoyama S., Hou K.-C., Shimizu I., Hirashita H., Todoroki K., Choi J.-H., Nagamine K., 2017, MNRAS, 466, 105

Aoyama S., Hou K.-C., Hirashita H., Nagamine K., Shimizu I., 2018, MNRAS, 478, 4905

Arthur S. J., Kurtz S. E., Franco J., Albarrán M. Y., 2004, ApJ, 608, 282

Asplund M., Grevesse N., Sauval A. J., Scott P., 2009, ARA&A, 47, 481

Azimlu M., Marciniak R., Barmby P., 2011, AJ, 142, 139

Bakx T. J. L. C., et al., 2020, MNRAS, 493, 4294

Baldwin J. A., Ferland G. J., Martin P. G., Corbin M. R., Cota S. A., Peterson B. M., Slettebak A., 1991, ApJ, 374, 580

Bañados E., et al., 2018, Nature, 553, 473

Barkana R., Loeb A., 2001, Phys. Rep., 349, 125

Behrens C., Pallottini A., Ferrara A., Gallerani S., Vallini L., 2019, MNRAS, 486, 2197

Bekki K., 2015, ApJ, 799, 166

Bertoldi F., Carilli C. L., Cox P., Fan X., Strauss M. A., Beelen A., Omont A., Zylka R., 2003, A&A, 406, L55

Bian F., Fan X., 2020, MNRAS, 493, L65

Bianchi S., Ferrara A., 2005, MNRAS, 358, 379

Birnstiel T., et al., 2018, ApJL, 869, L45

Bisbas T. G., et al., 2015a, MNRAS, 453, 1324

Bisbas T. G., Haworth T. J., Barlow M. J., Viti S., Harries T. J., Bell T., Yates J. A., 2015b, MNRAS, 454, 2828

Black J. H., 1981, MNRAS, 197, 553

Bocchio M., Micelotta E. R., Gautier A.-L., Jones A. P., 2012, A&A, 545, A124

Bohm D., Aller L. H., 1947, ApJ, 105, 131

Bohren C. F., Huffman D. R., 1983, Absorption and Scattering of Light by Small Particles. Wiley-Blackwell, doi:10.1002/9783527618156

Bohren C. F., Hunt A. J., 1977, Can. J. Phys., 55, 1930

Bolton J. S., Haehnelt M. G., Warren S. J., Hewett P. C., Mortlock D. J., Venemans B. P., McMahon R. G., Simpson C., 2011, MNRAS, 416, L70

Bromm V., Yoshida N., 2011, ARA&A, 49, 373

Bruderer S., van der Marel N., van Dishoeck E. F., van Kempen T. A., 2014, A&A, 562, A26

Calzetti D., Armus L., Bohlin R. C., Kinney A. L., Koornneef J., Storchi-Bergmann T., 2000, ApJ, 533, 682

Camps P., Baes M., 2015, Astron. Comput., 9, 20

Camps P., Baes M., 2018, ApJ, 861, 80

Cardelli J. A., Clayton G. C., Mathis J. S., 1989, ApJ, 345, 245

Carroll S. M., 2014, Spacetime and Geometry - An Introduction to General Relativity. Pearson Education

Casey C. M., Narayanan D., Cooray A., 2014, Phys. Rep., 541, 45

Ceccarelli C., Viti S., Balucani N., Taquet V., 2018, MNRAS, 476, 1371

Cecchi-Pestellini C., Casu S., Mulas G., Zonca A., 2014, ApJ, 785, 41

Cen R., 1992, ApJS, 78, 341

Chabrier G., 2003, PASP, 115, 763

Chastenet J., et al., 2019, ApJ, 876, 62

Cherchneff I., Dwek E., 2009, ApJ, 703, 642

Cherchneff I., Sarangi A., 2017, in Miroshnichenko A., Zharikov S., Korčáková D., Wolf M., eds, Astronomical Society of the Pacific Conference Series Vol. 508, The B[e] Phenomenon: Forty Years of Studies. Astronomical Society of the Pacific, Charles University, Prague, Czechia, p. 57

Churchwell E., et al., 2009, PASP, 121, 213

Ciardi B., Ferrara A., 2005, Space Sci. Rev., 116, 625

Ciardi B., Ferrara A., Marri S., Raimondo G., 2001, MNRAS, 324, 381

Ciardi B., Ferrara A., White S. D. M., 2003, MNRAS, 344, L7

Ciardi B., Bolton J. S., Maselli A., Graziani L., 2012, MNRAS, 423, 558

Clayton G. C., Wolff M. J., Sofia U. J., Gordon K. D., Misselt K. A., 2003, ApJ, 588, 871

Compiègne M., Abergel A., Verstraete L., Reach W. T., Habart E., Smith J. D., Boulanger F., Joblin C., 2007, A&A, 471, 205

Compiègne M., et al., 2011, A&A, 525, A103

Dalgarno A., Yan M., Liu W., 1999, ApJS, 125, 237

De Cia A., Ledoux C., Mattsson L., Petitjean P., Srianand R., Gavignaud I., Jenkins E. B., 2016, A&A, 596, A97

De Looze I., et al., 2014, A&A, 571, A69

De Vis P., et al., 2019, A&A, 623, A5

Dell'Agli F., Di Criscienzo M., García-Hernández D. A., Ventura P., Limongi M., Marini E., Jones O. C., 2019, MNRAS, 482, 4733

Dodelson S., 2003, Modern Cosmology. Academic Press (Elsevier)

Dominik C., Tielens A. G. G. M., 1997, ApJ, 480, 647

Dopita M. A., Sutherland R. S., 2003, Astrophysics of the Diffuse Universe. Astronomy and Astrophysics Library, Springer Berlin Heidelberg, doi:10.1007/978-3-662-05866-4

Draine B. T., 1988, ApJ, 333, 848

Draine B. T., 2003a, ARA&A, 41, 241

Draine B. T., 2003b, ApJ, 598, 1017

Draine B. T., 2003c, ApJ, 598, 1026

Draine B. T., 2009, in Henning T., Grün E., Steinacker J., eds, Astronomical Society of the Pacific Conference Series Vol. 414, Cosmic Dust - Near and Far. Astromomical Society of the Pacific, p. 453

Draine B. T., 2011a, Physics of the Interstellar and Intergalactic Medium. Princeton University Press

Draine B. T., 2011b, ApJ, 732, 100

Draine B. T., 2016, ApJ, 831, 109

Draine B. T., Kreisch C. D., 2018, ApJ, 862, 30

Draine B. T., Lazarian A., 1998, ApJ, 508, 157

Draine B. T., Li A., 2007, ApJ, 657, 810

Draine B. T., Salpeter E. E., 1979a, ApJ, 231, 77

Draine B. T., Salpeter E. E., 1979b, ApJ, 231, 438

Draine B. T., Sutin B., 1987, ApJ, 320, 803

Draine B. T., Tan J. C., 2003, ApJ, 594, 347

Draine B. T., et al., 2007, ApJ, 663, 866

Eide M. B., Graziani L., Ciardi B., Feng Y., Kakiichi K., Matteo T. D., 2018a, MNRAS, 476, 1174

Eide M. B., Gronke M., Dijkstra M., Hayes M., 2018b, ApJ, 856, 156

Enßlin T. A., 2019, Ann. Phys., 531, 1800127

Ercolano B., Barlow M. J., Storey P. J., Liu X.-W., 2003, MNRAS, 340, 1136

Ercolano B., Barlow M. J., Storey P. J., 2005, MNRAS, 362, 1038

Ercolano B., Young P. R., Drake J. J., Raymond J. C., 2008, ApJS, 175, 534

Fan X., Carilli C., Keating B., 2006, ARA&A, 44, 415

Ferland G. J., 2003, ARA&A, 41, 517

Ferland G. J., Williams R. J. R., 2016, in Ralchenko Y., ed., Springer Series on Atomic, Optical, and Plasma Physics, Modern Methods in Collisional-Radiative Modeling of Plasmas. Springer International Publishing, Cham, pp 153–180, doi:10.1007/978-3-319-27514-7_7

Ferland G. J., Henney W. J., O'Dell C. R., Peimbert M., 2016, Rev. Mex. Astron. Astrofisica, 52, 261

Ferland G. J., et al., 2017, Rev. Mex. Astron. Astrofís., 53, 385

Fialkov A., Barkana R., Visbal E., 2014, Nature, 506, 197

Fitzpatrick E. L., 1999, PASP, 111, 63

Friedrich M. M., Mellema G., Iliev I. T., Shapiro P. R., 2012, MNRAS, 421, 2232

Furlanetto S. R., Johnson Stoever S., 2010, MNRAS, 404, 1869

Garay G., Lizano S., 1999, PASP, 111, 1049

Gavilan L., et al., 2016, A&A, 587, A144

Gazagnes S., Chisholm J., Schaerer D., Verhamme A., Izotov Y., 2020, arXiv e-prints, 2005.07215, accepted for publication in A&A

Giannetti A., et al., 2017, A&A, 606, L12

Giard M., Bernard J. P., Lacombe F., Normand P., Rouan D., 1994, A&A, 291, 239

Ginolfi M., Graziani L., Schneider R., Marassi S., Valiante R., Dell'Agli F., Ventura P., Hunt L. K., 2018, MNRAS, 473, 4538

Gioannini L., Matteucci F., Calura F., 2017, MNRAS, 471, 4615

Gjergo E., Granato G. L., Murante G., Ragone-Figueroa C., Tornatore L., Borgani S., 2018, MNRAS, 479, 2588

Glatzle M., Ciardi B., Graziani L., 2019, MNRAS, 482, 321

Glatzle M., Graziani L., Ciardi B., 2020, Radiative Transfer of Ionizing Radiation through Gas and Dust: Grain Charging in Star Forming Regions, in prep.

Gnedin N. Y., 2014, ApJ, 793, 29

Gnedin N. Y., Abel T., 2001, New Astron., 6, 437

Gnedin N. Y., Ostriker J. P., 1997, ApJ, 486, 581

Gordon K. D., Clayton G. C., 1998, ApJ, 500, 816

Gordon K. D., et al., 2017, A&A, 603, A114

Gordon K., et al., 2019, BAAS, 51, 397

Gould R. J., Thakur R. K., 1970, Ann. Phys., 61, 351

Gould R. J., Thakur R. K., 1971, Phys. Fluids, 14, 1701

Graziani L., 2012, PhD thesis, Ludwig Maximilians Universität München

Graziani L., Maselli A., Ciardi B., 2013, MNRAS, 431, 722

Graziani L., Ciardi B., Glatzle M., 2018, MNRAS, 479, 4320

Graziani L., Schneider R., Ginolfi M., Hunt L. K., Maio U., Glatzle M., Ciardi B., 2020, MNRAS, 494, 1071

Greenberg J. M., 1986, in Israel F. P., ed., Light on Dark Matter. Astrophysics and Space Science Library. Springer Netherlands, Dordrecht, pp 177–188, doi:10.1007/978-94-009-4672-9_39

Grün E., Krüger H., Srama R., 2019, Space Sci. Rev., 215, 46

Gunn J. E., Peterson B. A., 1965, ApJ, 142, 1633

Haardt F., Madau P., 2012, ApJ, 746, 125

Han J. L., 2017, ARA&A, 55, 111

Hansen J. E., Travis L. D., 1974, Space Sci. Rev., 16, 527

Hariharan N., Graziani L., Ciardi B., Miniati F., Bungartz H.-J., 2017, MNRAS, 467, 2458

Hashimoto T., et al., 2019, PASJ, 71, 71

Heinisch R. L., Bronold F. X., Fehske H., 2012, Phys. Rev. Lett., 109, 243903

Henning T., Mutschke H., 2010, J. Nanophotonics, 4, 041580

Heß S., Springel V., 2010, MNRAS, 406, 2289

Hirashita H., 2012, MNRAS, 422, 1263

Hirashita H., 2013, in Andersen A. C., Baes M., Gomez H. L., Kemper F., Watson D., eds, The Life Cycle of Dust in the Universe: Observations, Theory, and Laboratory Experiments (LCDU2013). Taipei, Taiwan, p. 27, doi:10.22323/1.207.0027

Hirashita H., Inoue A. K., 2019, MNRAS, 487, 961

Hoang T., 2019, ApJ, 876, 13

Hoang T., Lee H., 2019, arXiv e-prints, 1909.07001, accepted for publication in ApJ

Hoang T., Draine B. T., Lazarian A., 2010, ApJ, 715, 1462

Hockey T., Trimble V., Williams T. R., Bracher K., Jarrell R., Marché J. D., Palmeri J., Green D., eds, 2014, Biographical Encyclopedia of Astronomers, second edn. Springer-Verlag, New York

Hodge J. A., da Cunha E., 2020, arXiv e-prints, 2004.00934

Hunt L. K., Hirashita H., 2009, A&A, 507, 1327

Ibáñez-Mejía J. C., Walch S., Ivlev A. V., Clarke S., Caselli P., Joshi P. R., 2019, MNRAS, 485, 1220

IceCube Collaboration 2018, Science, 361, 147

IceCube Collaboration et al., 2018, Science, 361, eaat1378

Iliev I. T., et al., 2006, MNRAS, 371, 1057

Iliev I. T., et al., 2009, MNRAS, 400, 1283

Imara N., Loeb A., 2016, ApJL, 816, L16

Inoue A. K., Hirashita H., Kamaya H., 2001, ApJ, 555, 613

Ivlev A. V., Padovani M., Galli D., Caselli P., 2015, ApJ, 812, 135

Jackson J. D., 1962, Class. Electrodyn. N. Y. Wiley 1962

Jäger C., Mutschke H., Henning T., Huisken F., 2009, in ASP Conference Series. Heidelberg, Germany, p. 319

Jäger C., Sabri T., Wendler E., Henning T., 2016, ApJ, 831, 66

Jenkins E. B., 2009, ApJ, 700, 1299

Jensen J. J., et al., 2017, MNRAS, 470, 3071

Jessberger E. K., et al., 2001, in Grün E., Gustafson B. Å. S., Dermott S., Fechtig H., eds, Astronomy and Astrophysics Library, Interplanetary Dust. Springer, Berlin, Heidelberg, pp 253–294, doi:10.1007/978-3-642-56428-4_6

Jochims H. W., Ruhl E., Baumgartel H., Tobita S., Leach S., 1994, ApJ, 420, 307

Jones A. P., 2018, arXiv e-prints, 1804.10628

Jones A. P., Fanciullo L., Köhler M., Verstraete L., Guillet V., Bocchio M., Ysard N., 2013, A&A, 558, A62

Jones A. P., Köhler M., Ysard N., Bocchio M., Verstraete L., 2017, A&A, 602, A46

Jonsson P., 2006, MNRAS, 372, 2

Kakiichi K., Graziani L., Ciardi B., Meiksin A., Compostella M., Eide M. B., Zaroubi S., 2017, MNRAS, 468, 3718

Kannan R., Vogelsberger M., Marinacci F., McKinnon R., Pakmor R., Springel V., 2019, MNRAS, 485, 117

Kassis M., Adams J. D., Campbell M. F., Deutsch L. K., Hora J. L., Jackson J. M., Tollestrup E. V., 2006, ApJ, 637, 823

Katz N., Weinberg D. H., Hernquist L., 1996, ApJS, 105, 19

Kemper F., Vriend W. J., Tielens A. G. G. M., 2004, ApJ, 609, 826

Kennicutt Jr. R. C., 1984, ApJ, 287, 116

Kennicutt R. C., Evans N. J., 2012, ARA&A, 50, 531

Kim J.-G., Kim W.-T., Ostriker E. C., 2019, ApJ, 883, 102

Kirchschlager F., Bertrang G. H.-M., 2020, arXiv e-prints, 2004.13742, accepted for publication in A&A

Knollmüller J., Enßlin T. A., 2019, arXiv e-prints, 1901.11033

Kocifaj M., Klačka J., 2012, Opt. Lett., 37, 265

Kocifaj M., Klačka J., Videen G., Kohút I., 2012, J. Quant. Spectrosc. Radiat. Transf., 113, 2561

Köhler M., Stepnik B., Jones A. P., Guillet V., Abergel A., Ristorcelli I., Bernard J.-P., 2012, A&A, 548, A61

Komatsu E., et al., 2011, ApJS, 192, 18

Krieger A., Wolf S., 2020, A&A, 635, A148

Krügel E., 2002, The Physics of Interstellar Dust. Series in Astronomy and Astrophysics, Institute of Physics Publishing

Krügel E., 2007, An Introduction to the Physics of Interstellar Dust. Series in Astronomy and Astrophysics, Taylor & Francis, doi:10.1201/b15897

Kulkarni V. P., Aller M. C., York D. G., Welty D. E., Vladilo G., Som D., 2016, Planet. Space Sci., 133, 7

Laibe G., Price D. J., 2014, MNRAS, 440, 2136

Laporte N., et al., 2017, ApJ, 837, L21

Le Page V., Snow T. P., Bierbaum V. M., 2001, ApJS, 132, 233

Leike R. H., Enßlin T. A., 2019, A&A, 631, A32

Leike R. H., Glatzle M., Enßlin T. A., 2020a, arXiv e-prints, 2004.06732, accepted for publication in A&A

Leike R. H., Celli S., Krone-Martins A., Boehm C., Glatzle M., Fukui Y., Sano H., Rowell G., 2020b, First Optical Reconstruction of Dust in the Region of SNR RX J1713.7-3946 from Astrometric Gaia Data, in prep.

Leinert C., Richter I., Pitz E., Planck B., 1981, A&A, 103, 177

Lewis A. R., et al., 2017, ApJ, 834, 70

Li A., 2020, Nat. Astron.

Li A., Draine B. T., 2001, ApJ, 554, 778

Li A., Greenberg M., 1997, A&A, 323, 566

Li Q., Narayanan D., Davé R., 2019, MNRAS, 490, 1425

Liseau R., et al., 2015, A&A, 578, A131

Lotz W., 1967, ApJS, 14, 207

Lucy L. B., 1999, A&A, 344, 282

Lund K., Wood K., Falceta-Gonçalves D., Vandenbroucke B., Sartorio N., Bonnell I., Johnston K., Keto E., 2019, MNRAS, 485, 3761

Ma Q., Matthews L. S., Land V., Hyde T. W., 2013, ApJ, 763, 77

Ma X., Hopkins P. F., Kasen D., Quataert E., Faucher-Giguère C.-A., Kereš D., Murray N., Strom A., 2016, MNRAS, 459, 3614

Mackey J., Walch S., Seifried D., Glover S. C. O., Wünsch R., Aharonian F., 2019, MNRAS, 486, 1094

Madau P., Dickinson M., 2014, ARA&A, 52, 415

Maio U., Petkova M., De Lucia G., Borgani S., 2016, MNRAS, 460, 3733

Malloci G., Joblin C., Mulas G., 2007, Chem. Phys., 332, 353

Mancini M., Schneider R., Graziani L., Valiante R., Dayal P., Maio U., Ciardi B., Hunt L. K., 2015, MNRAS: Letters, 451, L70

Mancini M., Schneider R., Graziani L., Valiante R., Dayal P., Maio U., Ciardi B., 2016, MNRAS, 462, 3130

Marassi S., Schneider R., Limongi M., Chieffi A., Graziani L., Bianchi S., 2019, MNRAS, 484, 2587

Martins F., Schaerer D., Hillier D. J., 2005, A&A, 436, 1049

Maselli A., Ferrara A., Ciardi B., 2003, MNRAS, 345, 379

Maselli A., Ciardi B., Kanekar A., 2009, MNRAS, 393, 171

Mason C. A., Naidu R. P., Tacchella S., Leja J., 2019, MNRAS, 489, 2669

Massey P., Hunter D. A., 1998, ApJ, 493, 180

Mathis J. S., Rumpl W., Nordsieck K. H., 1977, ApJ, 217, 425

McKinnon R., Torrey P., Vogelsberger M., Hayward C. C., Marinacci F., 2017, MNRAS, 468, 1505

McKinnon R., Vogelsberger M., Torrey P., Marinacci F., Kannan R., 2018, MNRAS, 478, 2851

Meiksin A. A., 2009, Rev. Mod. Phys., 81, 1405

Mellema G., Iliev I. T., Alvarez M. A., Shapiro P. R., 2006, New Astron., 11, 374

Melzer A., 2019, Physics of Dusty Plasmas. Lecture Notes in Physics Vol. 962, Springer, Cham, doi:10.1007/978-3-030-20260-6

Mendis D. A., Rosenberg M., 1994, ARA&A, 32, 419

Messenger S., Keller L. P., Nguyen A. N., 2014, in Proceedings of The Life Cycle of Dust in the Universe: Observations, Theory, and Laboratory Experiments — PoS(LCDU2013). SISSA Medialab, p. 040, doi:10.22323/1.207.0040

Micelotta E. R., Jones A. P., Tielens A. G. G. M., 2010a, A&A, 510, A36

Micelotta E. R., Jones A. P., Tielens A. G. G. M., 2010b, A&A, 510, A37

Mie G., 1908, Ann. Phys., 330, 377

Mo J., Raizen M. G., 2019, Annu. Rev. Fluid Mech., 51, 403

Mo H., Van den Bosch F. C., White S. D., 2010, Galaxy Formation and Evolution. Cambridge University Press New York

Monfredini T., et al., 2019, MNRAS, 488, 451

Mortlock D. J., et al., 2011, Nature, 474, 616

Mulas G., Zonca A., Casu S., Cecchi-Pestellini C., 2013, ApJS, 207, 7

Murga M. S., Wiebe D. S., Sivkova E. E., Akimkin V. V., 2019, MNRAS, 488, 965

Murray N., Quataert E., Thompson T. A., 2005, ApJ, 618, 569

Nelson D., et al., 2018, MNRAS, 475, 624

Nelson D., et al., 2019, MNRAS, 490, 3234

Noebauer U. M., Sim S. A., 2019, Living Rev. Comput. Astrophys., 5, 1

O'Dell C. R., 2001, ARAA, 39, 99

O'Dell C. R., Kollatschny W., Ferland G. J., 2017, ApJ, 837, 151

Osterbrock D. E., Ferland G. J., 2006, Astrophysics of Gaseous Nebulae and Active Galactic Nuclei, second edn. University Science Books

Owen P. J., Barlow M. J., 2015, ApJ, 801, 141

Paardekooper J.-P., Khochfar S., Dalla Vecchia C., 2015, MNRAS, 451, 2544

Peimbert M., Peimbert A., Delgado-Inglada G., 2017, PASP, 129, 082001

Petkova M., Maio U., 2012, MNRAS, 422, 3067

Petrosian V., Silk J., Field G. B., 1972, ApJ, 177, L69

Pierleoni M., Maselli A., Ciardi B., 2009, MNRAS, 393, 872

Pillepich A., et al., 2019, MNRAS, 490, 3196

Planck Collaboration et al., 2018, arXiv e-prints, 1807.06209

Pomraning G. C., 1973, The Equations of Radiation Hydrodynamics, first edn. International Series of Monographs in Natural Philosophy Vol. 54, Pergamon Press

Popping G., Somerville R. S., Galametz M., 2017, MNRAS, 471, 3152

Purcell E. M., Pennypacker C. R., 1973, ApJ, 186, 705

Purcell C. R., et al., 2009, A&A, 504, 139

Rab C., Güdel M., Woitke P., Kamp I., Thi W.-F., Min M., Aresu G., Meijerink R., 2018, A&A, 609, A91

Raga A. C., Lora V., 2015, Rev. Mex. Astron. Astrofís., 51, 189

Raiteri C. M., Villata M., Navarro J. F., 1996, A&A, 315, 105

Raymond J. C., Isenberg P. A., Laming J. M., 2008, ApJ, 682, 408

Reddy N. A., et al., 2015, ApJ, 806, 259

Reddy N. A., Steidel C. C., Pettini M., Bogosavljević M., 2016, ApJ, 828, 107

Relaño M., et al., 2016, A&A, 595, A43

Rémy-Ruyer A., et al., 2014, A&A, 563, A31

Rho J., Andersen M., Tappe A., Gomez H., Smith M., Bernard J. P., Onaka T., Cami J., 2015, Highlights Astron., 16, 583

Richards G. T., et al., 2006, ApJS, 166, 470

Riechers D. A., et al., 2014, ApJ, 786, 31

Rijkhorst E.-J., Plewa T., Dubey A., Mellema G., 2006, A&A, 452, 907

Ritchey A. M., Federman S. R., Lambert D. L., 2018, ApJS, 236, 36

Roche P. F., Aitken D. K., Smith C. H., Ward M. J., 1991, MNRAS, 248, 606

Röllig M., et al., 2007, A&A, 467, 187

Rosdahl J., et al., 2018, MNRAS

Roshi D. A., Anantharamaiah K. R., 2000, ApJ, 535, 231

Salgado F., Berné O., Adams J. D., Herter T. L., Keller L. D., Tielens A. G. G. M., 2016, ApJ, 830, 118

Salim S., Narayanan D., 2020, arXiv e-prints, 2001.03181, to be published in ARA&A

Sandstrom K. M., et al., 2013, ApJ, 777, 5

Sartorio N. S., Vandenbroucke B., Falceta-Goncalves D., Wood K., Keto E., 2019, MNRAS, 486, 5171

Schalén C., 1929, Astron. Nachrichten, 236, 249

Schlafly E. F., et al., 2016, ApJ, 821, 78

Schoenberg E., Jung B., 1934, Astron. Nachrichten, 253, 261

Semelin B., Eames E., Bolgar F., Caillat M., 2017, MNRAS, 472, 4508

Shapiro S. L., Lightman A. P., Eardley D. M., 1976, ApJ, 204, 187

Shull J. M., van Steenberg M. E., 1985, ApJ, 298, 268

Siebenmorgen R., Krügel E., 2010, A&A, 511, A6

Siebenmorgen R., Voshchinnikov N. V., Bagnulo S., 2014, A&A, 561, A82

Smith R. K., Dwek E., 1998, ApJ, 503, 831

Smith J. D. T., et al., 2007, ApJ, 656, 770

Smith B. M., et al., 2020, arXiv e-prints, 2004.04360, accepted for publication in ApJ

Spitzer L., 1978, Physical Processes in the Interstellar Medium. Physics Textbook, Wiley, doi:10.1002/9783527617722

Springel V., 2005, MNRAS, 364, 1105

Springel V., Hernquist L., 2003, MNRAS, 339, 289

Springel V., et al., 2005, Nature, 435, 629

Srama R., et al., 2011, CEAS Space J., 2, 3

Stalevski M., Fritz J., Baes M., Nakos T., Popovic L. C., 2012, MNRAS, 420, 2756

Stanway E. R., Eldridge J. J., 2018, MNRAS, 479, 75

Steinacker J., Baes M., Gordon K. D., 2013, ARA&A, 51, 63

Stephens I. W., Evans J. M., Xue R., Chu Y.-H., Gruendl R. A., Segura-Cox D. M., 2014, ApJ, 784, 147

Strömgren B., 1939, ApJ, 89, 526

Tamura Y., et al., 2019, ApJ, 874, 27

Tazaki R., Tanaka H., Kataoka A., Okuzumi S., Muto T., 2019, ApJ, 885, 52

Tazaki R., Ichikawa K., Kokubo M., 2020, ApJ, 892, 84

Teyssier R., 2002, A&A, 385, 337

Tielens A. G. G. M., 2005, The Physics and Chemistry of the Interstellar Medium. Cambridge University Press, Cambridge

Trumpler R. J., 1930, PASP, 42, 214

Valdes M., Ferrara A., 2008, MNRAS: Letters, 387, L8

Valdés M., Evoli C., Ferrara A., 2010, MNRAS, 404, 1569

Vandenbroucke B., Wood K., 2018, arXiv e-prints, 1802.09528

Vandenbroucke B., Wood K., Girichidis P., Hill A., Peters T., 2018, MNRAS, 476, 4032

Veilleux S., Cecil G., Bland-Hawthorn J., 2005, ARA&A, 43, 769

Venemans B. P., Walter F., Zschaechner L., Decarli R., Rosa G. D., Findlay J. R., McMahon R. G., Sutherland W. J., 2015, ApJ, 816, 37

Venemans B. P., et al., 2017, ApJ, 851, L8

Verner D. A., Ferland G. J., Korista K. T., Yakovlev D. G., 1996, ApJ, 465, 487

Verstocken S., Van De Putte D., Camps P., Baes M., 2017, Astron. Comput., 20, 16

Visser R., Geers V. C., Dullemond C. P., Augereau J.-C., Pontoppidan K. M., van Dishoeck E. F., 2007, A&A, 466, 229

Voit G. M., 1992, MNRAS, 258, 841

Voshchinnikov N. V., 2012, J. Quant. Spectrosc. Radiat. Transf., 113, 2334

Vuong M. H., Montmerle T., Grosso N., Feigelson E. D., Verstraete L., Ozawa H., 2003, A&A, 408, 581

Wang Y., Ferland G. J., Lykins M. L., Porter R. L., van Hoof P. a. M., Williams R. J. R., 2014, MNRAS, 440, 3100

Watson D., Christensen L., Knudsen K. K., Richard J., Gallazzi A., Michałowski M. J., 2015, Nature, 519, 327

Waxman E., Draine B. T., 2000, ApJ, 537, 796

Weinberger R., Springel V., Pakmor R., 2019, arXiv e-prints, 1909.04667

Weingartner J. C., Draine B. T., 1999, ApJ, 517, 292

Weingartner J. C., Draine B. T., 2001a, ApJ, 548, 296

Weingartner J. C., Draine B. T., 2001b, ApJS, 134, 263

Weingartner J. C., Draine B. T., Barr D. K., 2006, ApJ, 645, 1188

Whelan D. G., Lebouteiller V., Galliano F., Peeters E., Bernard-Salas J., Johnson K. E., Indebetouw R., Brandl B. R., 2013, ApJ, 771, 16

Whitney B. A., 2011, Monte Carlo Radiative Transfer. WORLD SCIENTIFIC, pp 151–176, doi:10.1142/9789814374774_0011

Whitney B. A., et al., 2004, ApJS, 154, 315

Whittet D. C. B., 2003, Dust in the Galactic Environment, second edn. Series in Astronomy and Astrophysics, Institute of Physics Publishing

Whittet D. C. B., 2010, ApJ, 710, 1009

Wiklind T., Mobasher B., Bromm V., eds, 2013, The First Galaxies - Theoretical Predictions and Observational Clues. Astrophysics and Space Science Library Vol. 396, Springer-Verlag Berlin Heidelberg

Willis R. F., Feuerbacher B., Fitton B., 1973, in Greenberg J. M., van de Hulst H. C., eds, IAU Symposium Vol. 52, Interstellar Dust and Related Topics. State University of New York at Albany, Albany, N.Y., U.S.A, p. 303

Willott C. J., Carilli C. L., Wagg J., Wang R., 2015, ApJ, 807, 180

Winston E., Wolk S. J., Bourke T. L., Megeath S. T., Gutermuth R., Spitzbart B., 2011, ApJ, 743, 166

Woitke P., Kamp I., Thi W.-F., 2009, A&A, 501, 383

Wood K., Hill A. S., Joung M. R., Low M.-M. M., Benjamin R. A., Haffner L. M., Reynolds R. J., Madsen G. J., 2010, ApJ, 721, 1397

Xu H., Wise J. H., Norman M. L., Ahn K., O'Shea B. W., 2016, ApJ, 833, 84

Yajima H., Li Y., Zhu Q., Abel T., 2012, MNRAS, 424, 884

Ysard N., Jones A. P., Demyk K., Boutéraon T., Koehler M., 2018, A&A, 617, A124

Zafar T., et al., 2018, MNRAS, 480, 108

Zhang Y., Zhang B., Liu X.-W., 2016, ApJ, 817, 68

Zhen J., et al., 2016, ApJ, 822, 113

Zhukovska S., Henning T., Dobbs C., 2018, ApJ, 857, 94

Zubko V., Dwek E., Arendt R. G., 2004, ApJS, 152, 211

de Zeeuw P. T., Hoogerwerf R., de Bruijne J. H. J., Brown A. G. A., Blaauw A., 1999, AJ, 117, 354

van Hoof P. A. M., Weingartner J. C., Martin P. G., Volk K., Ferland G. J., 2004, MNRAS, 350, 1330

van Hoof P. A. M., Van de Steene G. C., Guzmán F., Dehghanian M., Chatzikos M., Ferland G. J., 2020, CAOSP, 50, 32

van de Hulst H. C., 1957, Light Scattering by Small Particles. John Wiley & Sons